
CHAPTER 6

FINITE ELEMENT MODELLING OF MASONRY SHEAR WALLS

6.1 Introduction

This chapter presents an explicit finite element model for the analysis of the WSRM and the Non-WSRM walls. Non-WSRM walls have been modelled as URM walls consistent with the observation of the experimental behaviour reported in Chapter 5.

The theory of macro modelling for masonry, and yield and failure surfaces for masonry and grout are reviewed. Parameters that define the yield surface of masonry under biaxial loading are discussed. The material parameters required for modelling the softening characteristics of the walls are also described. The basics of the explicit algorithm of finite element analysis (FEA) are briefly discussed. The method of incorporating the masonry material model into ABAQUS/Explicit through the VUMAT user material subroutine is described.

The damaged concrete plasticity material model and rebar option available in ABAQUS have been adopted for the modelling of the vertical reinforced grouted cores. It has been shown that, by minimising the kinetic energy and using an appropriate time scaling and/or damping, the model could provide reasonable and efficient prediction of load flow, crack patterns and load-displacement profiles of the WSRM and Non-WSRM walls.

6.2 Theory of Macro Modelling

Masonry is a highly orthotropic material due to the presence of the mortar joints acting as planes of weakness. Use of hollow masonry units and partial grouting of the masonry assemblages further increases the degree of complexity of the material characteristics. In macro modelling, masonry is considered as a homogenised body using the material properties of masonry assemblages, this being in contrast to the micro modelling where the individual constituents are explicitly modelled as described in Chapter 3. There are several macro models reported in the literature that include Samarasinghe et al. (1981), and Dhanasekar (1985) who developed a failure surface for masonry to predict the behaviour of masonry assemblages under biaxial loading conditions. Seim (1994) used an orthotropic material model to simulate the load-deflection response of masonry shear walls. Lourenco (1996) developed a macro model based on the theory of plasticity consisting of two failure surfaces defined by Hill and Rankine type yield surfaces. He applied this model for the prediction of the behaviour of solid unreinforced masonry shear walls.

Use of macro modelling requires coarser mesh (less number of elements) and hence produces quick numerical solutions. As macro modelling of masonry is advantageous when the global behaviour of the structure is of prime importance, in this research project macro modelling has been adopted in preference to the micro model.

In spite of the advantages of macro modelling, it should be remembered that macro modelling in the context of masonry structures is affected by the limitation it imposes on the minimum size of elements. As masonry elements represent homogenised properties of masonry unit and mortar, each element should encompass at least some portion of masonry units and mortar. Random selection of the size of elements would, therefore, not be appropriate. Furthermore, unless the size of the element is not carefully included into the material constitutive relations (will be

further discussed in this chapter), post peak behaviour of masonry could not be reliably predicted.

6.3 Failure Criteria for Masonry

Masonry behaves differently parallel and perpendicular to the bed joint directions. Moreover, its strength under tension and compression is also different. Uniaxial behaviour of masonry is dictated by the tensile cracking and compressive crushing mechanisms. Under biaxial loading more complex behaviour exists. Lourenco et al. (1997) extended the conventional formulation for isotropic brittle materials to describe the orthotropic behaviour of masonry, and provided a yield surface as shown in Fig. 6.1. They used Hill type yield criterion for biaxial compression zones and a Rankine type yield criterion for biaxial tension-compression zones.

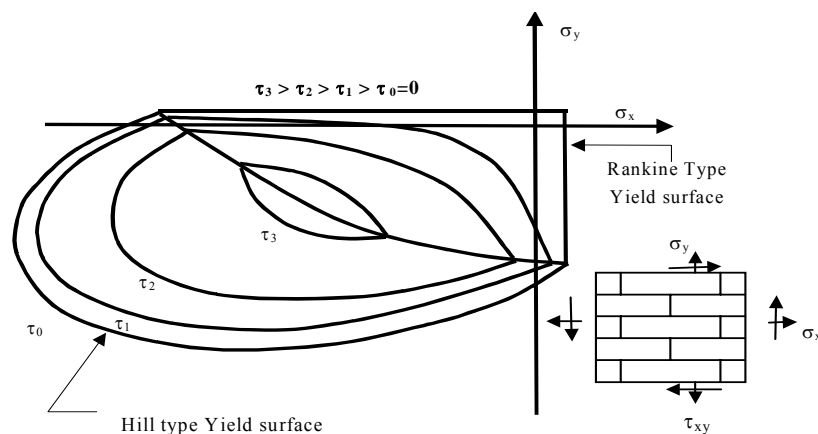


Figure 6.1: Composite yield surface with iso-shear stress lines (Lourenco et al. (1997))

6.3.1 Rankine Tension Failure Criterion

The Rankine type criterion states that yielding of masonry occurs when the maximum principal stress at a point reaches the tensile strength of the masonry. The yield surface representing this criterion is shown in Fig. 6.2. In Fig. 6.2, ' σ_{t1} ' and ' σ_{t2} ' are principal stresses; and ' f_t ' is the tensile yield stress in uniaxial tension.

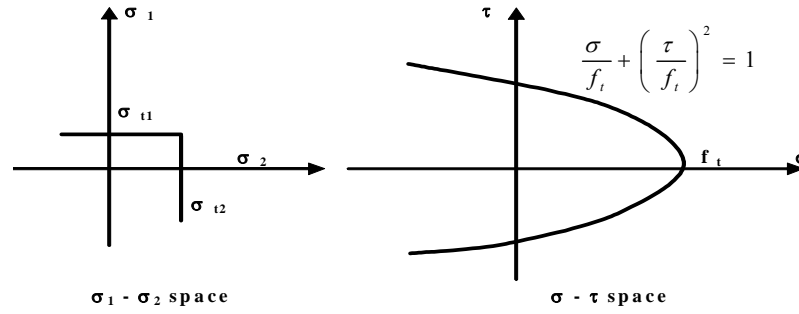


Figure 6.2: Rankine criterion for tension failure

A more adequate formulation of the Rankine yield criterion is given by a single function (f_1), which is governed by the major principal stress and one equivalent stress ' σ_t ' that describes the softening behaviour of the material as shown in Eq. 6.1.

$$f_1 = \frac{\sigma_x + \sigma_y}{2} \pm \sqrt{\frac{(\sigma_x - \sigma_y)^2}{2} + \tau_{xy}^2} - \sigma_t(k_t) \quad (6.1)$$

where ' k_t ' controls the amount of tension softening. For masonry, Lourenco (1996) introduced a single scalar with two different fracture energies to control the orthotropic softening simultaneously along two major axes of orthotropy (perpendicular and parallel to the bed joints). The expression for the Rankine yield criterion with this scalar is shown in Eq. 6.2.

$$f_1 = \frac{(\sigma_x - \sigma_t(k_t)) + (\sigma_x - \sigma_t(k_t))}{2} + \sqrt{\left(\frac{(\sigma_x - \sigma_t(k_t)) - (\sigma_x - \sigma_t(k_t))}{2}\right)^2 + \tau_{xy}^2} \quad (6.2)$$

For different tensile strengths along two axes of masonry, Eq. 6.2 is modified as shown in Eq. 6.3.

$$f_1 = \frac{(\sigma_x - \sigma_{tx}(k_t)) + (\sigma_x - \sigma_{ty}(k_t))}{2} + \sqrt{\left(\frac{(\sigma_x - \sigma_{tx}(k_t)) - (\sigma_x - \sigma_{ty}(k_t))}{2}\right)^2 + \alpha \tau_{xy}^2} \quad (6.3)$$

where ‘ α ’ is a parameter that defines the shear stress contribution to the tension failure of masonry. This parameter is determined from the uniaxial and biaxial tests on masonry, which are discussed later in this chapter.

‘ σ_{tx} ’ and ‘ σ_{ty} ’ are exponential tension softening parameters for two directions (x, y) and they are calculated from Eq. 6.4.

$$\sigma_{tx} = f_{tx} \exp\left(-\frac{hf_{tx}}{G_{fx}}k_t\right); \quad \sigma_{ty} = f_{ty} \exp\left(-\frac{hf_{ty}}{G_{fy}}k_t\right) \quad (6.4)$$

where ‘ h ’ is the characteristic length of elements and ‘ G_{fx} ’ and ‘ G_{fy} ’ are the fracture energies of masonry along ‘x’ and ‘y’ directions respectively. Graphical representation of Eq. 6.4 as adopted for the masonry material considered in this thesis is shown in Fig. 6.3.

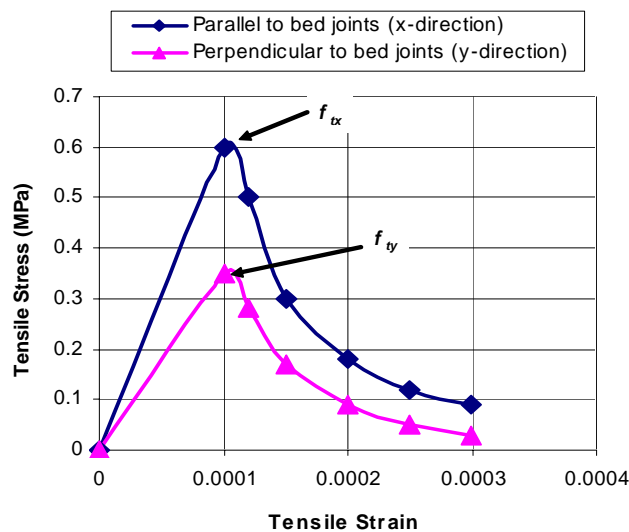


Figure 6.3: Stress – strain curves for masonry under uniaxial tension

For the hollow clay masonry used in the construction of the walls for this research, tensile strengths adopted for the ‘x’ and ‘y’ directions were equal to 0.60MPa and 0.35MPa respectively. The strain at the peak tensile strength in both directions was taken equal to 0.0001.

These stress-strain curves are similar to that adopted by Lourenco (1996). The characteristic length (h) is related to the area of the elements as shown in Eq. 6.5.

$$h = \xi \sqrt{A} \quad (6.5)$$

where ‘ ξ ’ is a constant for the type of element (for quadratic elements, $\xi = 1.0$ and for linear elements $\xi = \sqrt{2}$), and ‘ A ’ is the area of the element. For FEA of brittle concrete structures, a single characteristic length (h) parameter is recommended to be included as a numerical constant where prediction of the softening branch of load-displacement curves are desired (Rots (1988), Feenstra and Borst (1995)). It has been shown that, without the inclusion of ‘ h ’, the results have been affected by mesh pathology.

Typically much work has been carried out in RC structural analysis in comparison to the very limited research in structural masonry. As RC is generally regarded as isotropic, use of a single characteristic length appears appropriate. For distinctly orthotropic materials like masonry, it could be argued that one requires a different characteristic length for two orthotropic directions. However, such fundamental research in computational mechanics is outside the scope of this research.

The minimum size of the characteristic length (h) is defined as in Eq. 6.6.

$$h \leq \frac{G_f E_i}{f_{ti}^2} \quad (6.6)$$

where ‘ E_i ’ is the Young’s modulus and the subscript ‘ i ’ refers to the material axis (‘x’ for the horizontal direction and ‘y’ for the vertical direction). If this condition is violated for any of the material axes, the tensile strength ‘ f_{ti} ’ is reduced according to Eq. 6.7.

$$f_{ti} = \left[\frac{G_f E_i}{h} \right]^{1/2} \quad (6.7)$$

Complete formulation for the Rankine type tension criterion for masonry can be found in Lourenco (1996).

A discrepancy between the values used for the characteristic lengths in the x and y-directions has been found in the analysis of URM walls reported in Lourenco (1996). For example, for the analysis of ETH Zurich shear walls, length and height of 4-noded plane stress elements was 150mm and 133.3mm respectively. The characteristic length of these elements was 200mm as obtained from the product of the square root of the area of the element and $\sqrt{2}$ (Eq. 6.5). Tensile strength of masonry parallel to the x-direction and perpendicular to the y-direction was equal to 0.28MPa and 0.05MPa respectively. Young's modulus of masonry parallel (E_x) and perpendicular (E_y) to the bed joints was equal to 2,460MPa and 5,460MPa respectively. Fracture energy for the 'x' and 'y' directions used in the analysis was 0.02 Nmm/mm². When the values of Young's moduli, fracture energies and tensile strength of masonry given above were used in Eq. 6.7, the characteristic length of elements was determined as 628mm and 43,680mm respectively (compared to the geometric characteristic length of 200mm). This shows that the value of characteristic lengths of elements actually used in the analysis for the x-direction and y-direction were approximately 3 times and 218 times the corresponding values calculated from Eq. 6.7, which is defined as a discrepancy in this thesis.

Based on the above observation, in this research two different characteristic lengths were adopted along the two major orthotropic directions of masonry. Actual characteristic length was multiplied by 60 for the x-direction and by 50 for the y-direction in the calculation of the fracture energies along two directions of masonry, which helped with eliminating the mesh pathology. The sensitivity of the randomly selected multiplication factors '60' and '50' has been examined

and reported in this chapter; typically the selection was justified. This particular issue addresses the obvious inadequacy in the current knowledge; more fundamental research is highly desirable in this area.

6.3.2 Hill Compression Failure Criterion

An expression (f_2) for the simplest compression yield surface (Hill type) that features different compressive strengths along the material axes is shown in Eq. 6.8.

$$f_2 = A\sigma_x^2 + B\sigma_x\sigma_y + C\sigma_y^2 + D\tau_u^2 - 1 = 0 \quad (6.8)$$

where A, B, C, and D are four material parameters as shown in Eq. 6.9.

$$\begin{aligned} A &= 1/(\sigma_{cx}(k_c))^2, & B &= \beta / ((\sigma_{cx}(k_c) (\sigma_{cy}(k_c))), \\ C &= 1/(\sigma_{cy}(k_c))^2, & D &= \gamma / ((\sigma_{cx}(k_c) (\sigma_{cy}(k_c))) \end{aligned} \quad (6.9)$$

where σ_{cx} and σ_{cy} are respectively the compressive yield stresses along the ‘x’ and ‘y’ material axes, and ‘ k_c ’ is a scalar that controls the amount of hardening and softening. ‘ β ’ is the parameter that rotates the yield surface around the shear stress axis, and ‘ γ ’ controls the shear stress contribution to failure. These parameters are typically determined from uniaxial and biaxial tests of masonry. The inelastic compressive law of masonry that features hardening, softening and a residual plateau of ideally plastic behaviour is shown in Fig. 6.4.

Refined compressive fracture energy ‘ G_{fci} ’ shown in the shaded area of Fig. 6.4 corresponds only to the local contribution of ‘ $\bar{\sigma}_{ci} \sim k_c$ ’ diagram, where the subscript ‘ i ’ refers to the material axis. The peak value is considered to be reached simultaneously on both material axes. Isotropic hardening and isotropic softening are determined by different fracture energies.

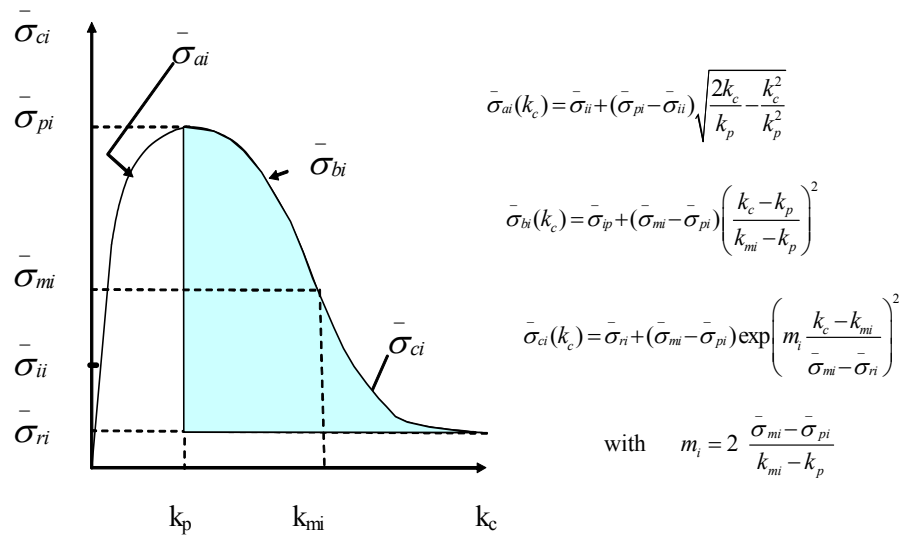


Figure 6.4: Hardening/softening law for compression of masonry (Lourenco (1996))

For practical reasons, this model assumes that all the stress values are determined from the peak value $\bar{\sigma}_{pi} = f_{mi}$ as follows: $\bar{\sigma}_{ii} = 1/3 f_{mi}$, $\bar{\sigma}_{mi} = 1/2 f_{mi}$, $\bar{\sigma}_{ri} = 1/10 f_{mi}$. The equivalent plastic strain ' k_p ' corresponds to the peak compressive strength. In order to obtain mesh independent energy dissipation, the parameter ' k_{mi} ' is given by Lourenco (1996) as:

$$k_{mi} = \frac{75}{67} \frac{G_{fci}}{h f_{mi}} + k_p \quad (6.10)$$

To avoid numerical instability at constitutive level, a condition is required as shown in Eq. 6.11.

$$k_{mi} \geq \frac{f_{mi}}{E_i} + k_p \quad (6.11)$$

If this condition is not satisfied, the strength limit is reduced to a level shown in Eq. 6.12

$$f_{mi} = \left[\frac{75}{67} \frac{G_{fci} E_i}{h} \right]^{1/2} \quad (6.12)$$

The complete formulation for the Hill type criterion for masonry can be found in Lourenco (1996).

The complete material model for masonry contains a composite yield surface of tension and compression failures. Formulation for the composite yield surface can be found in Lourenco (1996).

6.3.3 Parameters Required to Define Masonry Yield Criteria

This composite masonry material model requires seven strength parameters (f_{tx} , f_{ty} , f_{cx} , f_{cy} , α , γ , β), and five inelastic parameters (G_{fx} , G_{fy} , G_{cx} , G_{cy} , k_p) of which the first four are energy parameters. The first group of four strength parameters are the uniaxial tensile and compressive strengths along the material axes, which define the orthotropic behaviour of masonry. Complete characterisation of masonry material requires a set of tests as shown in Fig. 6.5 as a minimum performed under displacement control.

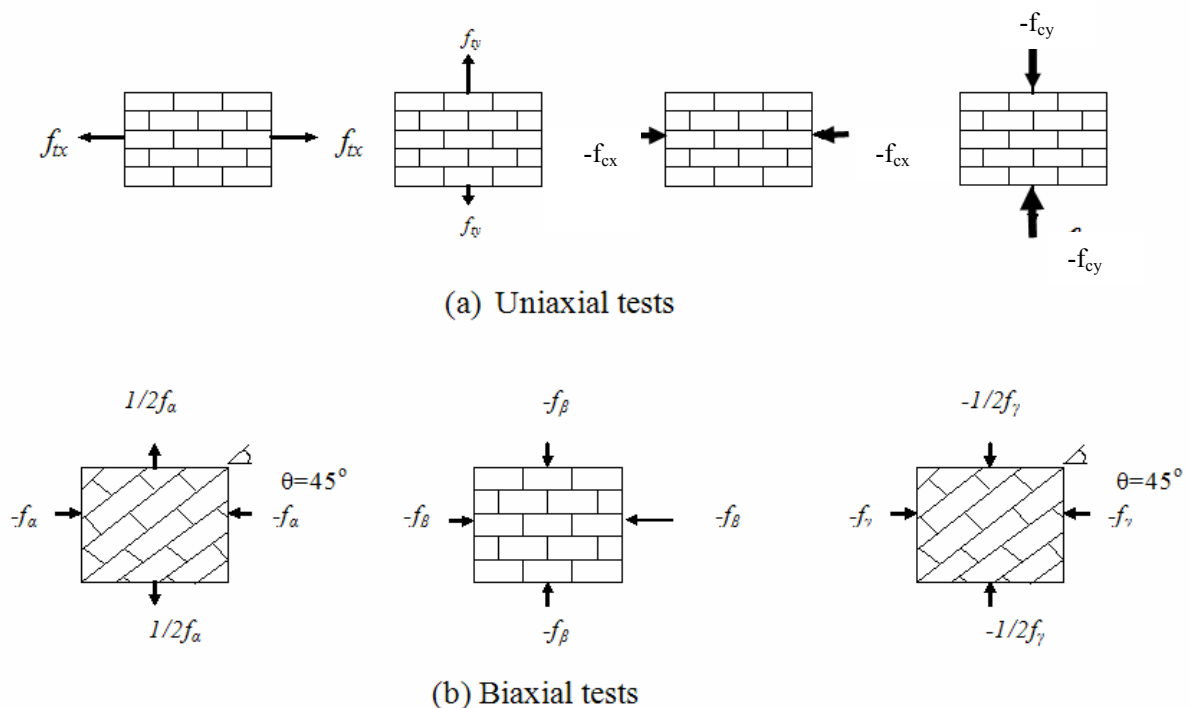


Figure 6.5: Tests for determining masonry parameters (Lourenco (1996))

In addition to strength and energy parameters, shear stress contribution to tension failure parameter (α), a biaxial compressive strength parameter (β) and a parameter (γ) that accounts for the shear stress contribution to compression failure are also determined using these tests. With these tests, the model parameters can be determined from the following equations:

$$\alpha = \frac{1}{9} \left(1 + 4 \frac{f_{tx}}{f_a} \right) \left(1 + 4 \frac{f_{ty}}{f_a} \right) \quad (6.13)$$

$$\beta = \left(\frac{1}{f_\beta^2} + \frac{1}{f_{cx}^2} + \frac{1}{f_{cy}^2} \right) f_{cx} f_{cy} \quad (6.14)$$

$$\gamma = \left(\frac{16}{f_\gamma^2} - 9 \left(\frac{1}{f_{cx}^2} + \frac{\beta}{f_{cx} f_{cy}} + \frac{1}{f_{cy}^2} \right) \right) f_{cx} f_{cy} \quad (6.15)$$

As displacement controlled biaxial tests (Fig. 6.5(b)) require an extensive test program, they have not been carried out as part of this thesis. Furthermore, it is believed that the effect of variations in material characteristics would only have minor effects on the behaviour of the masonry walls (sensitivity of material parameters is addressed later in this chapter).

6.4 Material Model for Grouted Reinforced Cores

The WSRM walls contain grouted reinforced cores in addition to the URM panels. For FE modelling of these walls, vertical reinforced grouted cores required careful modelling. Towards this end, a damaged concrete plasticity model for grout and a rebar option for reinforcement available in ABAQUS were adopted. A brief description of the concrete and reinforcement models used for the analysis of WSRM walls is provided in this section.

6.4.1 Grout Material Model

This isotropic damaged concrete plasticity model was used to represent grout. This model assumes that the grout fails due to two main failure mechanisms, namely ‘tensile cracking’ and ‘compressive crushing’. The yield surface is controlled by two hardening variables. These are tensile equivalent plastic strain and compressive equivalent plastic strain linked to the tension and compression failures respectively. Equivalent plastic strains are equal to the total strains less the elastic strains. This model assumes that failure of grout can be effectively modelled using its uniaxial tension, uniaxial compression and plasticity characteristics.

Under uniaxial tension, the stress-strain response follows a linear elastic relationship until the value of failure stress is reached. The failure stress corresponds to the onset of micro cracking in grout. Beyond the failure stress, the formation of micro-cracks is represented macroscopically with a softening stress-strain response, which induces strain localisation in the concrete structure. Typical uniaxial tension behaviour of grout is shown in Fig. 6.6(a).

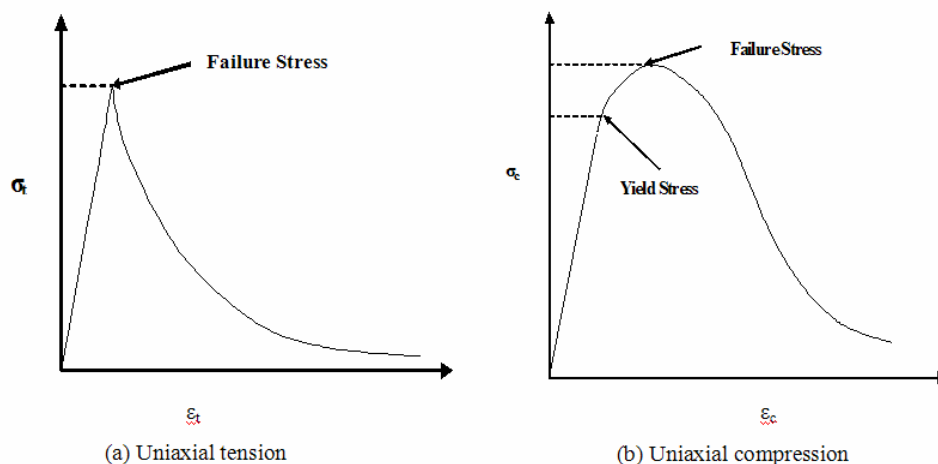


Figure 6.6: Stress strain curves for grout

Under uniaxial compression, the response remains linear until the initial value of yield stress is reached. In the plastic regime, the response is typically characterised by stress hardening

followed by strain softening beyond the failure stress. Typical behaviour of grout under uniaxial compression is shown in Fig. 6.6(b). These simplified representations of uniaxial tension and compression capture the main features of response of grout.

In reinforced grout, the specification of post failure behaviour generally represents the post failure stress as a function of cracking strain (Fig. 6.6(a)). Stress-strain data for uniaxial compression and stress-cracking strain data for tension stiffening are provided in Table 6.1.

Table 6.1: Compression hardening and tension stiffening data for grout

Grout Compression Hardening		Tension Stiffening	
Compressive Stress (MPa)	Inelastic Strain	Tensile Stress (MPa)	Cracking strain
9.00	0.0000	1.60	0.0000
13.50	0.0080	1.0	0.00016
13.70	0.0016	0.50	0.00025
4.00	0.0027	0.20	0.00050
		0.10	0.00100

In addition to the compressive and tensile stress-strain data, this material model requires dilation angle, flow potential eccentricity, ratio of initial equi-biaxial compressive yield stress to initial uniaxial compressive yield stress (σ_{bo}/σ_{co}) and ratio of the second stress invariant on the tensile meridian to that on the compressive meridian. Details of these parameters can be found in ABAQUS (2005) Theory Manual. The value of dilation angle for grout was set equal to 36 degrees and default values for the other three parameters were set equal to 0.1, 1.16 and 0.67 respectively for the analysis of WSRM walls.

For compression hardening data, peak compressive strength was set equal to the average prism strength whereas for the tension stiffening data, peak tensile strength was assumed equal to the weighted average of tensile strength of grout and unreinforced masonry in the grouted core.

Tensile strength of the grout and unreinforced masonry were taken equal to 4.0MPa and 0.35 MPa respectively and the cross sectional area of the grout and unreinforced masonry were equal to 8,000mm² and 15,250mm² respectively. Typical values of strains at peak compressive strength and at maximum tensile strength for the grouted masonry were set equal to 0.0016 and 0.0001 respectively.

6.4.2 Reinforcement Material Model

Reinforcing bars were modelled using the REBAR option available in ABAQUS (2005). As per this model, the rebars are integrated at one or two points, depending on the order of interpolation in the underlying elements. For the reduced integration linear plane stress (CPS4R) elements used in the analysis of the WSRM walls, the rebar “element” was integrated at its centroid (single point only). Formulation of rebars used in this study can be found in the ABAQUS (2005) Theory Manual. Modelling of rebars for four noded plane stress elements (CPS4R) is shown in Fig. 6.7. The arrows represent the direction of specifying node numbers for elements. Node numbers and edge numbers are also shown in this figure.

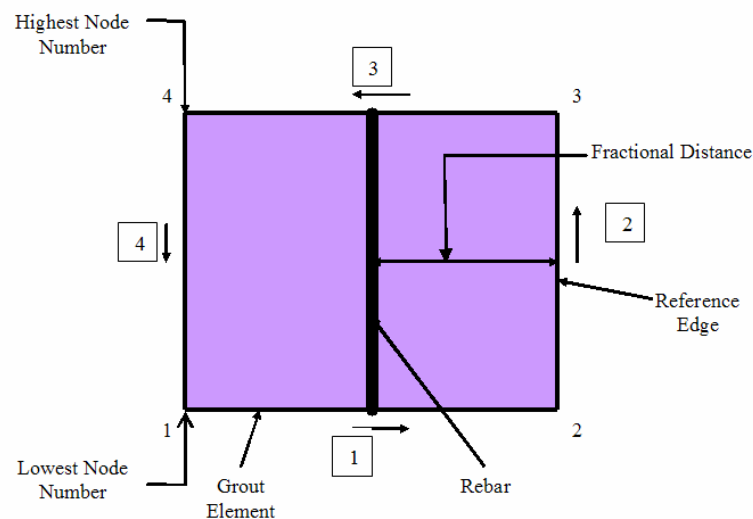


Figure 6.7: Layout of reinforcement bars on top of 4-noded plane stress element

To overlap reinforcement bars on top of the two dimensional reduced integration plane stress grout elements the following data were provided to the input file: Name of the set of the grouted elements, cross-sectional area of the bar in the element set (110mm^2), rebar spacing along the thickness of the elements (150mm), orientation of the rebar in the element (0°), reference number of the edge (2), fractional distance from the edge (ratio of the distance between the edge and the rebar to the distance across the element = 0.5). The stress-strain curve of the reinforcement bar under tension and compression is shown in Fig. 6.8.

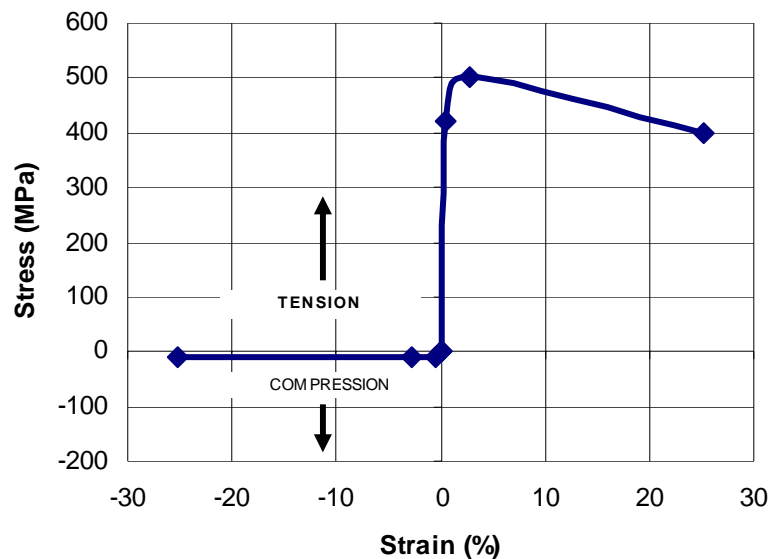


Figure 6.8: Stress-strain data for reinforcing bars

Capability of the reinforcement bars under compression was disabled as shown in Fig. 6.8 to allow buckling of the bars. This was essential because in practical WSRM walls the reinforcement bars do not have any lateral confinement. This model enabled the full tension (500MPa) capability of the reinforcement bars and reduced their compression capability to only 2% of its yield strength (10MPa).

6.5 Nonlinear Solution Technique: Explicit Formulation

The explicit method of structural analysis is essentially suitable for high frequency dynamic events such as impact and collision. This method also has the capability of approximately modelling static events and hence was adopted here. It uses a consistent, large deformation theory allowing models to undergo large rotations and large deformations. It is computationally efficient for the analysis of large models with relatively short dynamic response times and for the analysis of extremely discontinuous events.

This method allows numerical solutions without the formulation of structural stiffness matrices. An explicit central difference time integration rule and diagonal element mass matrices are used in the analysis process. The explicit central difference time integration rule is used to satisfy dynamic equilibrium equations and requires nodal mass or inertia to exist at all activated degrees of freedom.

6.5.1 Basics of Explicit Finite Element Formulation

The explicit central difference operator satisfies the dynamic equilibrium equations at the beginning of the increment at time 't'. Accelerations (in three directions) calculated at time 't' are used to determine the velocity solution to time 't+Δt/2' and displacement solution through explicit integration without any regard to whole structural stiffness matrices. Kinematic conditions at one increment are used to calculate the kinematic conditions at the next increment. Dynamic equilibrium is solved at the beginning of the increment as:

$$M a = P - I \quad (6.16)$$

where ' M ' is the nodal mass matrix, ' a ' is the nodal acceleration, ' P ' is the external applied force, and ' I ' is the internal element forces. The accelerations at the beginning of the current increment (at time t) are calculated by the following equation:

$$a_{(t)} = (M)^{-1} \cdot (P - I)_t \quad (6.17)$$

The accelerations of any node are determined completely by its mass and the net force acting on it, making the nodal calculations very simple and inexpensive. The accelerations are integrated through time using the central difference rule, which calculates the change in velocity assuming that the acceleration is constant. This change in velocity is added to the velocity from the middle of the previous increment to determine the velocities at the middle of the current increment by the following relation:

$$V_{(t + \frac{\Delta t}{2})} = V_{(t - \frac{\Delta t}{2})} + \frac{\Delta t_{(t+\Delta t)} + \Delta t_{(t)}}{2} a_{(t)} \quad (6.18)$$

The velocities are integrated through time and added to the displacement at the beginning of the increment to determine the displacement at the end of the increment as follows:

$$d_{(t + \Delta t)} = d_{(t)} + \Delta t V_{(t+\Delta t)} V_{(t + \frac{\Delta t}{2})} \quad (6.19)$$

The term explicit refers to the fact that the state at the end of the increment is based solely on the displacement, velocities and accelerations at the beginning of the increment. For the method to produce accurate results, the time increments must be quite small so that the accelerations are nearly constant during an increment. Once displacements are calculated from Eq. 6.19, the strains are calculated and in turn element stresses are calculated by applying material constitutive relationships from Eq. 6.20.

$$\sigma_{(t + \Delta t)} = f(\sigma_{(t)}, d\varepsilon) \quad (6.20)$$

The maximum time increment used by Explicit Solver related to the stability limit of the structure globally is calculated from Eq. 6.21.

$$\Delta t_{stable} = \frac{2}{\omega_{max}} \quad (6.21)$$

where ' ω_{max} ' is the highest frequency in the structure. The actual highest frequency in the structure is based on a complex set of interacting factors, and it is not computationally feasible to calculate its exact value; however, a simple estimate is determined on an element-by-element basis and is calculated from Eq. 6.22.

$$\Delta t_{stable} = \frac{L_e}{C_d} \quad (6.22)$$

where ' L_e ' is the element length and ' C_d ' is the wave speed of the material and is calculated from Eq. 6.23.

$$C_d = \sqrt{\frac{E}{\rho}} \quad (6.23)$$

where ' E ' is the Young's modulus and ' ρ ' is the mass density of the material. Although wave speed (and hence the natural frequency or period) could be approximately determined from Eq. 6.23, more detailed frequency analysis was carried out as a routine due to its simplicity and availability of mesh for other purposes.

6.5.2 Frequency Analysis

Natural frequency analysis is a linear perturbation procedure, which performs Eigen value extraction to calculate the natural frequencies and the corresponding mode shapes of a dynamic

system. Lanczos and subspace iteration are the two methods which are used to determine the Eigen values to extract the natural frequencies of the system. The Lanczos method is generally faster when a large number of Eigen modes are required for a system with many degrees of freedom (DOF). Since in the analysis of WSRM shear walls, a large number of DOF are involved, the Lanczos method was adopted. Details of the Lanczos solver can be found in the ABAQUS (2005) Theory Manual. The Eigen value problem for the natural frequencies of an undamped finite element model is given by

$$(-\omega^2 [M^{mn}] + [K^{mn}]) \zeta = 0 \quad (6.24)$$

where ' M ' is a symmetric, positive definite mass matrix, ' K^{mn} ' is a stiffness matrix, ' ζ ' is the Eigen vector or the mode of vibration, ' ω ' is frequency, ' m ' and ' n ' are degrees of freedom of the system. Once the natural frequency of the system for the lowest mode is determined, the time period (TP) of the system is calculated for the static analysis of the system simply by inverting the frequency as shown in Eq. 6.25.

$$T P = 1 / \omega \quad (6.25)$$

6.5.3 Method of Modelling

Although the explicit solution method is a true dynamic procedure originally developed to model high speed impact events in which inertia plays a dominant role in the solution, it has also proven valuable in solving static problems. Applying the explicit dynamic procedure to static problems requires some special considerations.

Since a static solution by definition considers the time period, it is often computationally impractical to simulate the analysis in its natural time scale, as it would require an excessive number of small time increments. To obtain an economical solution, the event needs to be

accelerated in some way. The problem is that, as the event is accelerated, the state of static equilibrium evolves into a state of dynamic equilibrium in which inertial forces become more dominant. This problem can be overcome by making use of one or a combination of the following options:

- Artificially increase the loading rate so that the physical event occurs in less time as long as the solution remains nearly the same and the true static solution and dynamic effects remain insignificant. This option causes the velocities and the kinetic energy to equal zero.
- Artificially increase the mass density of the elements to increase the stability limit of the structure. This option has the same effect as the loading rate. As per Eq. 6.23, artificially increasing the mass density by a factor of ' g^2 ', decreases the wave speed by a factor of ' g ' and increases the stable time by a factor of ' g ', which in turn increases the stability limit of the structure. This option is more useful when the elements in critical zones of the structures are badly distorted or material is rate dependent.

For accuracy and efficiency, static analysis requires the application of loading that is as smooth as possible. Sudden, jerky movements cause stress waves, which could induce noisy or inaccurate solutions. Applying the load in the smoothest possible manner requires that the acceleration change only a small amount from one increment to the subsequent one. If the acceleration is smooth, it follows that the changes in velocity and displacement also become smooth. It is usually desirable to increase the loading time to 10 or even more times the period of the lowest mode to be certain that the solution remains truly static.

To improve the results even further, a smooth step amplitude curve as shown in Fig. 6.9 is used that creates smooth loading amplitude. Step type amplitude curves cause jumps in the application of loading.

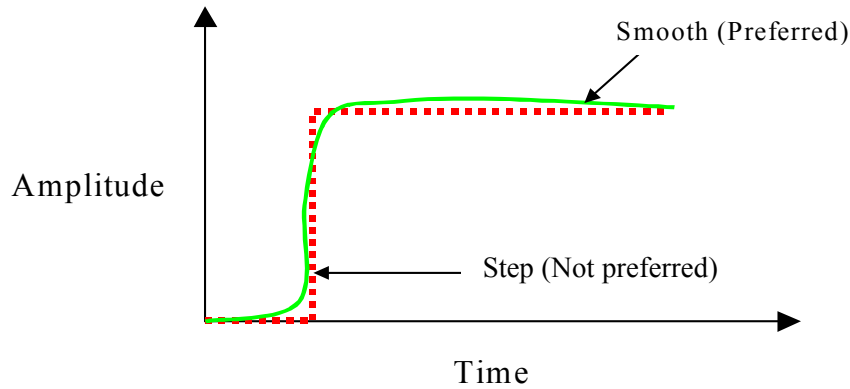


Figure 6.9: Smooth and step type amplitude curves

The most general means of evaluating whether or not the explicit analysis produces an appropriate static response are to ensure satisfaction of the energy balance rule as shown in Eq. 6.26.

$$E_I + E_V + E_{KE} + E_{FD} - E_W = E_{total} \quad (6.26)$$

where ' E_I ' is the internal energy and is equal to the sum of the elastic and plastic strain energy, ' E_V ', is the energy absorbed by viscous damping, ' E_{KE} ' is the kinetic energy during the load application, ' E_{FD} ' is the energy absorbed by frictional dissipation, ' E_W ' is the work of external forces and ' E_{total} ' is the total energy in the structure.

Another requirement for the appropriateness of the static solution is that the kinetic energy of the deforming material should remain low, typically below 10% of the internal energy throughout the simulation.

6.6 Process for the Non-linear Analysis of WSRM Walls

The procedure for the non-linear analysis of the WSRM walls is discussed in this section. A flow diagram of the various steps of the analysis procedure is presented in Fig. 6.10.

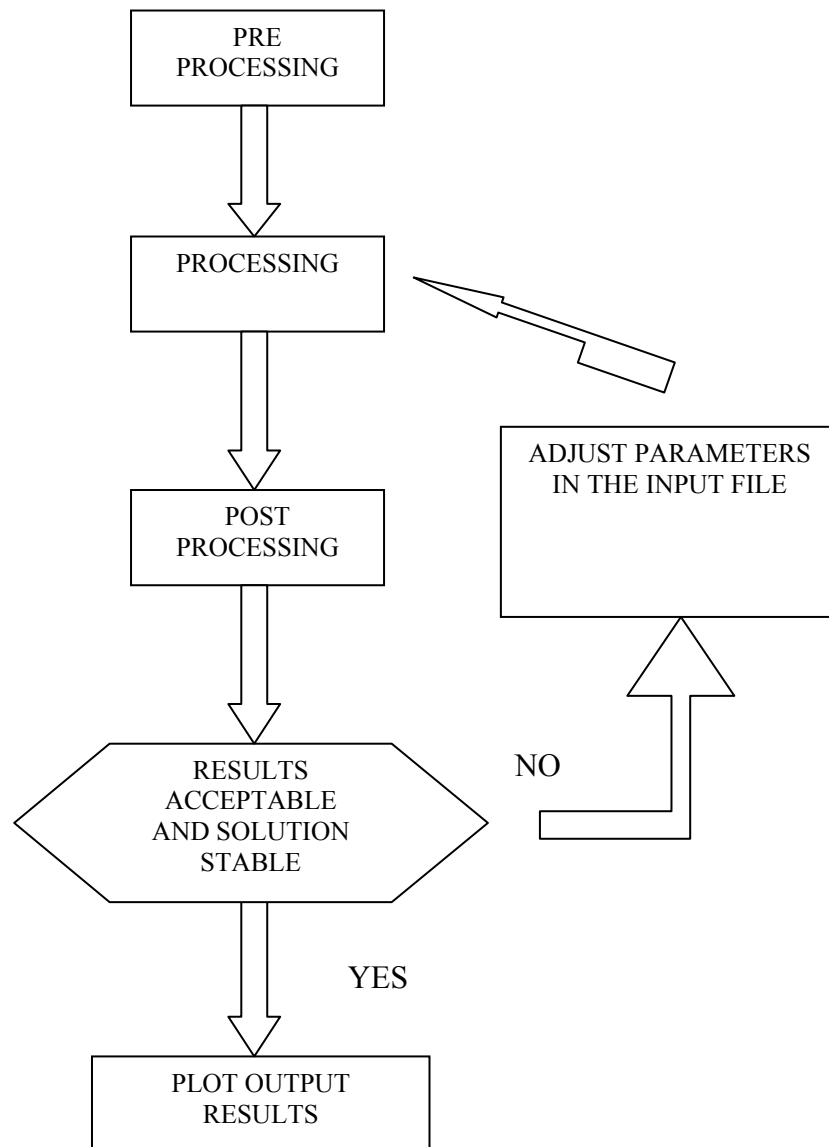


Figure 6.10: Flow diagram of steps involved in the non-linear analysis of WSRM walls

Details of the pre-processing, processing and post-processing are discussed in this section.

6.6.1 Pre-Processing

A flow chart of the steps involved in creating the INPUT file for the analysis of the WSRM wall is presented in Fig. 6.11.

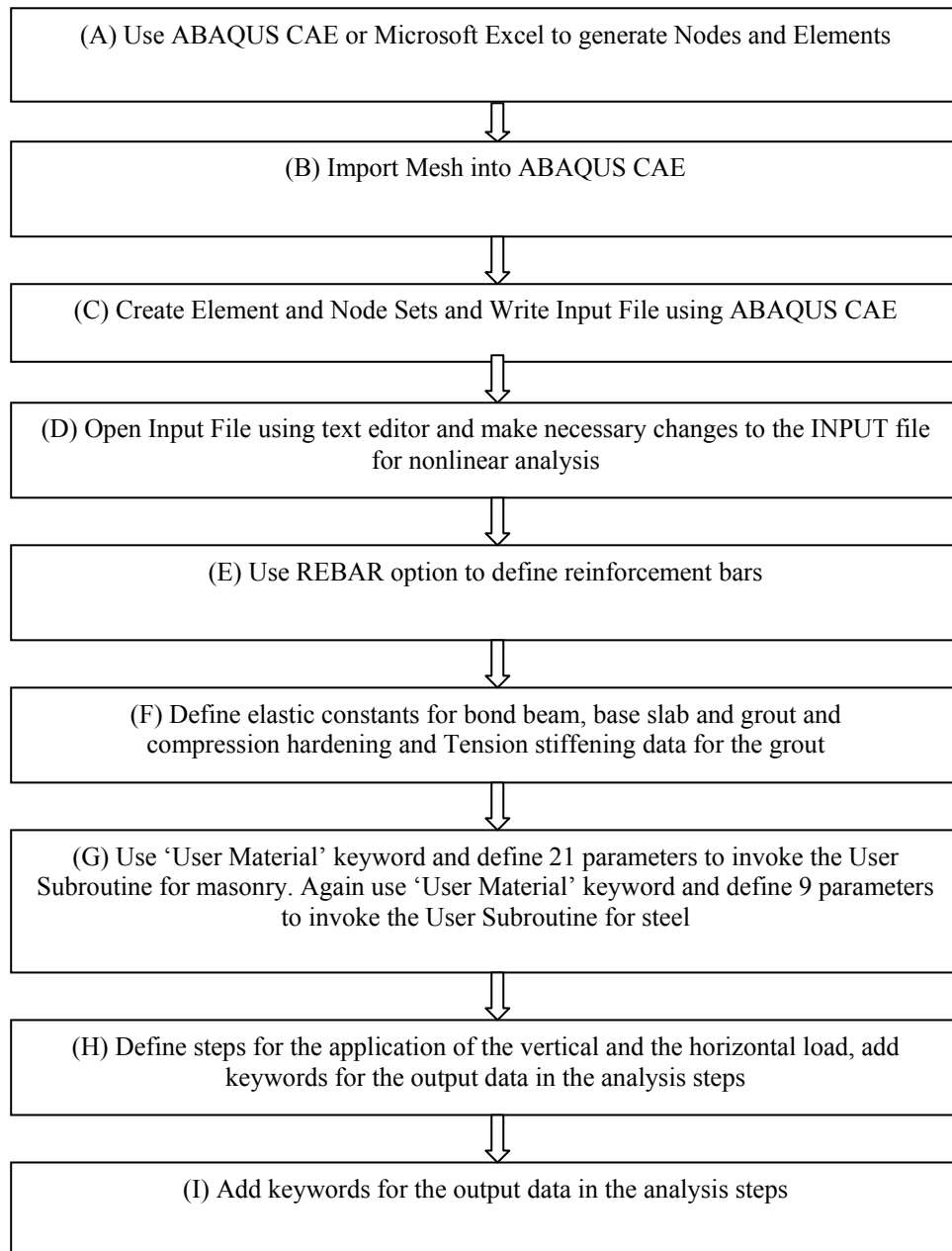


Figure 6.11: Flow diagram of steps involved in pre-processing

Steps involved in pre-processing presented in Fig. 6.11 are briefly discussed herein:

(A) Either ABAQUS CAE or Microsoft Excel can be used for preparing the input file. For the analysis of the masonry walls discussed in this thesis, Microsoft Excel was used. In the Microsoft Excel worksheet, *NODE was typed in the first column of the first row and 1 was typed for Node 1 in the first column of the second row, 'x' and 'y' coordinates of node 1 were typed respectively in the second and third columns of the second row. Equation capability available in Excel was used to generate a table of the required number of nodes and the corresponding coordinates. '*Element, type=CPS4R' was typed in the first column of the row next to the table of nodes and their coordinates.

Element number was typed in the first column and its node numbers in the next four columns. Node numbers were written in the counter clockwise orientation. Equation capability available in Excel was used to generate a table of the total number of elements. The worksheet was saved as a CSV file and then opened in a text editor. All the stars were deleted from the file except one star before keyword Node and one star before keyword Element and the file was saved with an extension of INP (for example WSRM.INP)

(B) The import function on the file bar of ABAQUS CAE was used to import the mesh of the wall created in step (A).

(C) The TOOLS bar of CAE was used to create element sets for the bond beam, the base slab, unreinforced masonry, vertical grouted cores and node sets for the bottom of the base slab. The TOOLS bar of CAE was also used to define boundary condition and set of nodes at the end of the bond beam for the application of the horizontal load. Job menu of CAE was used to write an input file (for example WSRM-A.inp) containing the element and node sets.

- (D) The input file (WSRM-A.inp) was opened and all the unnecessary data were deleted from the file. This has been essential because the CAE writes some unnecessary data that sometimes creates trouble in the analysis of the data used by ABAQUS solvers (Explicit and Implicit). Separate lines were used to define thicknesses of different sections of the wall. For example “*Solid Section, elset=HOLLOW MASONRY, material=MASONRY on the first line and 70 on the next line”. The thickness of the hollow masonry was defined equal to 70mm. Top surface of the bond beam, boundary conditions; amplitude curves (Definition =smooth) were defined for the vertical and the horizontal load application. For boundary conditions, the bottom nodes of the base slab were constrained against the x and y direction movements.
- (E) The REBAR option was used to define element sets (sets of vertical grouted cores) that contain reinforcement bars, area of the reinforcement bars, location of the reinforcement bars in the thickness direction of the underlying elements, orientation of the reinforcement bar and edge number of the underlying element to the reference of the reinforcement bar.
- (F) Elastic properties (Young’s modulus and Poisson’s ratio) of bond beam, base slab and grout, and the compression hardening and tension stiffening data of the composite section of the grout and hollow masonry block were defined.
- (G) The keyword ‘User Material’ and 21 constants were then typed to invoke the subroutine for unreinforced masonry. A list of the 21 parameters is provided later in this chapter. Again the keyword “User Material” and 9 constants (Young’s modulus ($E_s=200,000\text{MPa}$), area of the reinforcement bar ($A_s=110\text{mm}^2$), yield strength of the reinforcement bar in tension ($S_y=420\text{MPa}$), ultimate tensile strength of the bar ($S_{tu}=500\text{MPa}$), failure stress of the bar ($S_{tf}=400\text{MPa}$), ultimate compressive strength of

the bar (S_{cy} , S_{cu} , $S_{cf}=10\text{MPa}$), strain at tensile yield strength of the bar ($\epsilon_{sy} = 0.004$), strain at peak tensile strength of the bar ($\epsilon_{su} = 0.025$), strain at failure tensile strength of the bar ($\epsilon_{sf} = 0.252$)) for the reinforcement bar were defined to invoke the user subroutine for steel.

A keyword ‘*DEPVAR’ was applied in the input file to invoke the number of solution dependent state variables. For plane stress elements used for masonry, its value was equal to ‘2’ for stress along y -axis and x -axis whereas it is equal to ‘1’ for steel bar due to only uniaxial stress.

- (H) Vertical load was applied in a single step and the horizontal displacement in multi steps using keywords (Dynamic, Explicit) along with time period and bulk viscosity parameters and corresponding amplitude curves. For each millimetre of the horizontal displacement, a separate step was defined. For the vertical load application a keyword (*DSLOAD) was used and the magnitude of the vertical stress (0.5MPa) on the top surface of the bond beam was defined. For the horizontal load application, a keyword ‘*BOUNDARY’ and magnitude of the intended horizontal displacement (1mm for each step) were used.
- (I) In each step, history and field output keywords were used to write output (stresses, strains, energy, reaction forces etc.) using *ELSET and *NODE SET for the whole model to the field output database and for the selected nodes and elements to the history database.

6.6.2 Processing

The VUMAT interface available in ABAQUS/Explicit links the user material subroutine with the FE analysis program. To link the user material subroutine (USERMAT) developed by Lourenco (1996) for masonry material to ABAQUS (2005), a FORTRAN program was written.

Since the Explicit integration program requires stress component calculations directly, the FORTRAN program linked only the calculation of stresses to ABAQUS. The material model for the reinforcement bars in the VUMAT subroutine was included as a separate subroutine to provide capability to the steel bars to yield in tension or buckle under compression due to lack of lateral reinforcement as shown in Fig. 6.8.

The ABAQUS (2005) program calculates the characteristic length of the elements internally; the characteristic length in the FORTRAN program was output to monitor its value. Listing of the VUMAT subroutine is provided in Appendix D. A flow diagram that describes the processing of the data provided through the input file and the user subroutines is shown in Fig. 6.12.

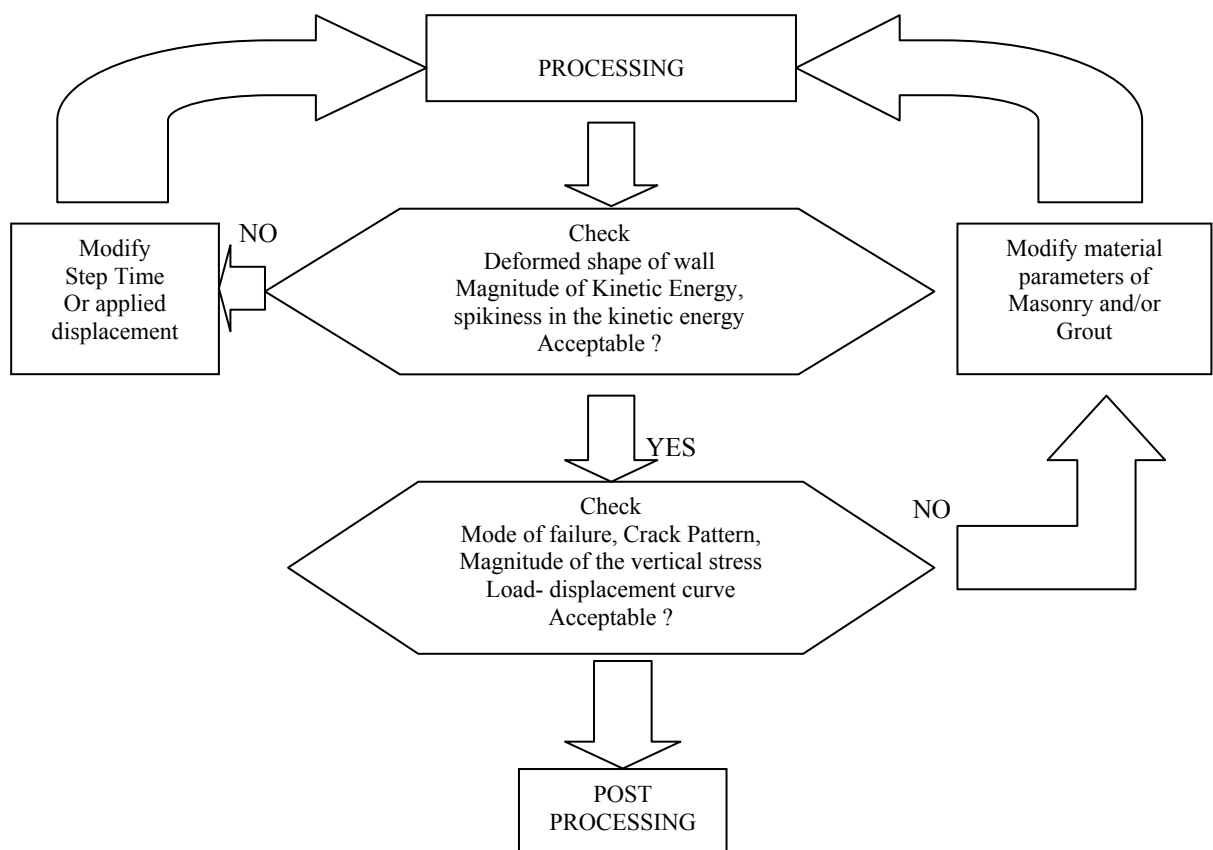


Figure 6.12: Flow diagram of the process for the analysis of masonry walls

In the DOS command box, 'job= *Name of the file containing input data*, user= *Name of the file containing user subroutine interactive*' was typed to run the analysis. Upon completion or termination of the analysis, the output database (ODB) file was opened in ABAQUS CAE and the results were viewed. The time period in the steps for the application of the horizontal displacement was adjusted until the solution became stable. Energy criterion (kinetic energy less than 10% of the internal energy, and smooth kinetic energy during the whole analysis) was checked. Spikiness in the kinetic energy was accepted as this was due to tensile cracking of masonry. Twenty one parameters of the masonry material were modified until the load-displacement curve and the crack pattern (vector plots of logarithmic strains and principal stresses) of the WSRM wall matched with that obtained from the experiments.

6.6.3 Post-Processing

The ODB file was opened in ABAQUS CAE interface and the results were viewed. Reaction forces at all the nodes of the bond beam where the horizontal displacement was applied were extracted and summed up to view the load-displacement curve of the wall using displacement at one of the nodes where the horizontal displacement was applied.

Contours and vector plots of stresses and strains were viewed to examine the load flow, shape of the deformed structure, and magnitude of the logarithmic strains.

Various types of energy required for the energy balance check, magnitude of stresses for critical regions (the heel, the toe, and the centre), vector plots of principal stresses and principal logarithmic strains were also extracted. Using the REPORT menu of the CAE, numerical data were written to a text file, which was opened in a Microsoft Excel worksheet and the plots for the stresses and load-displacement curves were drawn. Vector plots of principal stresses and

logarithmic principal strains were printed to files that were later opened through IMAGING program and then they were copied and pasted to the Microsoft word file.

6.7 WSRM Wall Modelling, Analysis and Results

Macro modelling was adopted for the analysis of WSRM walls. Since all the masonry walls discussed in this thesis were constructed from hollow clay blocks with face shell mortar bedding, effective thickness of the URM was taken equal to 70mm (sum of thickness of two shells) in the finite element model. The presence of horizontal bed joints and vertical joints in the URM demands a careful meshing strategy for macro modelling of the masonry walls. The meshing strategy for the WSRM walls is discussed in this section. Frequency analysis, static analysis, load-displacement response and step-by-step stress state are discussed in this section.

6.7.1 Meshing

Macro material modelling for masonry (Samarasinghe et al. (1981), Dhanasekar (1985), Lourenco (1996)) has been developed by testing masonry panels that contain mortar joints in the horizontal as well as in the vertical direction. Therefore to use the macro model for masonry, it becomes mandatory to generate mesh in such a way that each element contains at least a portion of horizontal as well as vertical mortar joint surrounding the masonry unit. In the present study, all the walls were constructed from 150mm thick, 76mm high and 310mm long hollow clay blocks. Therefore, the horizontal mortar joints and the vertical mortar joints were spaced at approximately 315mm and 81mm respectively.

Coarse, medium and fine meshes were generated for the analysis of the WSRM wall as shown in Fig. 6.13. The coarse mesh consisted of plane stress elements of length 407mm in the end panels and 310mm in the middle panel. Height of all the elements was equal to 224.1mm. In this mesh each element contained at least a block or little more than a block along the length and

approximately two and a half blocks along the height. This mesh had 60 elements in the masonry, 10 elements in the bond beam and 12 elements in the base slab. Length and height of elements in the grouted cores were equal to 155mm and 224.1mm respectively.

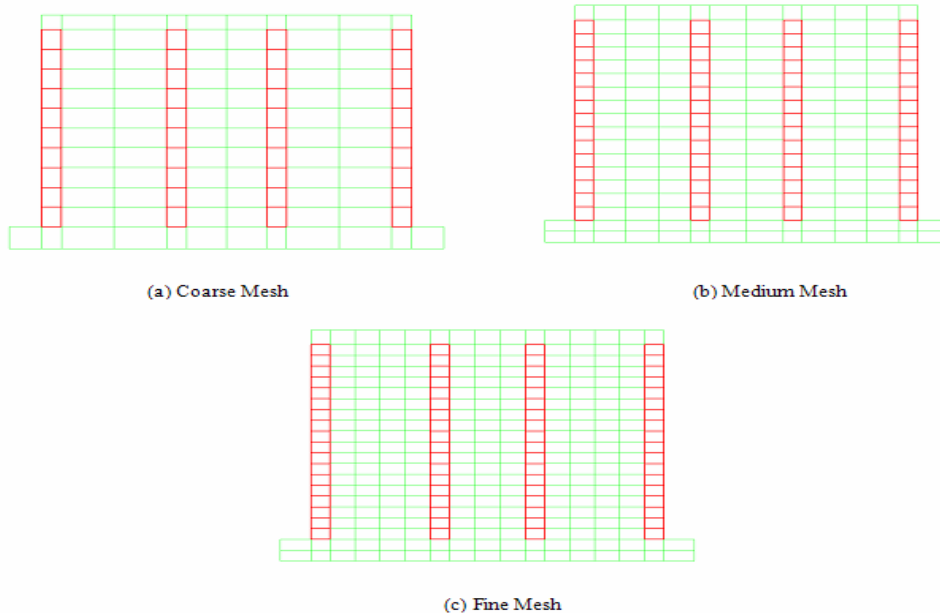


Figure 6.13: Meshes adopted for the analysis of WSRM wall

The medium mesh consisted of plane stress elements of length 271.1mm in the end panels and 310mm in the middle panel. Height of all the elements was equal to 149.4mm. In this mesh each element contained at least a block or three quarters of a block along the length and approximately two blocks along the height. This mesh had 120 elements in the masonry, 12 elements in the bond beam and 14 elements in the base slab. Length and height of elements in the grouted cores was equal to 155mm and 149.4mm respectively.

The fine mesh consisted of plane stress elements of length 203.75mm in the end panels and 206.7mm in the middle panel. Height of all the elements was equal to 124.5mm. In this mesh each element contained two thirds of a block along the length and approximately one and a half blocks along the height. This mesh had 198 elements in the masonry, 15 elements in the bond

beam and 17 elements in the base slab. Length and height of elements in the grouted cores was equal to 155mm and 124.5mm respectively. Details of medium mesh are shown in Fig. 6.14.

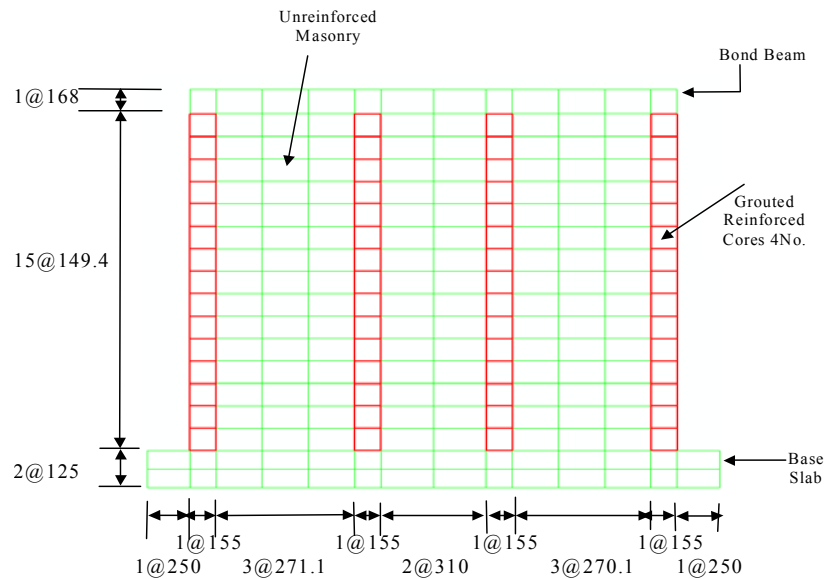


Figure 6.14: Details of medium mesh used for the analysis of WSRM wall

One element was modelled for the full height of the bond beam and two elements for the full thickness of the base slab. The width of elements in the bond beam and in the base slab was kept similar to the elements used for the wall for uniformity of the mesh.

All the meshes were generated with a common assumption that masonry was uniform for the full wall disregarding the hollow or solid cores of masonry, which is appropriate for face shell bedded construction.

6.7.2 Frequency Analysis of WSRM Wall

Explicit analysis requires knowledge of the natural time period of the structure. To determine the natural time period of the WSRM wall, a frequency analysis was performed for all the three meshes individually and natural frequency was found for the first 10 modes of vibration.

Since frequency analysis is purely a linear perturbation type analysis, it required only linear elastic properties of the elements. An option available in ABAQUS for defining the orthotropic elastic properties of materials was utilised. For this purpose, orientation of the structure was defined first and then a key word (*ELASTIC in combination with LAMINA) was used to define orthotropic elastic constants of masonry. Elastic modulus (E_x) parallel to the bed joints was selected as 6,000MPa and normal to the bed joints (E_y) as 15,000MPa. Poisson's ratio (ν) along both the x and y directions was equal to of 0.20. Shear modulus (G) calculated from Eq. 6.27 was equal to 3,953MPa.

$$G = \frac{\sqrt{E_x E_y}}{2(1+\nu)} \quad (6.27)$$

Isotropic elastic modulus for the bond beam and the base slab was equal to 30,000MPa and 35,000MPa respectively with Poisson's ratio of 0.25. Thickness of the URM, the bond beam and the base slabs was equal to 70mm, 150mm and 1000mm respectively.

The first modes of vibration of the WSRM wall for the coarse, the medium and the fine mesh are shown in Fig. 6.15.

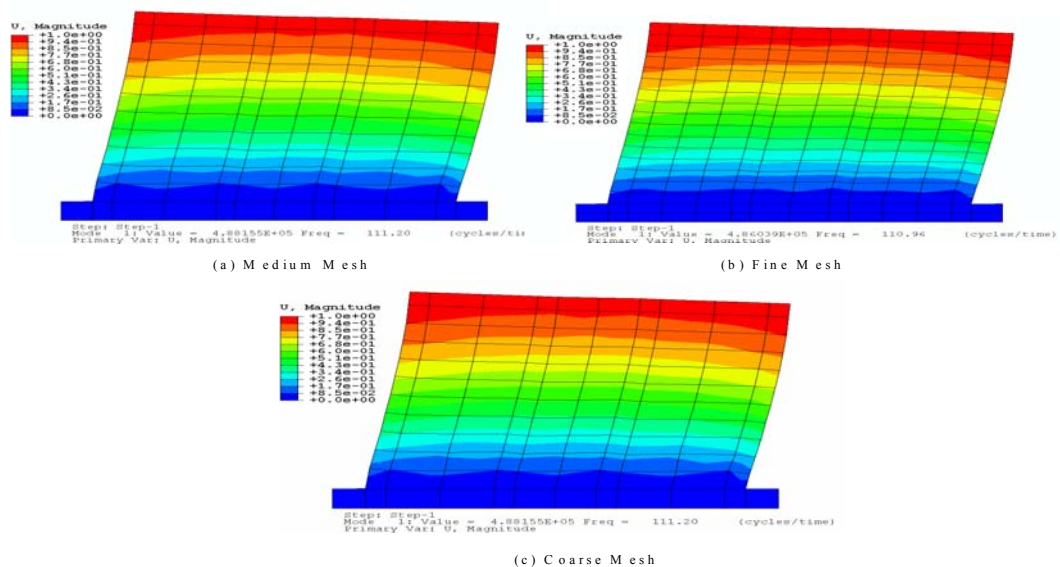


Figure 6.15: First mode of vibration of WSRM wall

The natural frequencies of the WSRM wall determined using the coarse, the medium and the fine mesh were 111.2Hz, 112.2 Hz and 111.0 Hz respectively. The corresponding time periods were all approximately equal to 0.009sec.

6.7.3 Analysis of WSRM Wall

Analysis in ABAQUS/Explicit requires artificial increase in the time period or increase in the mass density of structures to minimise the dynamic effects and to achieve stable solutions. Options available in ABAQUS for increasing the stability limit of structures include:

- Increase in natural time period of the structure (by a factor of 10 or higher)
- Increase in the bulk viscosity
- Damping factor (increase in damping related to mass and/or stiffness)
- Mass scaling of elements in the critical zones of the wall

Among all the options available in ABAQUS for artificial increase of stability limit of structures, increase in natural time period of the wall was found efficient. Since the mesh was more uniform, increase in the time period was found easy to implement.

The calculated time period was increased to approximately 10 times for the application of the vertical load and then approximately 100 times for the application for the horizontal load to ensure that the magnitude of peak *kinetic energy* remained insignificant relative to *internal energy*. A smooth step definition was used in addition to the increased time period to avoid jerky movements and produce stable solutions. Horizontal displacement was applied in multi steps, which also helped to ensure stable solutions.

In the absence of material tests for masonry used for the URM, the required material parameters were collected from the literature. This approach was considered sensible as:

- (1) Masonry material data for average Australian workmanship are reasonably well reported over the past three decades.
- (2) Masonry properties are highly variable and an average property would be indicative of the current construction.
- (3) Structural response of masonry walls containing reinforcement is not significantly affected by the accuracy of the material data set.
- (4) Material property determination especially from biaxial displacement controlled tests is expensive and time consuming.

Values of all other parameters adopted for the analysis of the WSRM wall were close to those found in the literature (Dhanasekar (1985), Page (1982), (Lourenco (1996)). Compressive strength of this same type of masonry perpendicular to the bed joints (face shell bedding) found earlier by Kumar (1995) was adopted in the model. The bond beam and base slab were kept as elastic bodies; therefore the elastic constants adopted in the frequency analysis were used in the nonlinear explicit analysis.

21 parameters were required for the analysis of the wall. A brief description of these parameters is provided in Table 6.2. A factor equal to $\sqrt{2}$ was multiplied with the calculated characteristic length to account for the linear elements (plane stress elements CPS4R) in ABAQUS/Explicit. Energy for compression failure parallel to the bed joints (G_{fcx}) and normal to the bed joints (G_{fcy}) was calculated from Eq. 6.12 whereas the fracture energies (G_{fx} , G_{fy}) were calculated from Eq. 6.7.

For fracture energies, characteristic length criterion given in Eq. 6.7 were not strictly followed in the explicit analysis of the WSRM and Non-WSRM walls due to reasons discussed in section 6.3.1. In this thesis for the analysis of the WSRM walls, calculated values of characteristic lengths of the masonry elements were multiplied by a factor for x-direction (k_x) and by a factor for y-direction (k_y) to calculate the energy required to obtain stable solutions. Values of ' k_x ' and ' k_y ' were equal to 60 and 50 respectively.

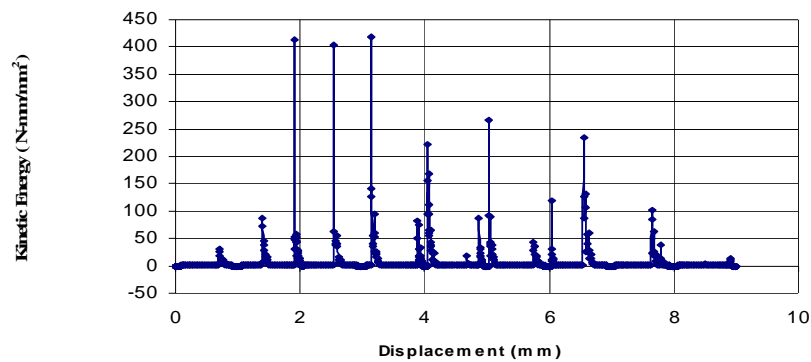
Table 6.2: Material parameters for unreinforced masonry

No.	Parameter	Value	Units	Description
1	f_{tx}	0.60	MPa	Tensile strength parallel to bed joints
2	G_{fx}	1.00	(N-mm/mm ²)	Fracture energy parallel to bed joints
3	f_{ty}	0.35	MPa	Tensile strength normal to bed joints
4	G_{fy}	0.50	(N-mm/mm ²)	Fracture energy normal to bed joints
5	α	1.25	-	Shear stress contribution factor to the tension failure
6	α_g	1.00	-	Mathematical variable for plastic flow of masonry
7	f_{cx}	3.00	MPa	Compressive strength parallel to bed joints
8	G_{fcx}	0.302	(N-mm/mm ²)	Energy for compression failure parallel to bed joints
9	f_{cy}	18.00	MPa	Compressive strength normal to bed joint
10	G_{fcy}	4.35	(N-mm/mm ²)	Energy for compression failure normal to bed joints
11	β	-1.17	-	Biaxial compressive strength factor
12	γ	4.00	-	Shear stress contribution factor to compression failure
13	h	+	mm	Characteristic length of critical elements (+ different values for different meshes)
14	K_p	0.0025	-	Strain at compression failure
15	E_x	6000	MPa	Young's Modulus of masonry parallel to bed joints
16	E_y	15000	MPa	Young's Modulus of masonry normal to bed joints
17	E_z^*	1e-3	MPa	Young's Modulus of masonry along thickness direction
18	ν_x	0.20	-	Poisson's Ratio of masonry parallel to bed joints
19	ν_y	0.20	-	Poisson's Ratio of masonry normal to bed joints
20	ν_z^*	1e-7	-	Poisson's Ratio of masonry along thickness direction
21	G	3953	MPa	Shear Modulus of masonry of masonry (Eq. 6.27)

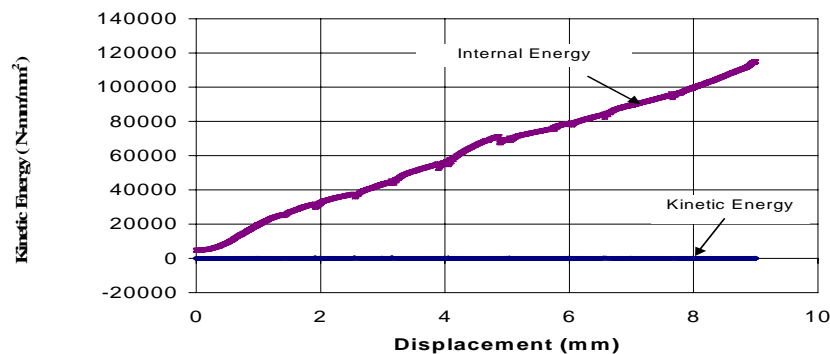
* For plane stress modelling, properties in the thickness direction are irrelevant.

Two amplitude curves were followed, one for the application of the vertical load and the other for the application of the horizontal load. This was attempted to apply the vertical load relatively faster, which was consistent with the experimental phase. The time period for the vertical load was 1/10 of that of 1mm of the horizontal displacement.

As a quality check of the analysis, energy plots are shown in Fig. 6.16. Kinetic energy was monitored throughout the analysis. Variation of kinetic energy versus the horizontal displacement for the medium mesh is shown in Fig. 6.16(a). During vertical load application, the magnitude of kinetic energy remained negligible; however, it marginally increased during the application of the horizontal load.



(a) Kinetic energy



(b) Internal and Kinetic energies

Figure 6.16: Comparison of energies dissipated during the analysis of WSRM wall

Fig. 6.16(a) shows the time series of kinetic energy in each step of the horizontal displacement. Kinetic energy remained smooth for each step of the horizontal displacement except that some spikes appeared whenever cracking of masonry and or grout occurred. Each spike in the kinetic energy was associated with cracking and a corresponding drop in lateral load. These spiky jumps in the kinetic energy show that the WSRM wall was able to regain the stable solution even after substantial cracking along its diagonal, which is a useful feature of the explicit solver.

Internal and kinetic energies are also plotted in Fig 6.16(b). A close review of the scale of the vertical axes of both graphs (Fig. 6.16(a), 6.16(b)) reveals that the magnitude of the kinetic energy remained in the hundreds whereas the internal energy was in the order of hundreds of thousands. Based on this observation, it is inferred that the analysis of the WSRM wall carried out using ABAQUS/Explicit is appropriate as it is assured that the inertia effects were successfully minimised. The other criterion of energy balance shown in Eq. 6.26 was also met. Meeting both the energy criteria shows that the increase in the time period as a means of achieving the solution was adequate.

6.7.4 Results and Discussion

Results of the analysis were post processed and are presented in this section. Load flow in the whole body of the WSRM wall, state of stress and strain in some selected elements and general crack patterns were the main focus of this presentation. Load-displacement response and stress state at various stages of horizontal displacement of the WSRM wall are discussed in this section.

6.7.4.1 Load-Displacement Response

The load-displacement response curve of six WSRM walls (#1 to #6) obtained from experiments is compared with that obtained from the FE model in Fig. 6.17.

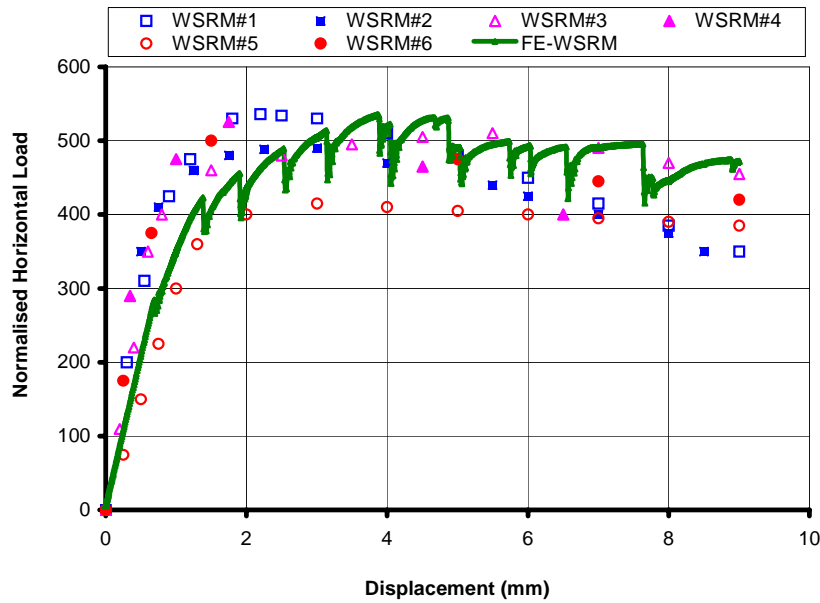


Figure 6.17: Load displacement response of WSRM walls

Experimental data for all the six WSRM walls (WSRM #1 to WSRM#6) are plotted in Fig. 6.17. Horizontal load was calculated as a sum of reaction forces at the nodes where the horizontal displacement was applied. The horizontal load thus determined was normalised using Eq. 6.28 to compare the load-displacement response with that obtained from experiments.

$$\text{Normalised Horizontal Load} = \frac{\text{Inplane Horizontal Load calculated by FE model}}{0.22\sqrt{f_m} \times A_g} \times 10^3 \quad (6.28)$$

where ' f_m ' is the peak value of compressive strength on the compression hardening data of the grouted masonry prisms. It was equal to 13.7 MPa for all the walls. ' A_g ' is the gross area of the wall and it was equal to 430,500mm².

It can be seen from Fig. 6.17 that the explicit analysis has successfully predicted the important characteristics of the load-displacement curve. The load displacement curve obtained from the FE model is in good agreement with that obtained from the experiments. Peak load and softening regime of the load-displacement curve show the capability of the model. The ductility

factor and the structural response factor (R_f) of the WSRM wall calculated from the load-displacement curve achieved from the FE model were 6.0 and 3.3 respectively. The load displacement curve provided in Fig. 6.17 was obtained using the medium mesh shown in Fig. 6.14. The load displacement curve obtained using the medium mesh is compared with those obtained using coarse mesh and fine mesh in Fig. 6.18.

Fracture and compression failure energies were calculated from Eqs. 6.7 and 6.12 respectively using the corresponding characteristic length of elements. Characteristic length factors (k_x and k_y) for the coarse and fine meshes were kept equal to those used for the medium mesh (60 and 50 respectively).

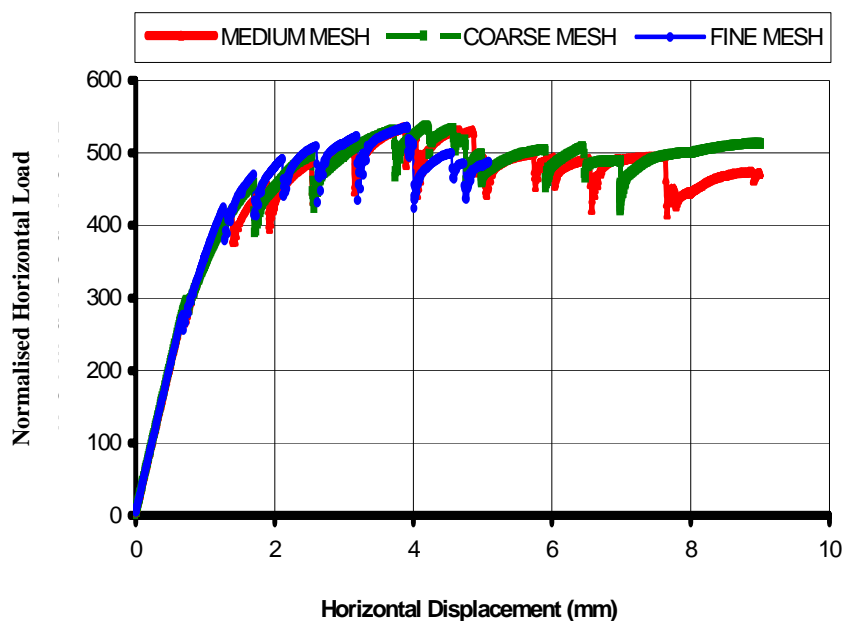


Figure 6.18: Effect of mesh size on load-displacement response

It is interesting to note from Fig. 6.18 that all the three meshes produced similar load-displacement responses until the peak load stage. Elastic and hardening regimes of the load-displacement curve matched very well for all the three meshes. The coarse and the medium

meshes were able to predict a large load-displacement response up to 9mm whereas the fine mesh produced a load-displacement response up to 5mm only.

Differences in the softening regime may be attributed to the bifurcation of solutions due to localisation in a zero volume, resulting in a wrong solution path. This fundamental problem for the isotropic and anisotropic materials has been addressed by Kozar and Bicanic (1999).

The medium mesh showed reasonable softening, which was in good agreement with that obtained from the experiments. Therefore, the analyses results obtained using medium mesh were post processed and used for the comparison purposes.

Sensitivity of the characteristic length factors (k_x , and k_y) used in the calculation of characteristic lengths of the URM elements was then investigated and the results are presented in Fig. 6.19.

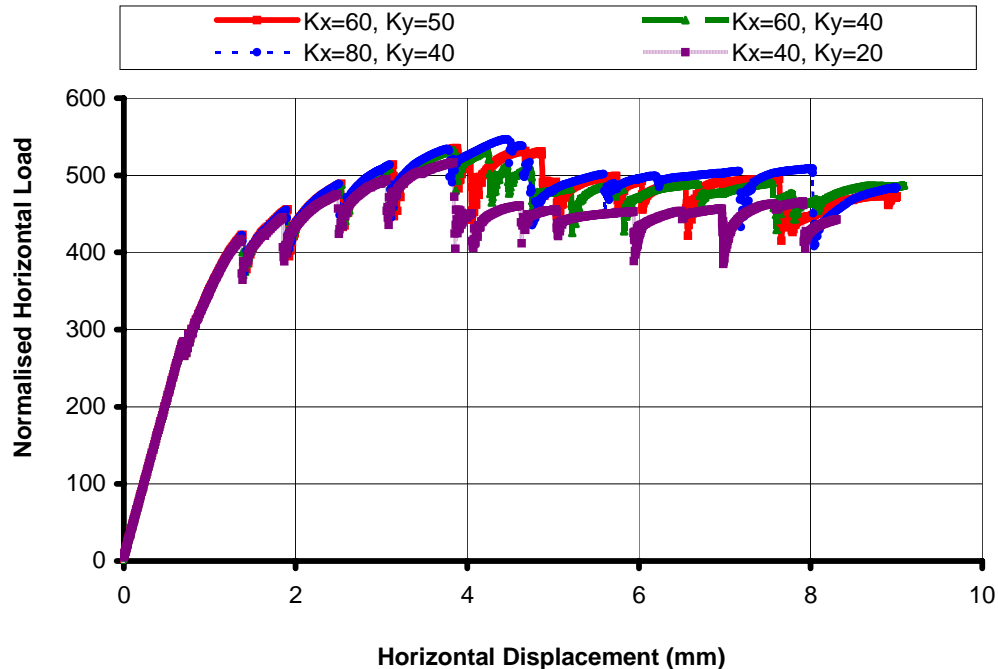


Figure 6.19: Effect of characteristic length factors on load-displacement response

It can be seen from Fig. 6.19 that all the three sets of characteristic length factors produced similar results. However, $k_x = 60$, and $k_y = 50$ produced load-displacement behaviour closer to the experimental curves, therefore they were used for analyses of other walls.

6.7.4.2 Stress – Strain State

ABAQUS explicit solution produces engineering as well as logarithmic strains. Logarithmic strains are calculated from Eq. 6.29.

$$\varepsilon_{\log} = \int \frac{dl}{l} = \ln\left(\frac{l}{l_0}\right) \quad (6.29)$$

where ' l ' is the change in length of the element and ' l_0 ' is the original length of the element. Logarithmic strain was found useful in understanding the behaviour of the WSRM wall because the wall cracked substantially and the strain vectors then indirectly represented crack width in an approximate sense. State of stress at the end of vertical load application is shown in Fig. 6.20. The corresponding contour plot of the vertical stress is shown in Fig. 6.20(a).

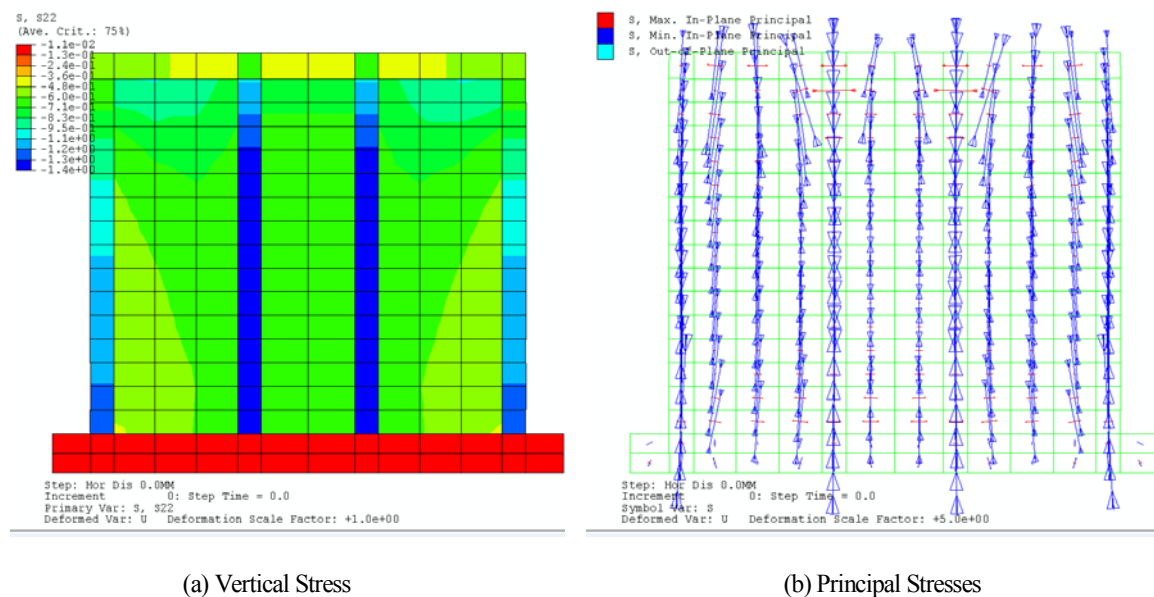


Figure 6.20: Stress state at application of full vertical load (0 Horizontal Load)

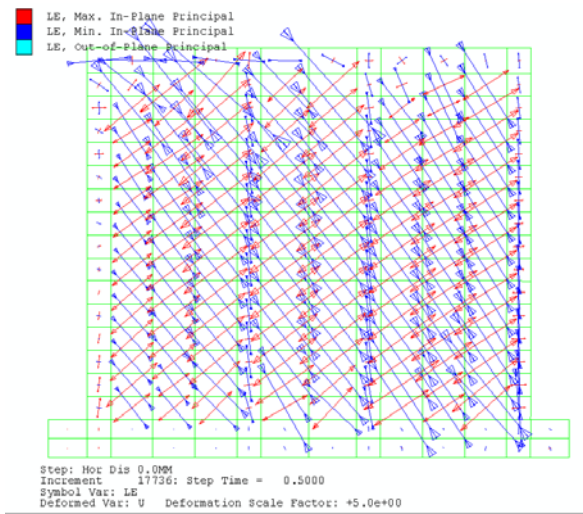
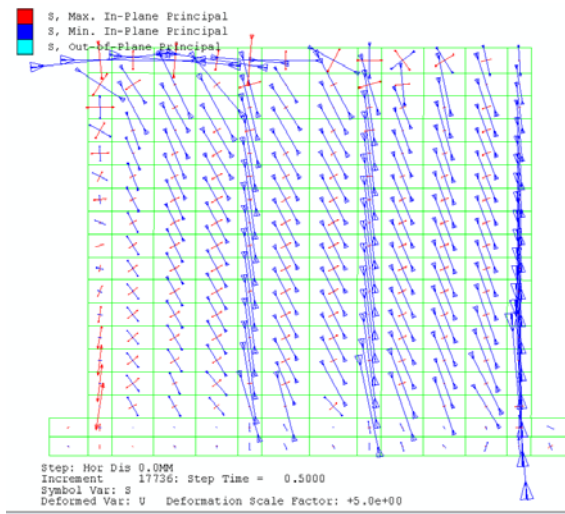
The magnitude of the vertical stress in the bond beam elements was equal to approximately 0.5MPa, which assured the right amount of vertical load on the wall. The thickness of the grouted cores was equal to 150mm. Stress in the URM was high due to reduced thickness of masonry (70mm for face shell bedding). Stress in the base slab was low due to its large thickness (1000mm).

Directions of principal stresses (tension and compression) are shown in Fig. 6.20(b). In the grouted cores where the magnitude of the vertical stress was high, principal compressive stresses were truly vertical whereas in the URM strain vectors showed some inclination.

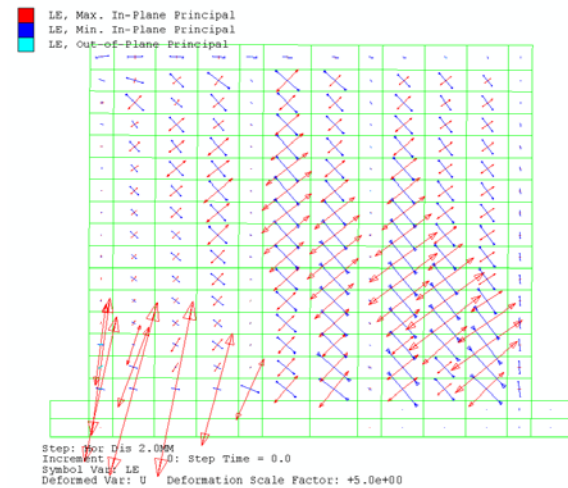
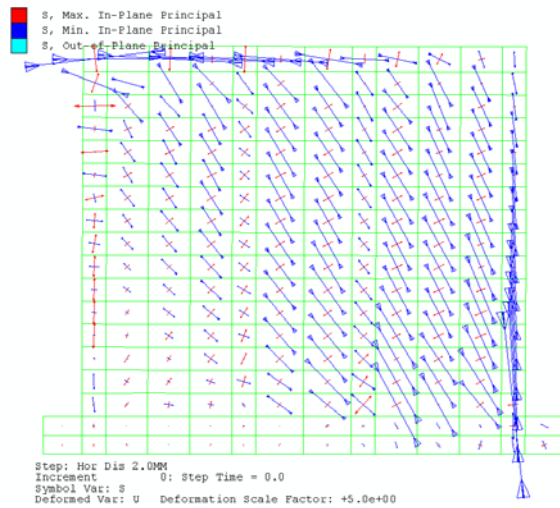
States of stress and logarithmic strain at various horizontal displacements for the WSRM wall are shown in Fig. 6.21.

Principal stresses and principal strains in the WSRM wall at 0.5mm of horizontal displacement are shown in Fig. 6.21(a). Principal stresses were fairly uniformly distributed in the body of the wall. Tensile and compressive stresses were observed in the left and the right vertical reinforced cores respectively.

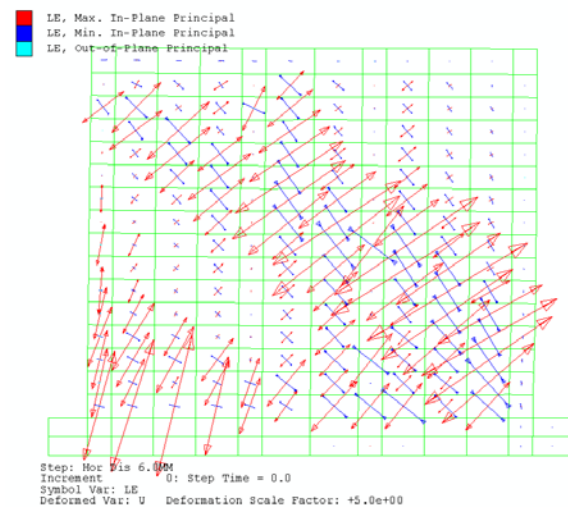
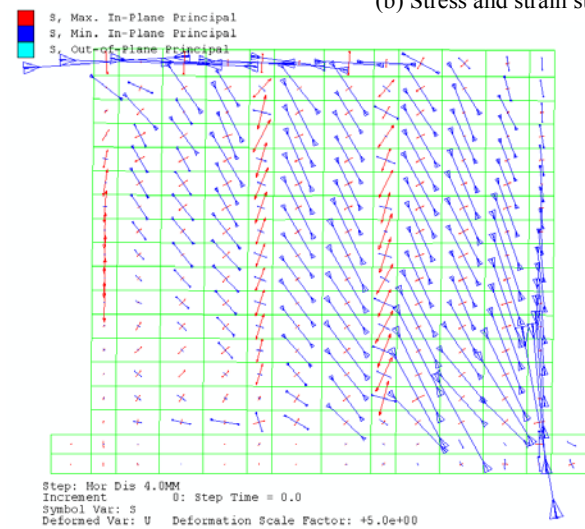
At 2mm horizontal displacement (see Fig. 6.21(b)), the magnitude of the principal stresses (compression and tension) increased along the diagonal of the wall and higher tensile strains were observed in the heel region of the wall. At this displacement, principal tensile and compressive stresses increased along the diagonal of the wall distinct from other regions of the wall. Principal tensile strains increased significantly along the diagonal establishing a potential path for the wall to crack. At 4mm horizontal displacement (see Fig. 6.21(c)), tensile strains and compressive strains propagated along the full length of the diagonal of the wall. Principal compressive stresses further increased whereas the principal tensile stresses marginally decreased and the principal tensile strains substantially increased. Decrease in the tensile stress indicated occurrence of cracking along the diagonal.



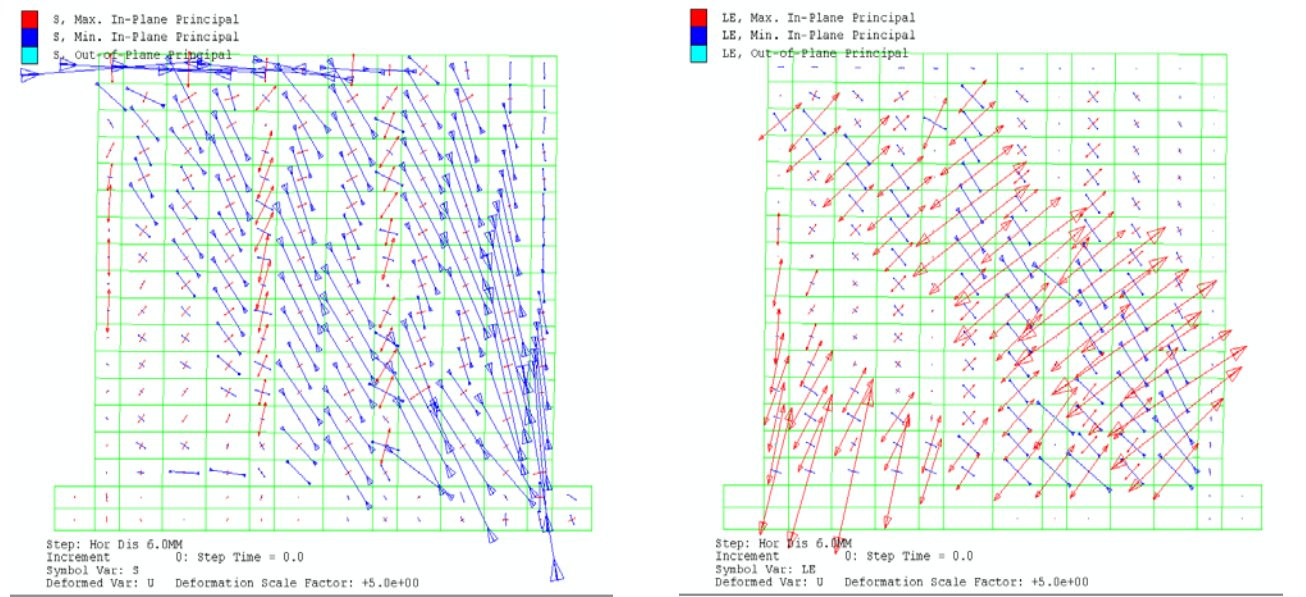
(a) Stress and strain state at 0.5mm of horizontal displacement



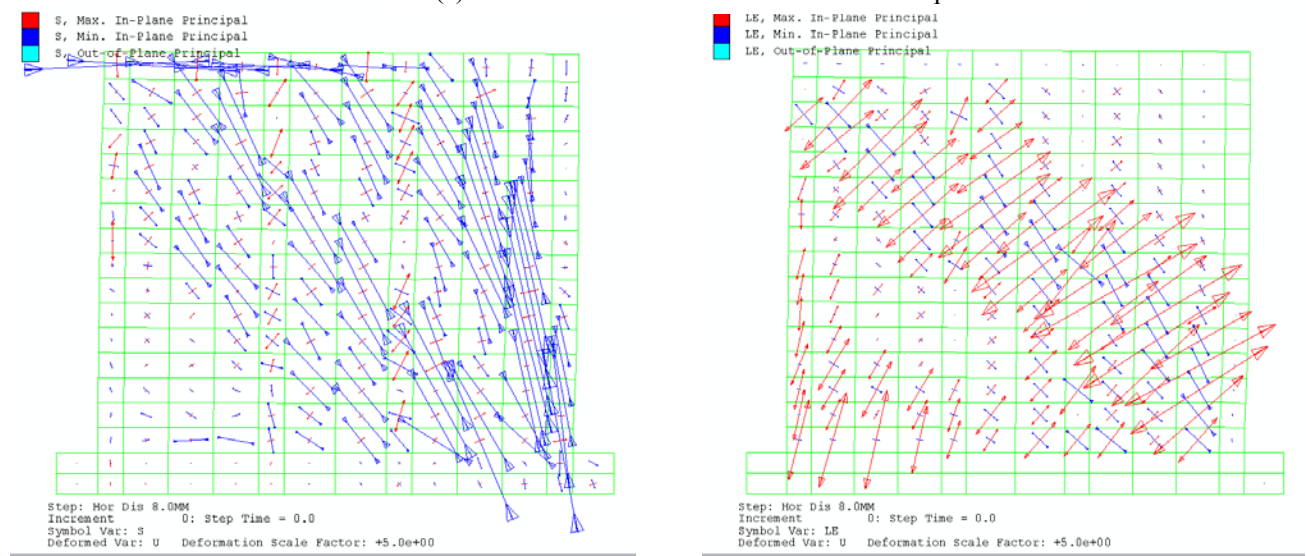
(b) Stress and strain state at 2mm of horizontal displacement



(c) Stress and strain state at 4mm of horizontal displacement



(d) Stress and strain state at 6mm of horizontal displacement



(e) Stress and strain state at 8mm of horizontal displacement

Figure 6.21: Stress and Strain states of WSRM wall

At 6mm horizontal displacement, principal tensile stresses along the diagonal significantly reduced whereas principal compressive stresses and the tensile strains further increased. It can be seen from Fig. 6.21(d) that at 6mm of horizontal displacement, the FE model has predicted a diagonal crack.

At 8mm of horizontal displacement, decrease in the principal tensile stress spread to a large area along the diagonal and the principal compressive stresses and principal tensile strains increased substantially indicating widening of the diagonal crack. By comparing Fig. 6.21(e) with Fig. 4.17, one can conclude that the FE model developed in this thesis has the capability of predicting the cracks that cause failure of the WSRM walls. Both these figures depict the failure mode of the WSRM walls at the ultimate load stage. Fig. 6.21(e) is the prediction by the FE model and Fig. 4.17 is the failure mode of the WSRM wall captured from the experiments.

6.8 Non-WSRM Wall Modelling, Analysis and Results

As the URM wall was geometrically similar to the WSRM wall with the exception of having no vertical reinforced cores, it was considered for modelling. The material model explained in section 6.3 was used for URM. A medium density mesh shown in Fig. 6.22 was generated for the analysis of the URM wall.

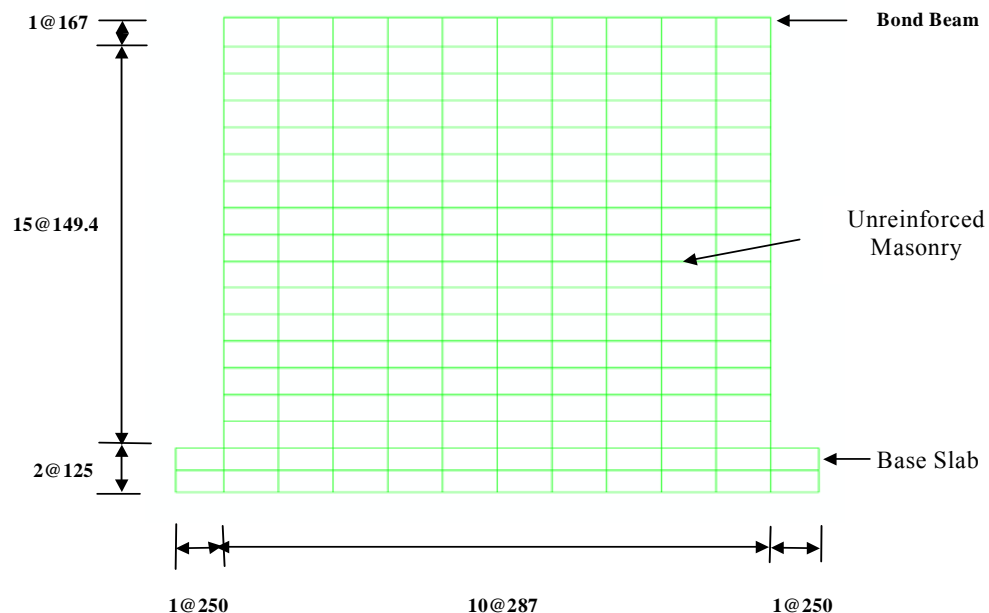


Figure 6.22: Mesh for the analysis of URM wall

Using the mesh shown in Fig. 6.22, frequency analysis was performed. The first mode of vibration of the URM wall is shown in Fig. 6.23. The natural frequency of the URM wall was found to be equal to 101.78Hz (natural frequency of the WSRM wall was equal to 111.20Hz). The natural time period for the URM wall was approximately equal to 0.01sec.

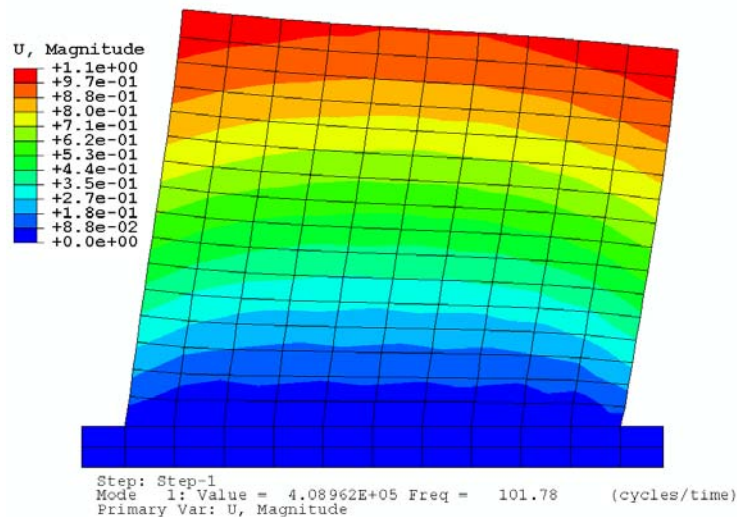


Figure 6.23: First mode of vibration of the URM wall

6.8.1 Analysis of URM Wall

Similar to the WSRM wall, the natural time period of the URM wall was factored by 10 for the application of the vertical load and by a factor of 100 for the horizontal displacement application. Material data used for the analysis of the URM wall were kept the same as that for the URM panels of the WSRM wall. Characteristic length factors (k_x and k_y) were also kept the same (60, 50). The procedure adopted for the application of the vertical load and the horizontal displacement for the analysis of the WSRM wall was followed for the analysis of the URM wall.

The quality of analysis was inferred through monitoring of energy from the energy plot shown in Fig. 6.24.

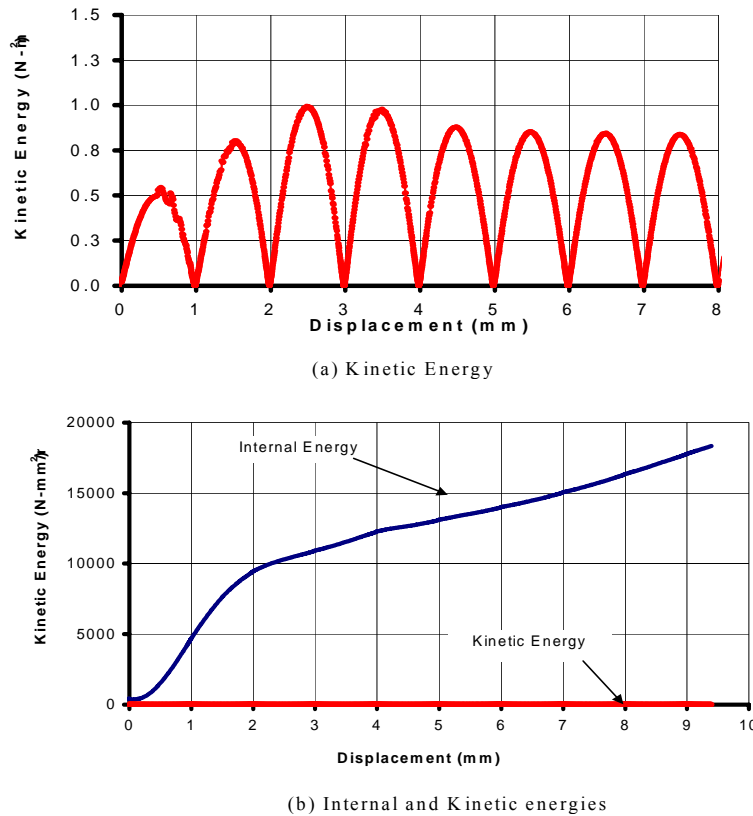


Figure 6.24: Energy balance for analysis of URM wall

It can be found from Fig. 6.24(a) that the kinetic energy remained smooth during the whole analysis. Internal and kinetic energies dissipated during the analysis are shown in Fig 6.24(b) indicating a measure of successful minimisation of the effects of inertia. The other criterion of energy balance shown in Eq. 6.26 was also met. As both energy criteria are satisfied, it is inferred that the increase in the time period was adequate for obtaining stable solutions.

6.8.2 Analysis of Results and Discussions

The load-displacement response and stress strain states at various stages of application of the horizontal displacement obtained for the URM wall are presented in this section.

6.8.2.1 Stress and Strain States

State of stress at the end of the vertical load application is shown in Fig. 6.25.

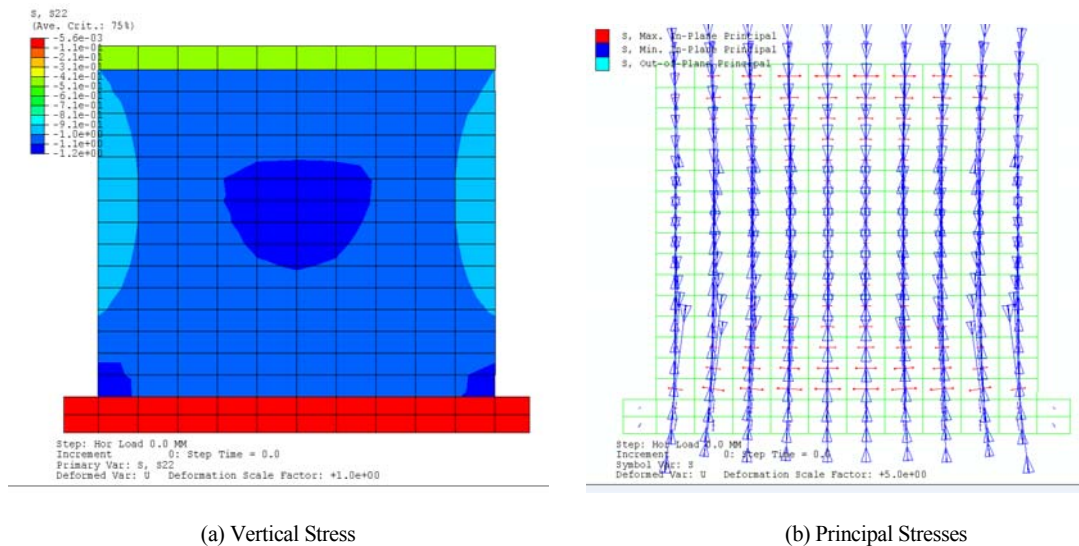


Figure 6.25: State of stress for URM wall at 0 horizontal displacement

The corresponding contour plot of the vertical stress is shown in Fig. 6.25(a) and directions of principal stresses are shown in Fig. 6.25(b). Minimum principal stress (compressive) was generally vertical showing the true flow of the vertical load. Maximum principal stress (tensile or relatively low magnitude compressive) was also found at the top and bottom of the wall exhibiting arching action. Distribution of the stress in the whole body of the wall was generally uniform.

States of stress and logarithmic strain at various horizontal displacements for the URM wall are shown in Fig. 6.26. Principal stresses and principal strains in the URM wall at 1mm of horizontal displacement are shown in Fig. 6.26(a). The magnitude of principal compressive stresses and principal tensile stresses was higher along the diagonal of the wall as compared to the other regions. Principal strains were also found to be higher along the diagonal. Large principal tensile

strains were found at the heel region, which decreased approximately linearly towards the toe region. This shows that the model was capable of predicting potential rocking failure of the URM wall, especially under low vertical loading.

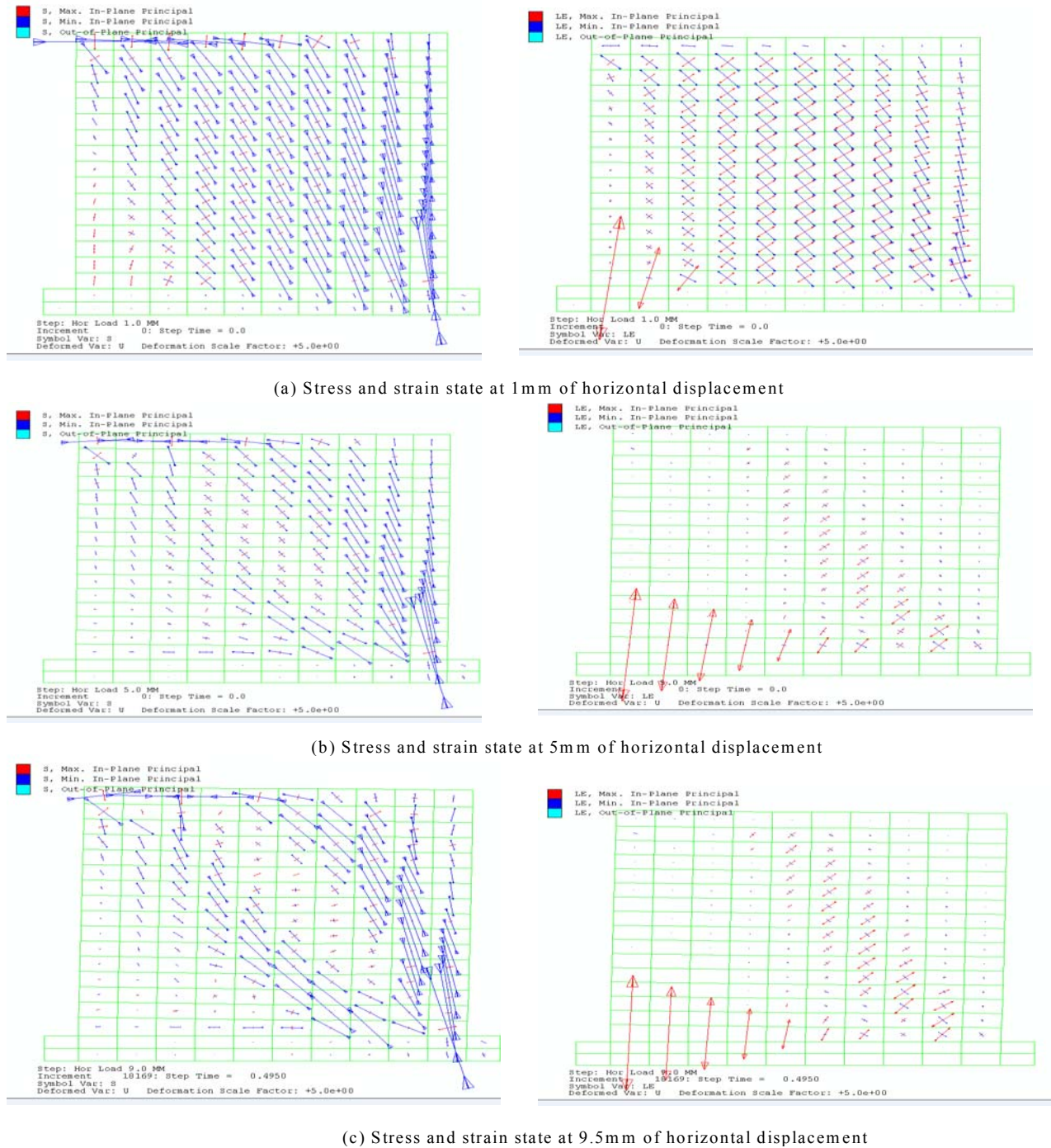


Figure 6.26: State of stress and strain of URM wall at various loading stages

Fig. 6.26(b) presents the states of stress and strain at 5mm of horizontal displacement. The principal tensile stresses substantially reduced at this displacement along the diagonal and at the heel, whereas the tensile strains increased in the corresponding regions. This phenomenon is due to crack opening at some salient locations. Fig. 6.26(c) shows further reduction in the principal stress and relatively large strains along the diagonal. This is exhibiting widening of the crack width along the diagonal. Fig. 6.26(c) compares well with Fig. 4.23 that depicts the crack pattern of the URM walls obtained from the experiment.

6.8.2.2 Load-displacement Response

The load-displacement response of the URM wall determined using the explicit formulation is presented in Fig. 6.27 along with the experimental load-displacement curves of all non-WSRM walls.

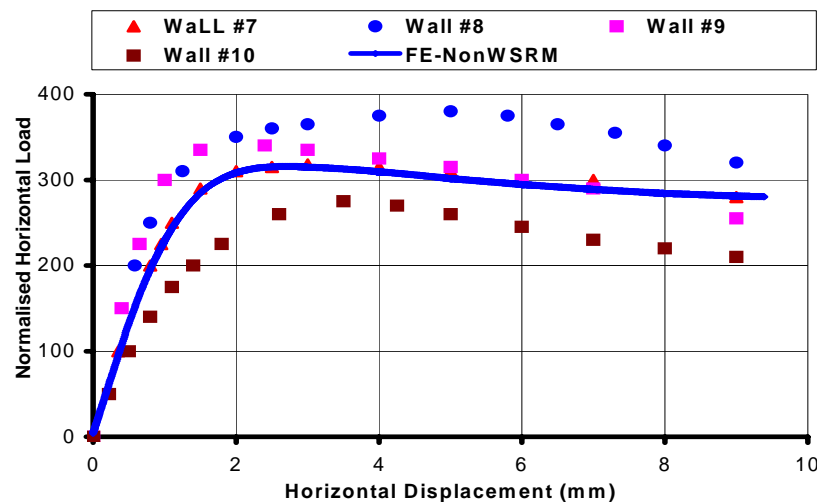


Figure 6.27: Load-displacement response of Non-WSRM walls

Fig. 6.27 shows that the FE model could predict the peak load and hardening and softening regimes of the load-displacement curves reasonably well. The smooth FE curve in Fig. 6.27 explains the absence of spikes in kinetic energy (see Fig. 6.24).

From the comparison, it could be concluded that the explicit FE model (together with the material parameters listed in Table 6.2) is capable of predicting the behaviour of WSRM and Non-WSRM (in particular URM) walls. As the model and the corresponding material dataset have only been validated using walls of one aspect ratio subjected to a vertical compression of 0.5MPa, the robustness of the model in predicting the behaviour of walls of all kinds can not be claimed. More validation experimental program is reported in Chapter 7.

6.9 Effect of Vertical Reinforced Cores

This section provides some additional insight into the results obtained from the analysis of the WSRM and Non-WSRM walls carried out in this chapter.

6.9.1 Load-Displacement Response

Load-displacement curves of the WSRM and Non-WSRM walls determined through the FE model are presented in Fig. 6.28.

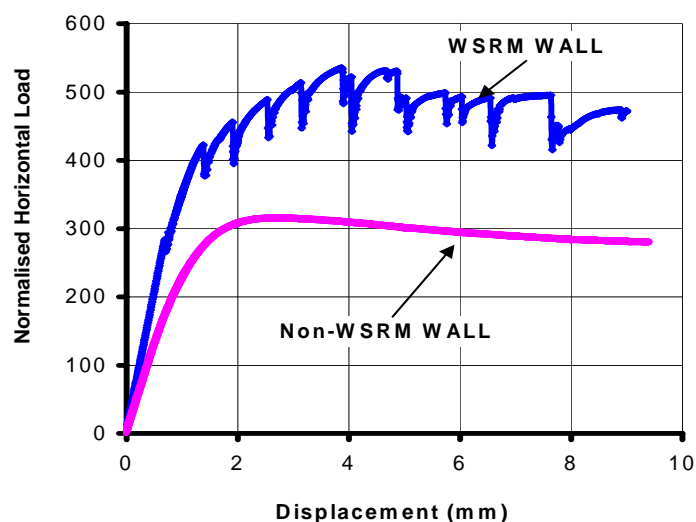


Figure 6.28: FE predicted load –displacement response of WSRM and Non-WSRM walls

It is evident from Fig. 6.28 that the presence of vertical reinforced cores has significantly increased the in-plane load capacity of the shear walls. Shear capacity of the WSRM wall was higher than that for the Non-WSRM wall. Based on this behaviour one could infer that the presence of vertical reinforced cores appears to be more effective in improving the shear capacity, but the softening characteristics are not largely affected.

6.9.2 Stress Variation in Critical Zones

Stress and strain data for the critical zones of the masonry walls (WSRM and Non-WSRM) were extracted from results obtained from FE analyses and are reviewed in this section. Three critical zones of the masonry walls, namely the centre, the heel and the toe as shown in Fig. 6.29 were considered for the discussion of stress variation.

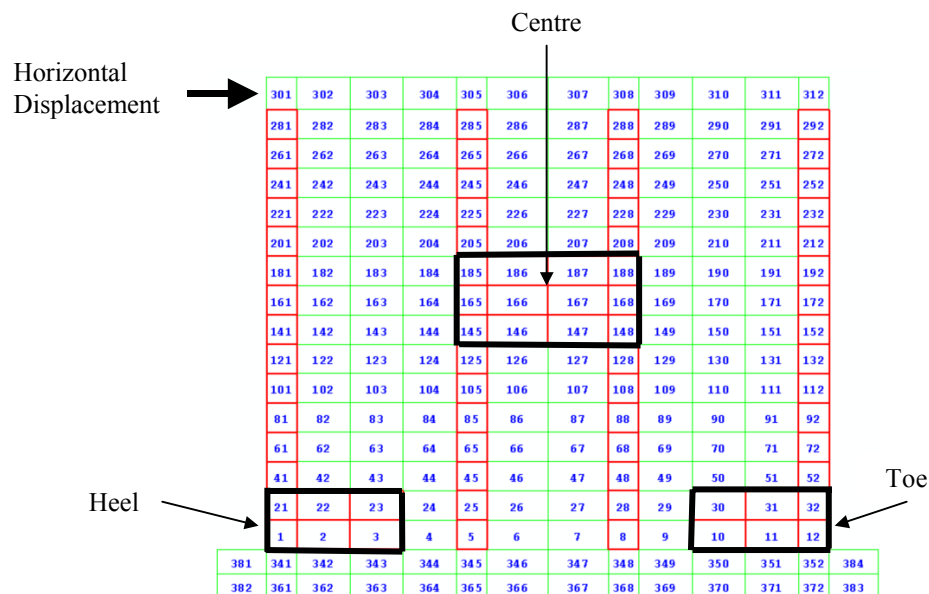
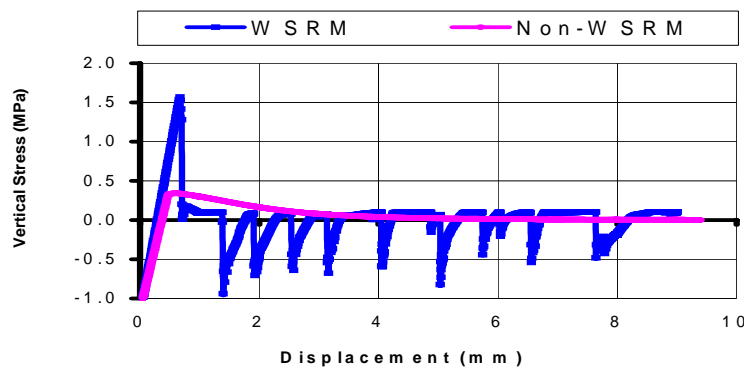


Figure 6.29: Critical zones of wall for stress and strain study

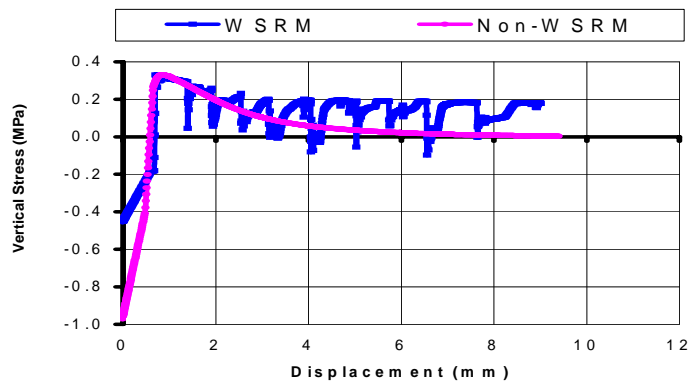
Elements #1 and #2 for the grouted section and the ungrouted section respectively were selected for the heel region. Similarly elements #11 and #12 for the toe region and elements #167, #168 for the centre region were selected. Element numbering for the Non-WSRM wall was different to

that for the WSRM wall due to mesh variation caused by the different locations of the vertical grouted cores, however, elements for the Non-WSRM wall were so selected that they lay in the same region as for the WSRM wall.

Vertical stress (S22) variation at the heel region is plotted in Fig. 6.30. Variation of stress in the grouted element and the ungrouted element at the heel region is presented in Fig. 6.30(a) and Fig. 6.30(b) respectively.



(a) Element # 1



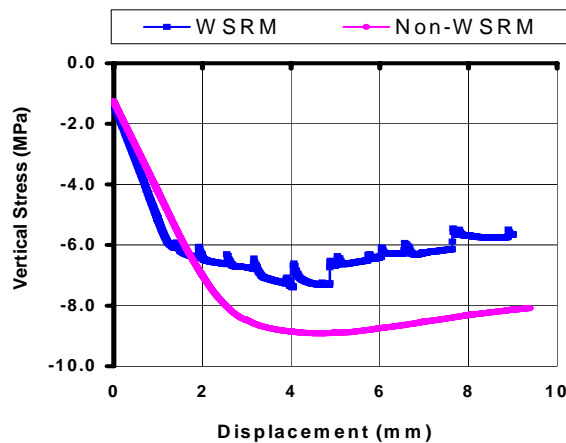
(b) Element # 2

Figure 6.30: Vertical stress (S22) variation at heel region of masonry walls

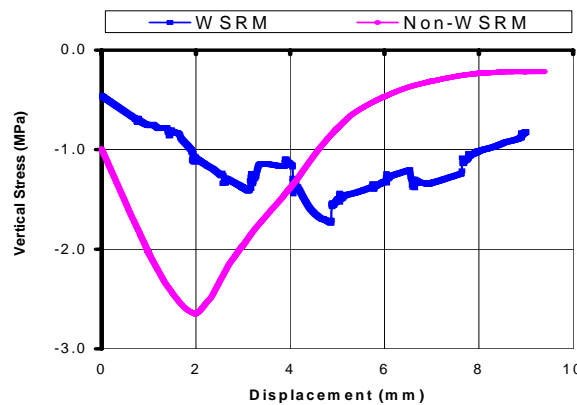
Fig. 6.30(a) shows that the grouted element (#1) of the WSRM wall exhibited a maximum 1.6MPa of tensile strength (its specified value) whereas the corresponding element for the Non-WSRM (URM) wall (ungrouted) exhibited its specified tensile strength of 0.35MPa. At 1mm to

2mm of horizontal displacement, both types of walls lost almost all of their tensile strength. The ungrouted element (element 2, Fig. 6.30(b)) of both the WSRM and the Non-WSRM walls at the heel region exhibited maximum tensile strength of 0.35MPa at approximately 1.2mm of horizontal displacement (see Fig. 6.30(b)); however, the WSRM walls retained significant tensile stress (0.2MPa) throughout the analysis. This shows that the presence of steel in the grouted core (in element #1) has contributed to the reduction in tensile strain (crack width) in the vertical direction that helped in retaining the tensile stress at 0.20MPa in the WSRM walls (see also Fig. 6.3). The URM walls did not have such a benefit from element #1.

Vertical stress (S22) variation of the grouted and the ungrouted elements at the toe region is plotted in Fig. 6.31(a) and Fig. 6.31(b) respectively.



(a) Element #12

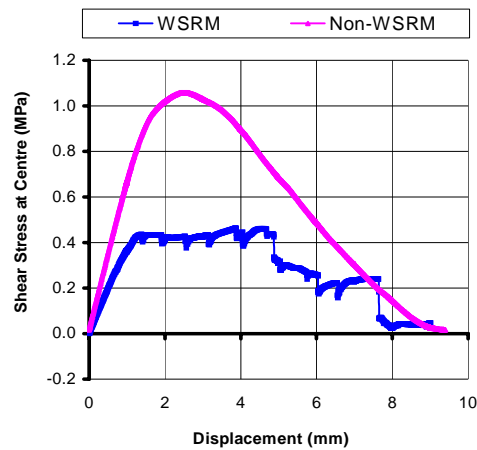


(b) Element #11

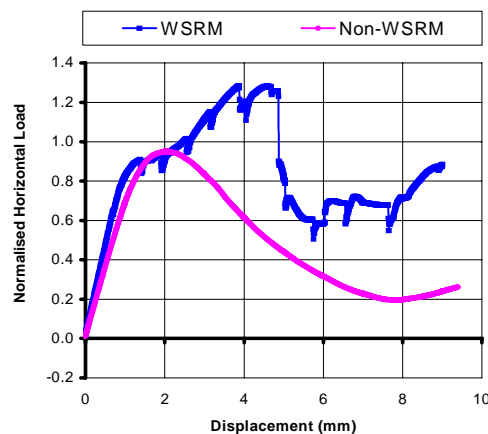
Figure 6.31: Vertical stress (S22) variation at toe region of masonry walls

From Figs. 6.31(a) and (b), it is evident that the vertical compressive stress (S22) in both the grouted and ungrouted elements for the Non-WSRM wall was higher than that for the WSRM wall in the corresponding elements. The grouted section of the toe of both the WSRM and Non-WSRM walls exhibited higher vertical compressive stress (7MPa to 9MPa) than that for the ungrouted section (1.7MPa to 2.7MPa).

Shear stress (S12) variation of the grouted and the ungrouted elements at the centre region is plotted in Fig. 6.32(a) and Fig. 6.32(b) respectively.



(a) Element #168



(b) Element #167

Figure 6.32: Shear stress (S12) variation at centre region of masonry walls

From Fig. 6.32(a), it is clear that the stress in element #168 of the Non-WSRM wall was much higher (approximately 1MPa) than that for the WSRM wall (approximately 0.4MPa). This was due to the presence of the grout, which provided increased thickness of the composite section of the hollow masonry unit, and grout in the WSRM wall hence resulted in lesser stress. A similar effect was indicated by the elastic analysis of the walls (see Chapter 3 Fig. 3.9). Shear stress in element #167 of the WSRM wall was higher (1.3MPa) than that for the Non-WSRM wall (0.9MPa). These results show that the magnitude of the shear stress in the hollow masonry elements significantly reduces when the hollow masonry elements have increased resultant thickness due to presence of grout.

6.10 Summary

In this chapter, the theory of macro modelling, the material model for macro modelling of masonry, the formulations of explicit analysis, the frequency analysis of structures and the material models for grouted cores and reinforcement bars have been reviewed. Steps involved in the pre-processing, processing and post-processing for achieving stable static solutions using the dynamic formulations have been discussed. Different meshing schemes for the WSRM walls have been studied. Modelling of both the WSRM and Non-WSRM walls has been discussed.

The Explicit FE model has successfully predicted the behaviour of the WSRM and the Non-WSRM walls. Load flow throughout the body of the walls, and the states of stress and strain at different stages of the analysis have been very well exhibited by the FE model. The model has very well captured the modes of failure of both types of walls. Hardening as well as softening regimes of load-displacement curves have been found to be in good agreement, on average, with those obtained through experiments. Prediction of the softening part of the load-displacement curve has made it possible to calculate the ductility factor as well as the structural response factor used by the designers of masonry structures. The displacement ductility factor and the

corresponding structural response factor for the WSRM walls calculated from the load-displacement curve obtained from the FE model wall were 6.0 and 3.3 respectively.

Local reduction in the shear stress in the grouted elements and global increase in the ungrouted elements due to vertical grouted cores indicated by elastic analysis (Chapter 3) has been exhibited by the nonlinear analysis described in this chapter.

Although this model has successfully predicted all characteristics of the masonry walls, still the characteristic length of elements in the URM panels required adjustment for calculation of fracture energy. A similar discrepancy in the calculation of fracture energies violating the rules of Eq. 6.7 and 6.12 has also been found for the masonry walls included in Lourenco (1996) where the formulation was of the implicit type. Based on these studies, it is strongly recommended that a comprehensive research program on the fracture energy, strain localisation and characteristic length of the URM be conducted.

CHAPTER 7

VALIDATION OF THE FINITE ELEMENT MODEL

7.1 Introduction

To validate the finite element model developed in Chapter 6, four WSRM walls were constructed and tested. These walls were of two aspect ratios (0.50 and 1.11). Two of these walls were tested under vertical compression of 0.25MPa; one under 0.04 MPa and one without any vertical load (zero pre-compression). Design, construction, curing, handling and testing procedures adopted for the first phase of experiments (wall #1 to #10, Chapter 4) were followed for these four walls. Modes of failure, load-deformation response and shear capacity of the validation test walls obtained from the FE model are compared with that obtained from these experiments. Shear capacity of the validation test walls predicted by AS3700 (2001) and by the FE model are also compared with that obtained from the experiments. It has been shown that the results obtained from the FE model are in good agreement with those of the experiments. Effects of the aspect ratio and the vertical stress to the behaviour of the WSRM walls are also discussed in this chapter.

7.2 Design of Validation Tests

It was intended to validate the FE model presented in Chapter 6 with the WSRM walls of different aspect ratio subjected to different vertical compression. The validation test walls were so designed that they required minimal modifications to the test rig to minimise the cost and time. For the purpose, the length of two of the four walls was chosen exactly the same as that of the previous walls (2870mm). The other two walls had reduced length (1270mm). The height of

all the four walls was kept the same which resulted in two aspect ratios (0.50, 1.11). Table 7.1 shows the geometric details and the parameters of testing of the validation test walls.

Table 7.1: Design details of validation test walls

Wall No.	Group	Size of Walls	Aspect Ratio	Vertical compression (MPa)	Panel Width of URM (mm)	
					Middle	Ends
#11	#7	2870×1411×150	0.50	0.25	780	960
#12				0.04	780	960
#13	#8	1270×1411×150	1.11	0.25	1100	-
#14				0.00	1100	-

All four walls were constructed from commercially available hollow clay blocks of gross dimensions 310mm × 150mm × 73mm with two symmetrical voids of size 100mm × 80mm × 73mm at the centre to accommodate grouting and steel bars. The height of the clay blocks was 3mm shorter than that of the blocks used in first phase of experiments.

Walls of Group #7 had four grouted cores whereas the walls of Group #8 had two grouted cores as shown in Fig. 7.1. Walls of Group #7 had 9 blocks along the length and 17 blocks along the height. Walls of Group #8 had 4 blocks along the length and 17 blocks along the height.

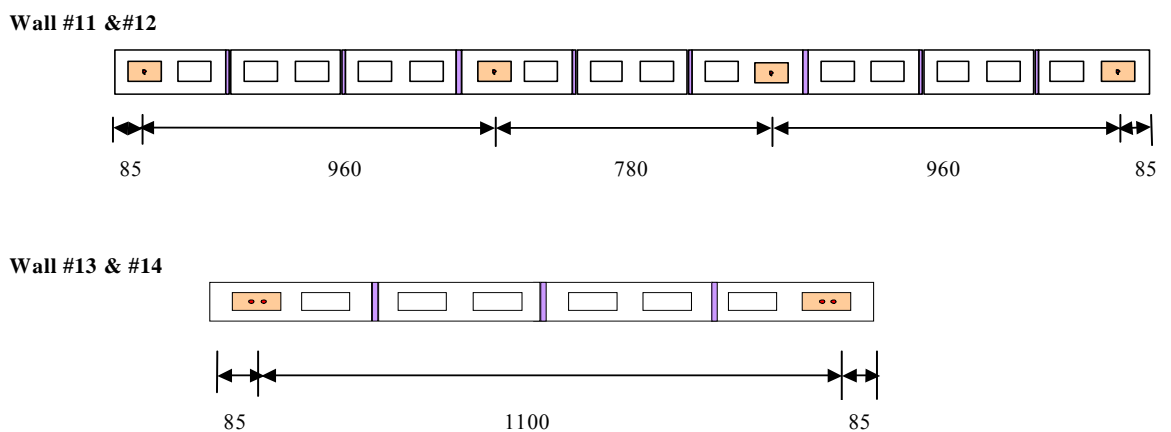


Figure 7.1: Design of validation test walls

The gross area of the walls of Group #7 determined as the product of the thickness of the wall (150mm) and the length of the wall (2870mm) was equal to $430,500\text{mm}^2$, whereas the design area determined as the bedded area ($70\text{mm} \times 2870\text{mm}$) of the ungrouted masonry plus the area of the grouted cores ($4\text{mm} \times 100\text{mm} \times 80\text{mm}$) was equal to $232,900\text{mm}^2$. The gross area of the walls of Group #8 was equal to $190,500\text{mm}^2$, whereas the design area was equal to $104,900\text{mm}^2$.

Walls of both the groups contained 4N12 reinforcement bars. In the walls of Group #7, one bar was placed in each grouted core (total 4 grouted cores) whereas in walls of Group #8, two bars were placed in each grouted core (total 2 grouted cores) to keep the area of reinforcement the same. The bond beam at the top of the walls contained 2N16 reinforcing bars.

The ratio of the vertical reinforcement in the walls of Group #7 based on the gross area and the design area was equal to 0.10% and 0.19% respectively, whereas these ratios for the walls of Group #8 were equal to 0.23% and 0.42% respectively. Horizontal spacing between the vertical grouted reinforced cores was within the limits specified in AS3700 (2001).

7.3 Construction and Testing of Walls

The base slabs used for the construction of the walls of the first phase of experiments (Wall #1 to #10) shown in Fig. 4.2 were reused for the construction of the validation test walls. The previously tested walls were dismantled and the top surface of the slab was first cleaned. Locations of the reinforcement bars for the validation tests were marked on the slab and holes were drilled to three quarters of the depth of the slab (approximately 180mm) and the reinforcement bars were inserted into the drilled holes and filled with resin epoxy to achieve good bond between the reinforcement bars and the concrete slab. For quality assurance, pullout tests were performed on the bond between the reinforcement bars and the concrete slab.

A flat plate was welded to the top of the bar to provide a strong grip. The bar was pulled out under displacement control and the bond between the bar and the concrete slab was monitored. No significant slip was noticed until failure of the bar as shown in Fig. 7.2.



Figure 7.2: Bond test between the new steel bar and the old concrete slab

This experiment provided the evidence that the slabs that were originally constructed for the first phase of experiments were reusable hence it saved cost and time. All the validation walls (#11, #12, #13, #14) were constructed on top of the old slabs with new reinforcement bars.

Masonry was laid in face shell bedding using a mortar bed of 10-mm thickness. A bond beam equal to the length of each wall was constructed at the top to enable uniform distribution of the applied vertical load and to minimise the chances of local failure of the loaded corners of the walls under the application of the horizontal load. The hollow masonry cores that were intended for the vertical reinforcement were flushed out with water after the completion of construction of the masonry shells. The walls were grouted after seven days of construction. A smooth surface steel bar was used for tamping the wet grout in the vertical cores and a steel trowel was used for tamping the grout in the bond beam.

Construction, curing and handling processes explained in section 4.3 were followed for these experiments. The testing procedure and arrangement of boundary conditions were similar to those adopted for the first phase of experiments. The rolling assembly for free lateral drift of the walls and the push and pull assembly for the load application were also kept the same. Steps involved in the application of loading for these walls were similar to those for the first phase of experiments explained in section 4.4.4. The data acquisition system explained in section 4.4.5 was used for recording the load and deformation data of these test walls.

7.3.1 Constituent Materials

The type and quantity of vertical reinforcement, the type of masonry units, the mortar mix and grout mix which were used in the first phase of experiments were also used for the construction of the validation test walls. Samples of mortar, grout, and grouted and ungrouted masonry prisms for each validation test wall were collected at the time of construction and tested at the time of testing of the walls. Four samples for each constituent material were prepared and tested as per standard procedures (AS2701.4 (1984), AS4456.3 (2003), AS3700 (2001)). The average compressive strength of the test samples was calculated from Eq. 4.1 and the values are reported in Table 7.2.

Table 7.2: Compressive strength of constituent materials

Walls #11, #12, #13, #14	Mortar Cubes	Grout Cylinders	Grouted Masonry Prisms	Hollow Masonry Prisms
Average compressive strength (MPa)	6.8	28.2	20.3	20.4
Number of specimens	4	9	4	4
Standard Deviation (MPa)	1.6	5.1	5.1	3.1
C.O.V. (%)	24%	18%	25%	15%

The horizontal load determined from the experiments was normalised using the shear strength of masonry calculated from the compressive strength of masonry (20.3MPa) as shown in Eq. 4.2.

This compressive strength (20.3MPa) was also used for the FE model and in the normalisation process for the load-displacement curves obtained from the FE model.

Similar to the first phase of experiments, vertical loading was applied first where required and then the displacement controlled horizontal load was applied at a rate of 0.2mm/min until the onset of the yield load, and then at higher rate (0.6mm/min) until the peak load dropped by 20% (typical ultimate load stage).

The load-displacement response and the mode of failure (crack pattern) of the validation test walls (#11, #12, #13, #14) obtained from the FE model and from the experiments are presented in section 7.4.

7.4 Wall #11

Wall #11 was tested under a vertical compression of 0.25MPa. The aspect ratio of this wall was 0.50 in contrast to the 10 walls tested in the first phase of experiments (aspect ratio = 0.84) based on which the FE model was first developed. The load-displacement response and the crack pattern of wall #11 obtained from the FE model and from the experiments are presented in this section. The complete load-displacement curve obtained from the experiments is presented in Appendix C.

Similar to the first four groups (wall #1 to #8 shown in Fig. 4.1), this wall also contained four vertical reinforced grouted cores. A medium density mesh shown in Fig. 7.3 was generated for the analysis of this wall. This mesh is similar to the mesh shown in Fig. 6.14. The height of the elements in this mesh was slightly different due to the different height of this wall.

The FE model explained in Chapter 6 was used for the analysis of this wall. The process explained in section 6.6 was followed to obtain the stable solution. Energy plots of this wall are presented in Appendix E.

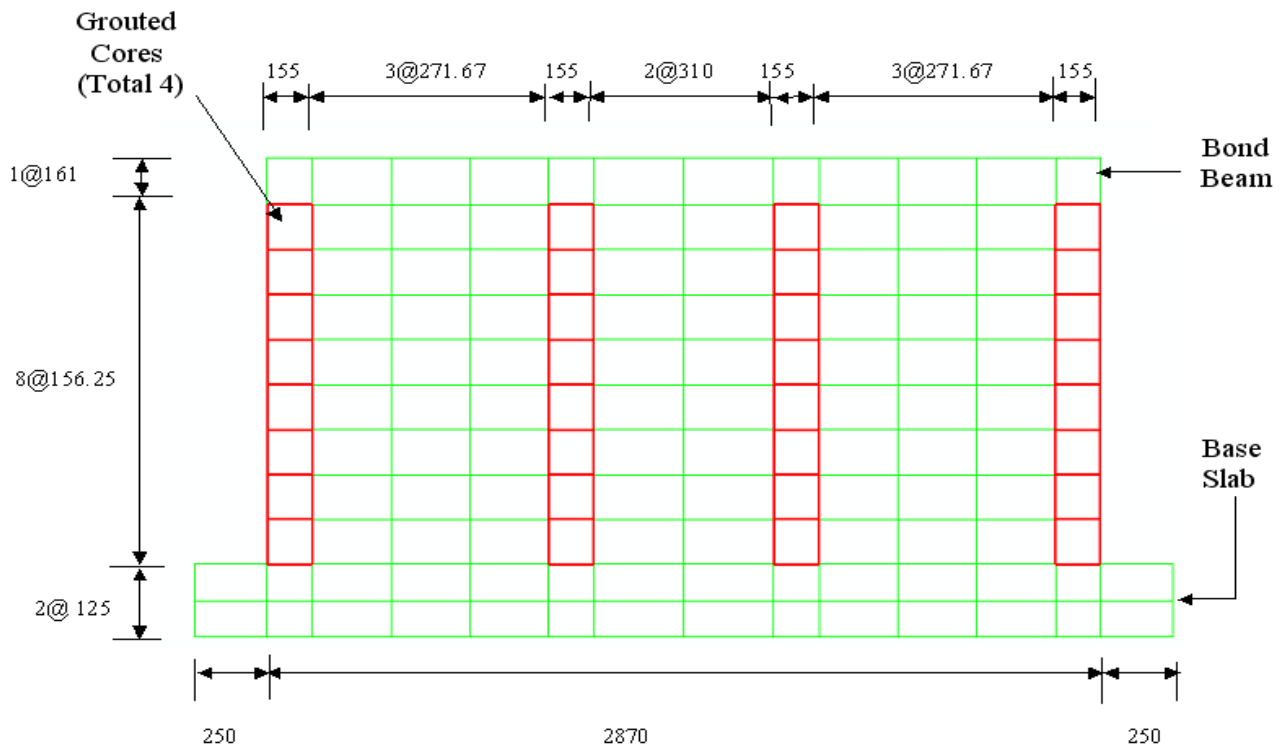


Figure 7.3: Mesh for wall #11 (valid for wall #12)

7.4.1 Mode of Failure

Logarithmic principal strains obtained from the FE model are presented in Fig. 7.4. These strains at approximate yield load stage (1mm horizontal displacement) and at the ultimate load stage (3.75mm horizontal displacement) are shown in Fig. 7.4(a) and (b) respectively.

At 1mm of horizontal displacement, logarithmic strains were distributed generally over the full length of the wall. The magnitude of these strains increased with the increase of the displacement controlled horizontal load until the wall failed. The higher magnitude of logarithmic strains along the diagonal shown in Fig. 7.4(b) exhibited the occurrence of a major crack.

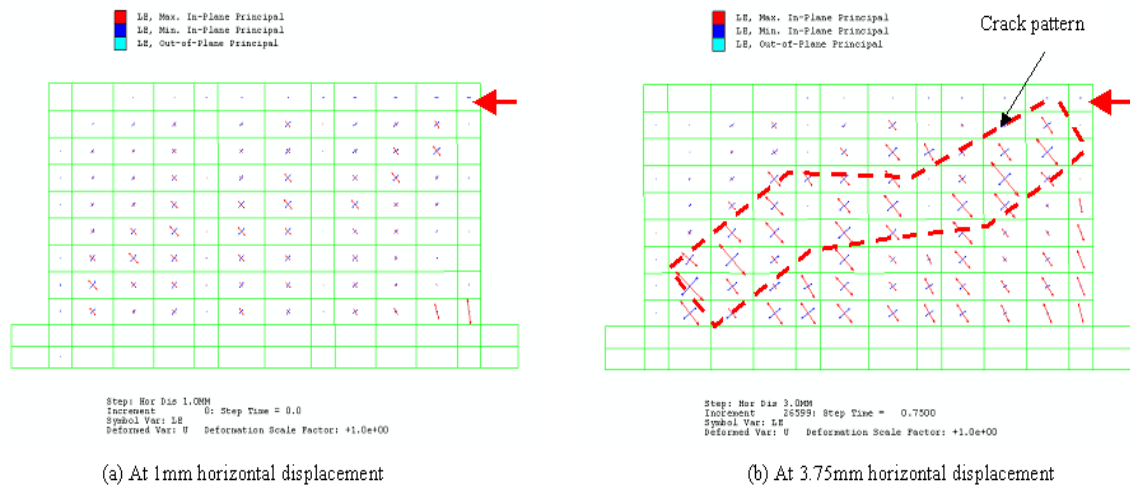


Figure 7.4: Principal logarithmic strains from FE model (wall #11)

Principal stresses obtained from the FE model at approximate yield and at ultimate load stages are shown in Fig. 7.5(a) and (b) respectively.

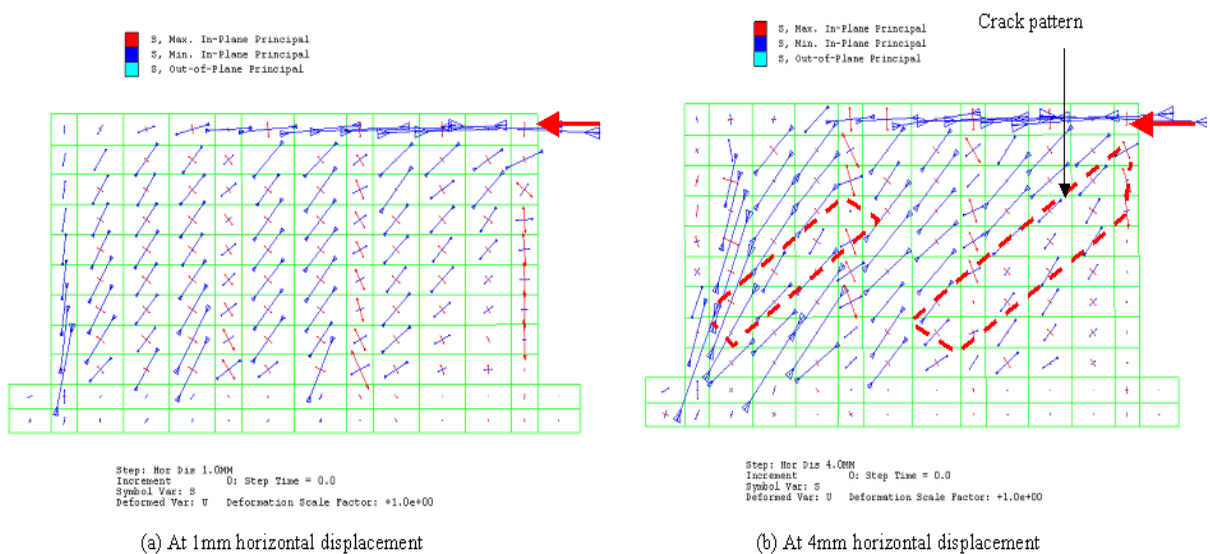


Figure 7.5: Principal stresses from FE model (wall #11)

At 1mm of horizontal displacement, principal stresses (maximum and minimum) were distributed over the full length of the wall, however the minimum principal stress (compressive) vectors showed inclination along the diagonal. With the increase in the horizontal displacement, the magnitude of the principal stresses significantly increased until, at about 3.75mm of

horizontal displacement, their magnitude significantly reduced at two locations as shown in Fig. 7.5(b). The locations where the principal stresses reduced (Fig. 7.5(b)) matched well with the locations where the logarithmic principal strains increased significantly (Fig. 7.4(b)).

Photographs of the wall taken during the experiment at approximate yield and at the ultimate load stages are presented in Fig. 7.6(a) and (b) respectively.

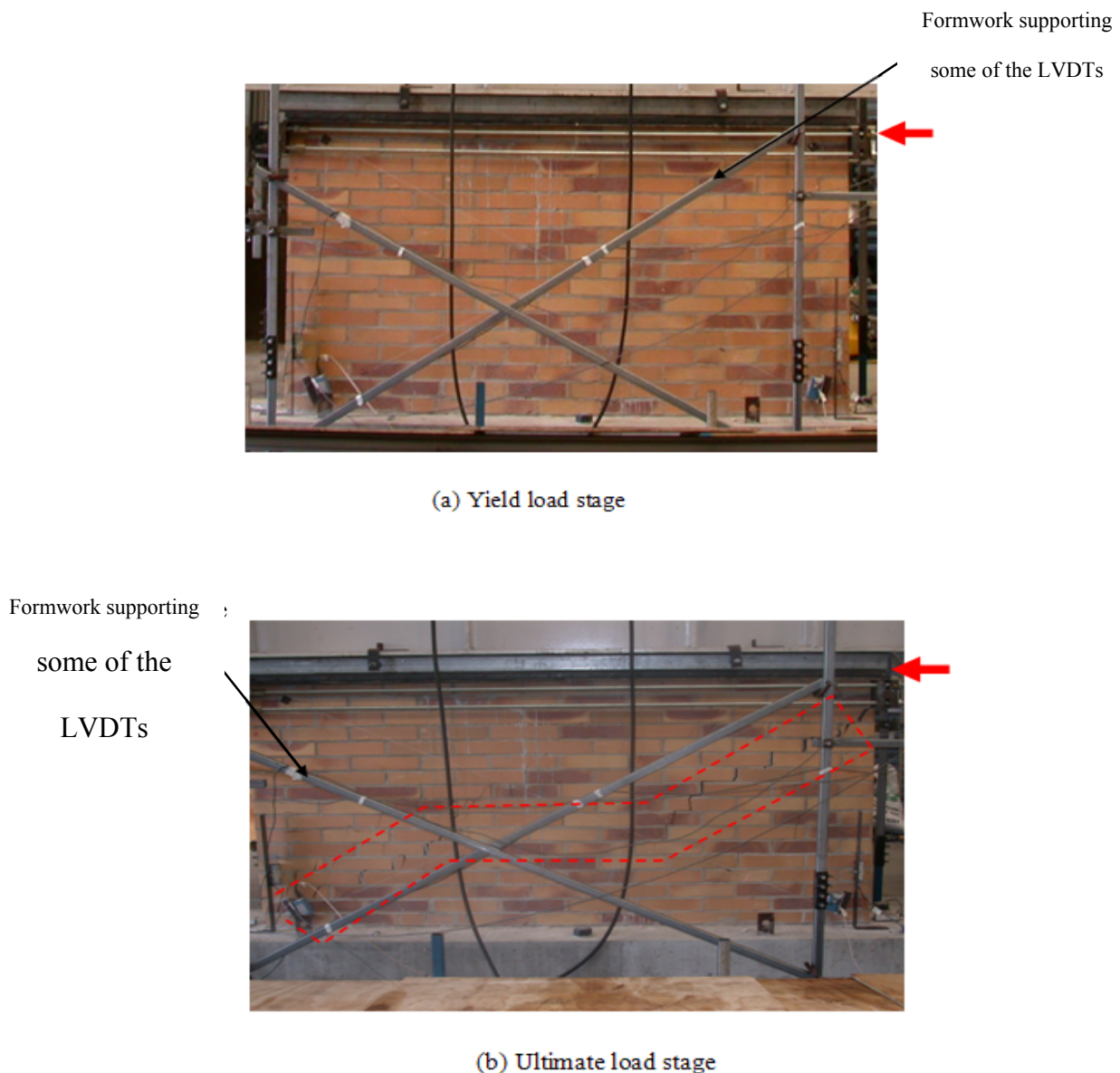


Figure 7.6: Crack pattern from experiment (wall #11)

No crack was observed at the yield load stage, however at the ultimate load stage the true crack pattern of the wall was observed. It can be seen from Fig. 7.6(b) that this wall did not exhibit a true diagonal crack rather the major crack emerged in step shape.

It is evident from Figs. 7.4(b), 7.5(b) and 7.6(b) that the crack pattern inferred from the FE model was in good agreement with that obtained from the experiment.

7.4.2 Load-Displacement Response

Normalised load-displacement curves of wall #11 obtained from the FE model and from the experiment are presented in Fig. 7.7. The elastic regime of the load-displacement curve obtained from the two methods showed good agreement.

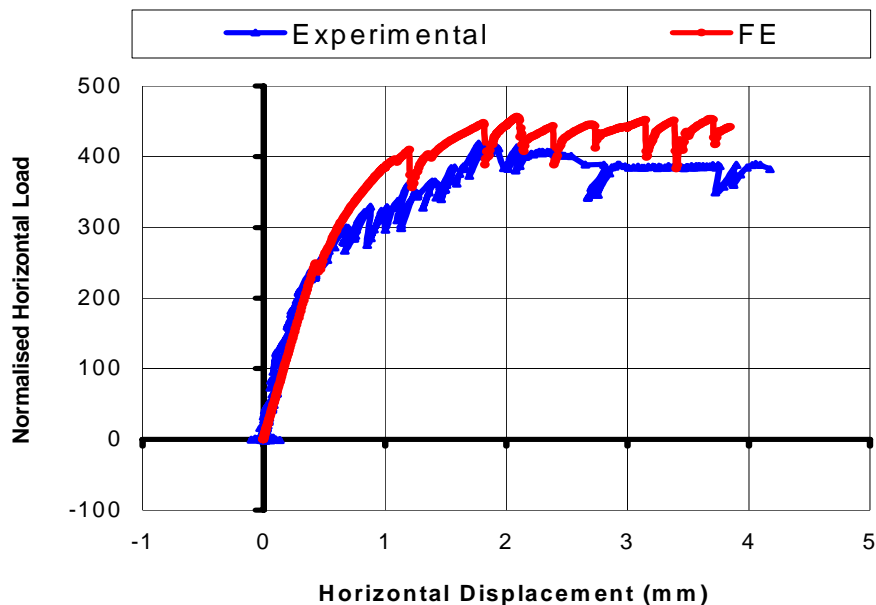


Figure 7.7: Load-displacement response of wall #11

Both the FE model and the experiment show that this wall reached the peak horizontal load at a horizontal displacement of approximately 2mm. Both the curves showed similar normalised peak horizontal load (“420” to “450” for the experiment and FE respectively).

The load-displacement curve obtained from the FE model could not show the 20% drop in the peak load due to numerical instability. A similar problem has been discussed earlier in section 6.3.1 of Chapter 6.

7.5 Wall #12

Wall #12 had similar geometry to that of wall #11 except this wall was tested under very small vertical load. Since this was the first wall to be tested under small vertical load or no vertical load, it was decided to keep at least one of the two spreader beams (each weighed 16kN) on the top just as a safety measure. Weight of the one spreader beam on the top of the wall resulted in 0.04MPa of vertical stress. A vertical stress of 0.04 MPa was also used in the vertical load step of the FE model to compare the results with that obtained from the experiments. The modes of failure and load-displacement response of wall #12 obtained from the experiments and from the FE model are presented in this section. The complete load-displacement curve of this wall is included in Appendix C. The mesh used for the analysis of wall #12 was similar to that used for wall #11 as shown in Fig. 7.3.

7.5.1 Mode of Failure

Logarithmic strains obtained from the FE model at approximate yield load stage (1mm horizontal displacement) and at the ultimate load stage (4.5mm horizontal displacement) for wall #12 are presented in Fig. 7.8(a) and (b) respectively.

Similar to wall #11, this wall also exhibited the highest magnitude of principal tensile strains along the diagonal region. Fig. 7.8(b) shows that the crack path did not align truly along the diagonal rather it was of step shape.

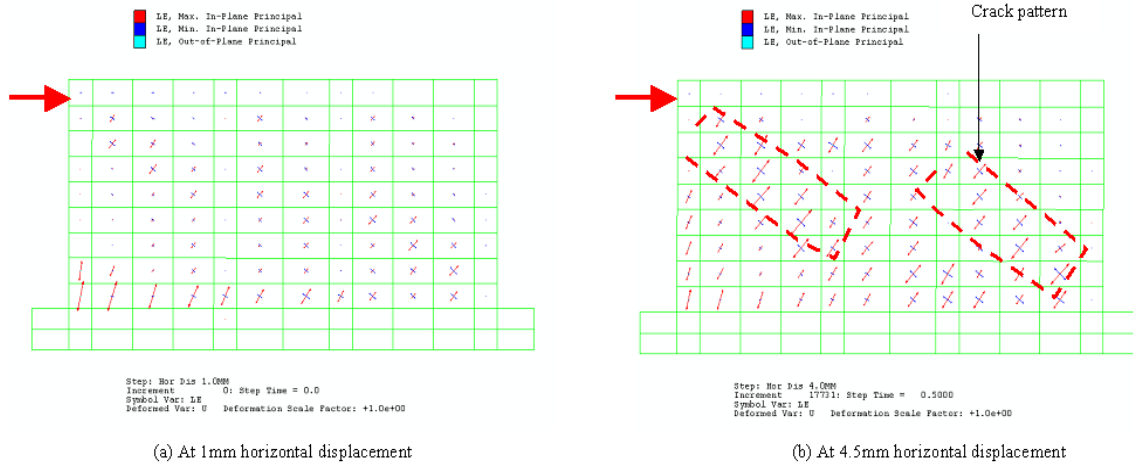


Figure 7.8: Principal logarithmic strains from FE model (wall #12)

Principal stresses obtained from the FE model at the approximate yield and the ultimate load stages are shown in Fig. 7.9(a) and (b) respectively.

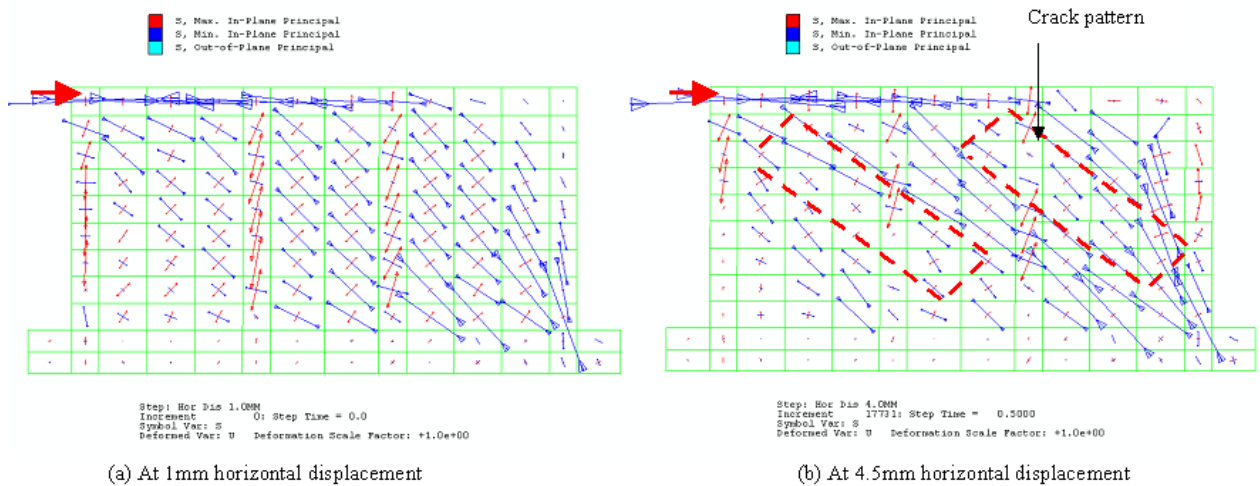


Figure 7.9: Principal stresses from FE model (wall #12)

It can be seen from Fig. 7.9 that the magnitude of the principal tensile stresses reduced drastically at two locations. These locations corresponded to the locations of higher magnitude principal logarithmic strains shown in Fig. 7.9(b). Photographs of the wall taken during the experiment at the approximate yield load and the ultimate load stages are presented in Fig. 7.10(a) and (b) respectively.

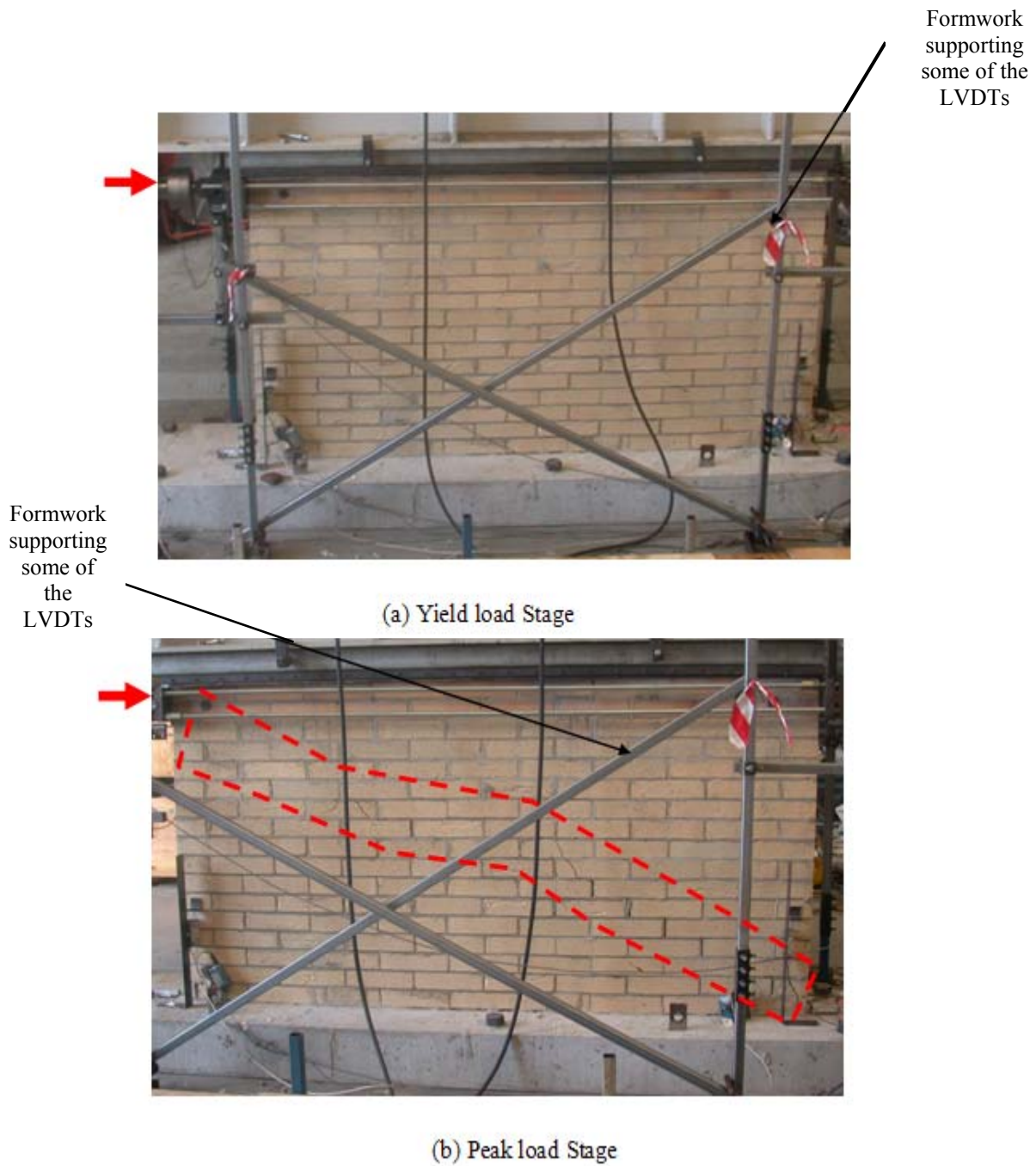


Figure 7.10: Crack pattern from experiment (wall #12)

From Figs. 7.8(b), 7.9(b) and 7.10(b) it is evident that the crack pattern inferred from the FE model matched well with that observed in the experiment. This, in conjunction with the outcomes presented in section 7.4.1, demonstrates the capability of the FE model to predict the correct mode of failure of the WSRM walls when they are subjected to the inplane racking load with large (0.5MPa) or small (0.04MPa) vertical pressure loading.

7.5.2 Load-Displacement Response

The load-displacement curves of wall #12 obtained from the FE model and from the experiment are presented in Fig. 7.11. Experimental data show that this wall reached the peak horizontal load at a horizontal displacement of approximately 3mm and dropped the peak load by 20% at approximately 6mm. Some discrepancy was noticeable between the elastic, hardening and softening regimes of the load-displacement curves obtained from the FE model and from the experiment; however, the general trend of the two curves was similar.

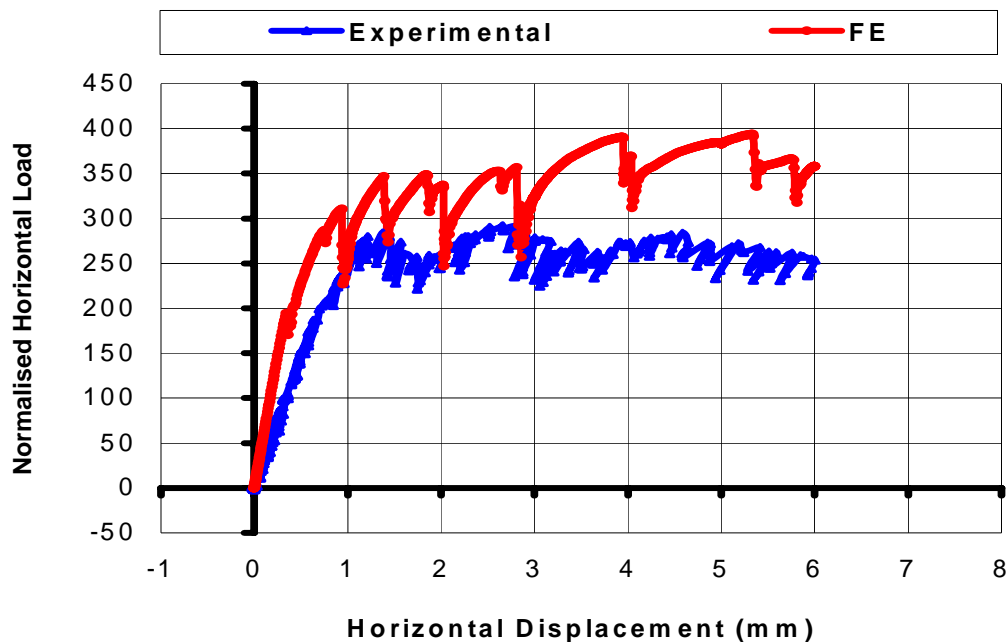


Figure 7.11: Load-displacement response of wall #12

Although the FE model did not experience instability up to lateral displacement of 6mm, the drop in the maximum racking load appeared to have commenced close to 5.2mm lateral displacement as against 3mm in the experiment. No apparent reason was evident for the discrepancies in the elastic range.

7.6 Wall #13

Walls #13 and #14 had an aspect ratio of 1.11 in contrast to 0.84 and 0.50 respectively for the walls of first phase of experiments (#1 to #10) and the walls of Group #7 (wall #11 and #12).

Wall #13 was tested under a vertical compression of 0.25MPa (similar to wall #11). The load-displacement response and the crack pattern of wall #13 obtained from the FE model and from the experiments are presented in this section. The complete load-displacement curve of this wall obtained from the experiments is presented in Appendix C.

A medium density mesh shown in Fig. 7.12 was generated for the analysis of this wall. Sizes of elements for this mesh were similar to those for the walls discussed in Chapter 6. The height of the elements was slightly different due to the different height of this wall.

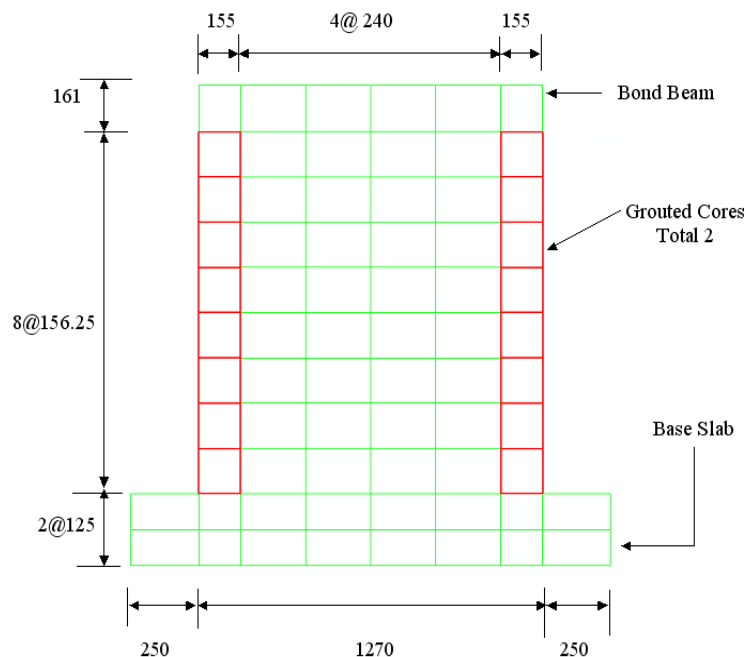


Figure 7.12: Mesh for wall #13 (valid for wall #14)

Plots for the kinetic and internal energies are included in Appendix E.

7.6.1 Mode of Failure

Logarithmic principal strains at the yield load stage (0.5mm horizontal displacement) and at the ultimate load stage (2.3mm horizontal displacement) obtained from the FE model are presented in Fig. 7.13(a) and (b) respectively.

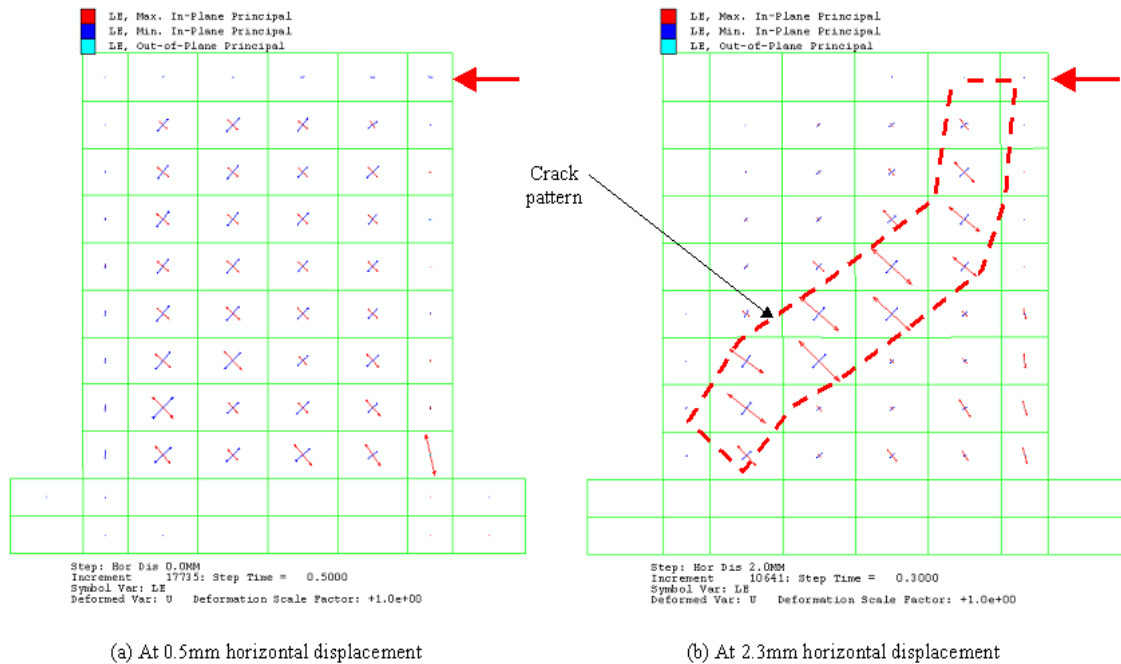


Figure 7.13: Principal logarithmic strains from FE model (wall #13)

The magnitude of the principal strains along the diagonal increased with the increase of the displacement controlled horizontal load. At the ultimate load stage, the final crack pattern of the wall emerged as shown in Fig. 7.13(b).

The state of principal stresses at the yield and the ultimate load stages are shown in Fig. 7.14(a) and (b) respectively. It can be seen from Fig. 7.14(b) that the principal tensile stresses reduced considerably along a line below the diagonal of the wall. The stress was reduced in this region due to the occurrence of cracking.

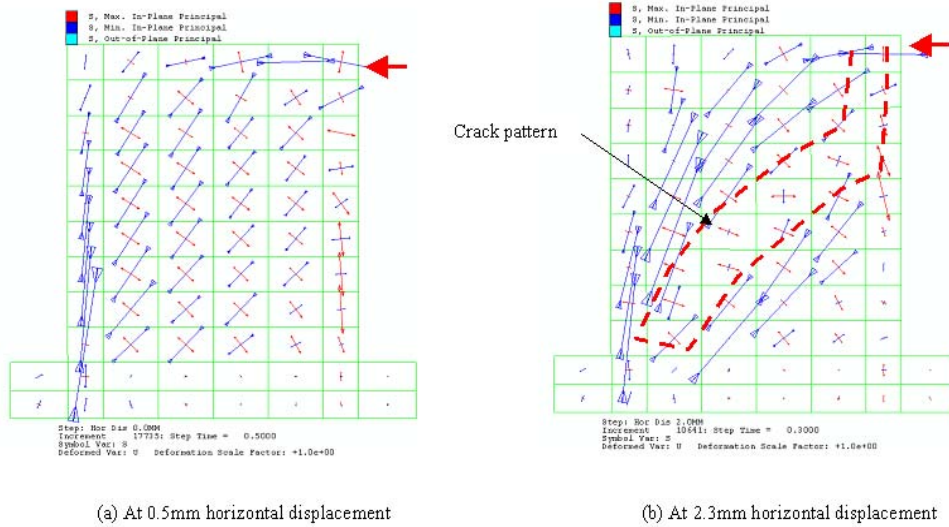


Figure 7.14: Principal stresses from FE model (wall #13)

Photographs of the walls taken during the experiment at the approximate yield load and the ultimate load stages are presented in Fig. 7.15(a) and (b) respectively.

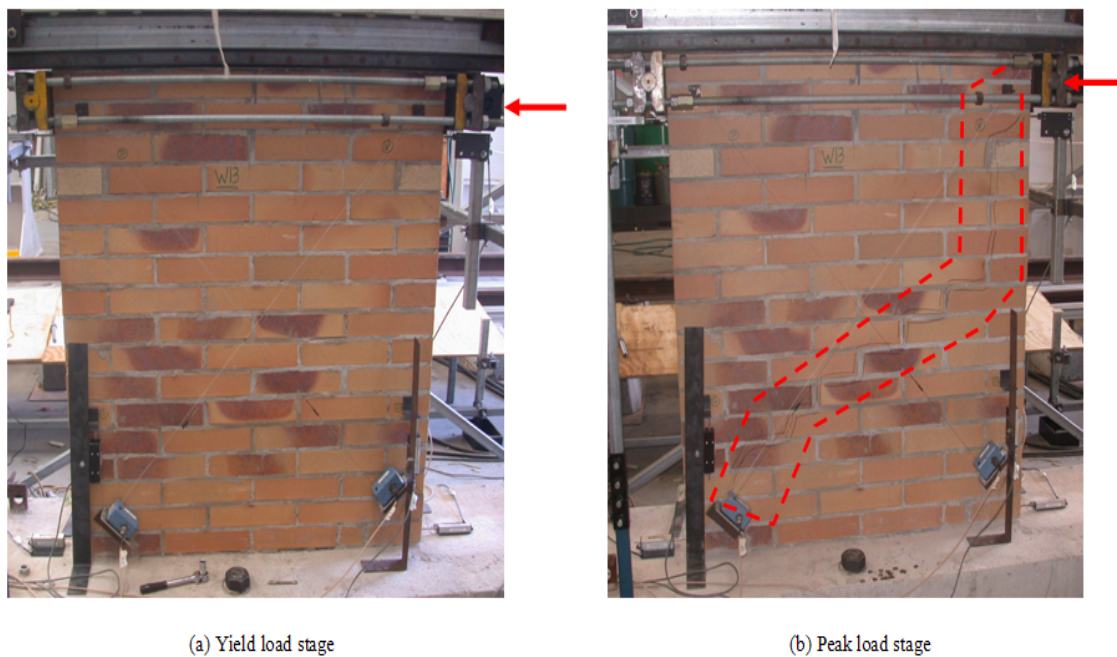


Figure 7.15: Crack pattern from experiment (wall #13)

In contrast to the walls of lower aspect ratio (Group #1, #2, #3 and #7), the major crack did not occur along the diagonal, rather the crack path defined itself below the diagonal as shown in Fig.

7.15(b). It can be seen from Figs. 7.13(b), 7.14(b) and 7.15(b) that the crack pattern inferred from the FE model matched well with that obtained from the experiment.

7.6.2 Load-Displacement Response

The load-displacement curves up to 2.3mm of horizontal displacement obtained from the experiment and predicted by the FE model are presented in Fig. 7.16.

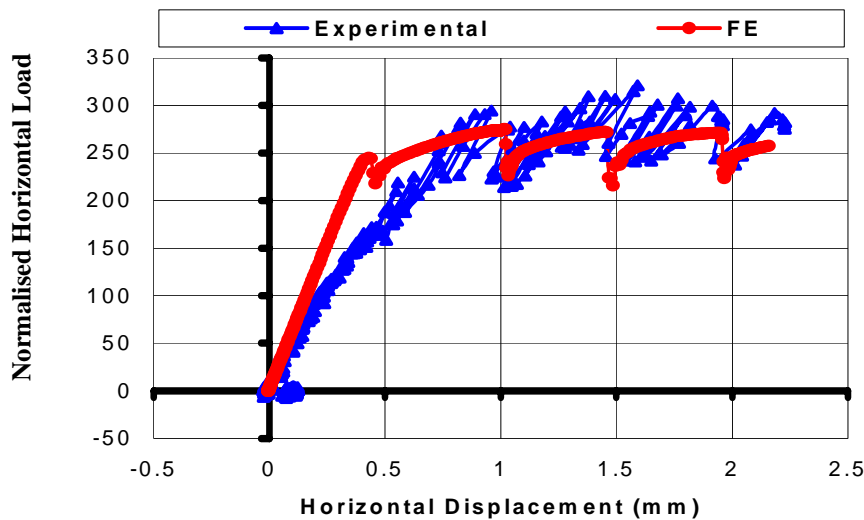


Figure 7.16: Load-displacement response of wall #13

It can be seen from Fig. 7.16 that the two curves showed good agreement in their elastic, hardening and softening regimes. Some discrepancy between the two curves between the horizontal displacements of 0.25mm and 0.75mm was evident. This could be due to very early cracking of the wall due to workmanship effects. The normalised peak loads were also similar (“275” to “300”) for both the curves.

7.7 Wall#14

Wall #14 was similar to wall #13 except that this wall was tested without any vertical load. Therefore, in the FE model the step for the vertical load application was omitted. Plots for the

kinetic and internal energies obtained from the FE model are included in Appendix E. The mode of failure and the load-displacement response of this wall obtained from the FE model and from the experiment is compared in this section. The mesh used for the analysis of wall #14 was similar to that used for wall #13 as shown in Fig. 7.12.

7.7.1 Mode of Failure

Logarithmic strains at the approximate yield load stage (1mm horizontal displacement), and at the ultimate load stage (6.5mm horizontal displacement) obtained from the FE model are presented in Fig. 7.17(a) and (b) respectively.

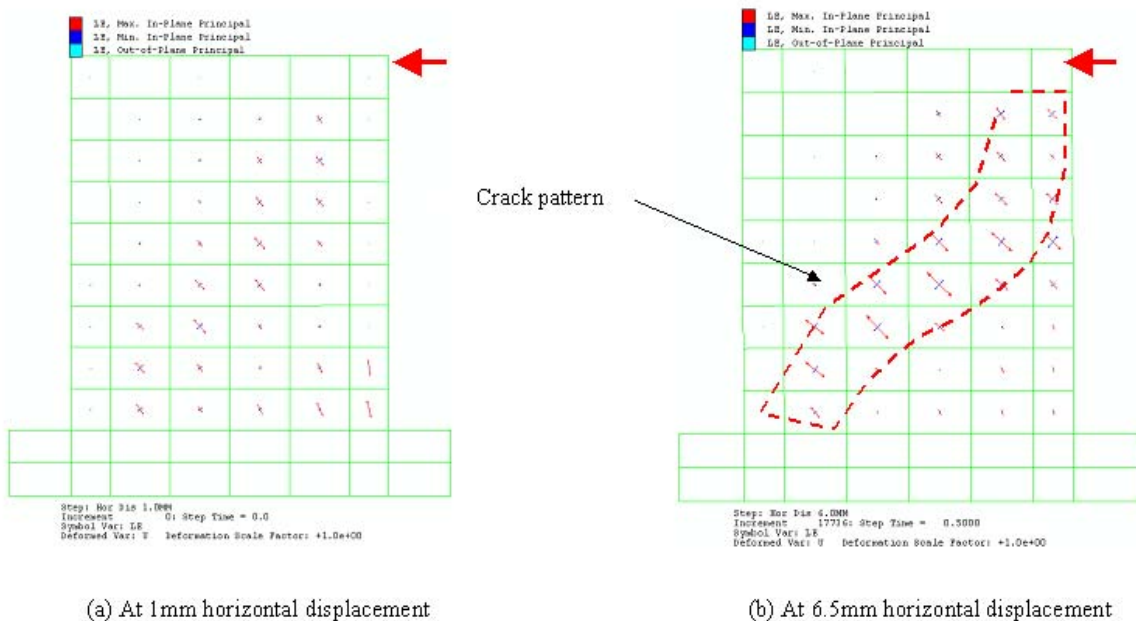


Figure 7.17: Principal logarithmic strains from FE model (wall #14)

Similar to wall #13, the major crack occurred below the diagonal as shown in Fig. 7.17(b). The states of principal stresses at the corresponding displacements are shown in Fig. 7.18(a) and (b) respectively.

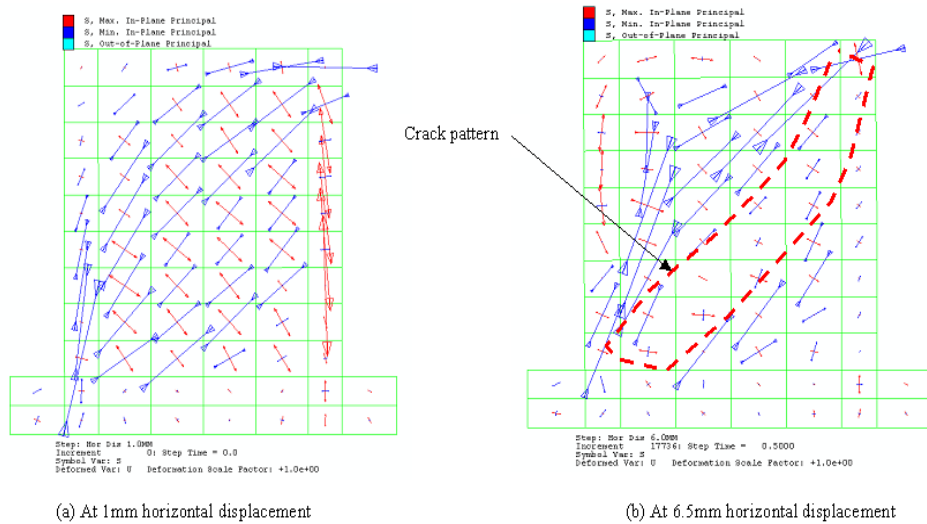


Figure 7.18: Principal stresses from FE model

Similar to wall #13, principal tensile stresses reduced significantly below the diagonal of the wall, exhibiting occurrence of a crack or failure path of the wall. The crack pattern of the wall observed in the experiments at the corresponding load stages is presented in Fig. 7.19(a) and (b) respectively.

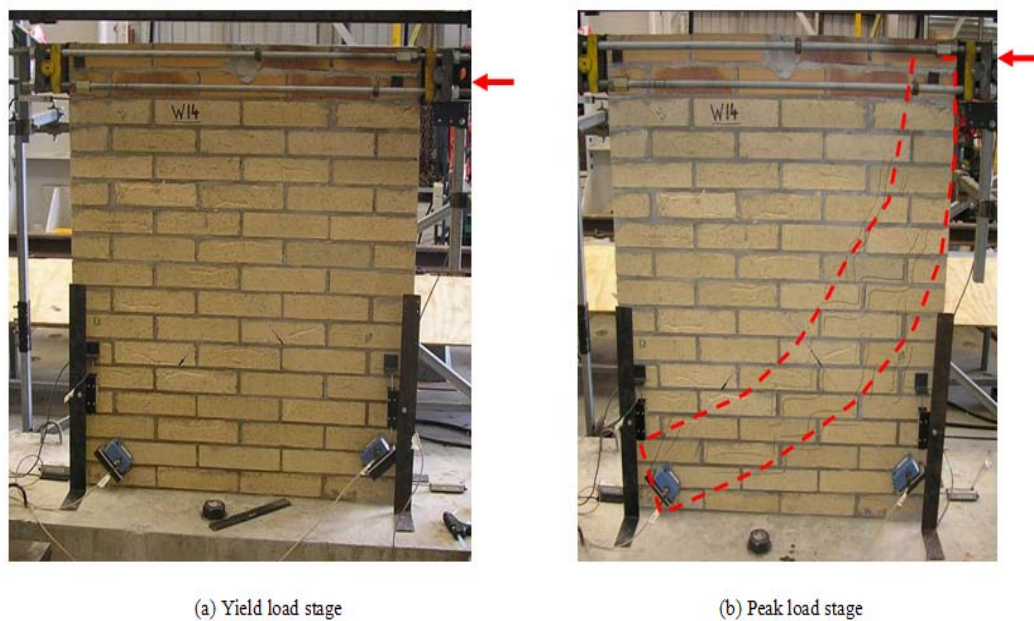


Figure 7.19: Crack pattern obtained from experiment (wall #14)

The crack pattern inferred from the FE model (Figs. 7.17(b), 7.18(b)) matched well with that obtained from the experiment (Fig. 7.19(b)). Similar to walls of Group #7 (wall #11 and #12), the vertical load did not significantly affect the mode of failure of the relatively tall walls (wall #13 and #14).

7.7.2 Load-Displacement Response

The complete load-displacement curve of wall #14 obtained from the experiment is provided in Appendix C. However, the load-displacement curves obtained from the FE model and from the experiments up to 6.5mm of horizontal displacement are presented in Fig. 7.20.

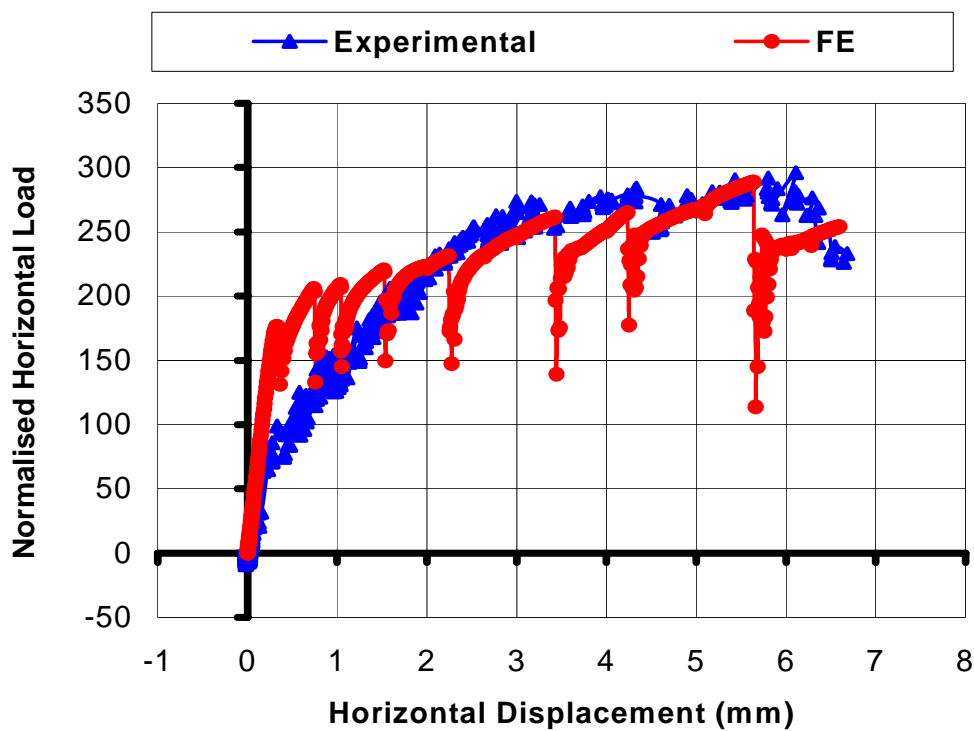


Figure 7.20: Load-displacement response of wall #14

This figure shows good agreement between the two curves in the elastic and the hardening regimes. The peak load and the corresponding horizontal displacement exhibited by the two curves were also similar. Once again some discrepancy existed between the two curves at the early stages of loading in the range of 0.25mm to 1.0mm.

7.8 Discussion

To examine the effect of the aspect ratio and the vertical stress on the shear capacity of the WSRM walls (Groups #1, #2, #3, #7 and #8), design details of the walls and the normalised peak horizontal load obtained from the FE model are provided in Table 7.3. Walls of Group #4, #5 and #6 were of Non-WSRM type hence they are not included in Table 7.3 for discussion.

Table 7.3: Peak normalised load of WSRM walls of different aspect ratio and vertical stress

Group #	Wall #	Size of Walls (L×H×T)	Aspect Ratio of Walls	Vertical Stress (MPa)	Normalised Horizontal Peak Load
7	11	2870×1411×150	0.50	0.25	450
	12	2870×1411×150	0.50	0.04	400
1, 2, 3	1 to 6	2870×2408×150	0.84	0.5	530
8	13	1270×1411×150	1.11	0.25	290
	14	1270×1411×150	1.11	0.00	275

Values of the normalised peak horizontal load reported in column (6) of Table 7.3 were calculated from Eq. 4.2 using the gross area of the wall (length × thickness) and compressive strength of the masonry.

Effect of vertical stress was studied for walls of Group #7 and #8. For Group #7, the normalised load increased only 11.1% with the increase of vertical load by 84%. For Group #8, the normalised horizontal load increased by only 6.6% with the increase of equivalent vertical load from 0MPa to 0.25MPa. The average increase in the shear capacity of the WSRM walls due to increase of vertical stress was 8.9%. The maximum normalised shear capacity of walls of aspect ratio of 1.11 and 0.50 was equal to “290” and “450” respectively. This indicates that the normalised shear capacity increased by 35% with 55% decrease in the aspect ratio. From these

results it may be concluded that the shear capacity of the WSRM walls was greatly affected by the aspect ratio and only marginally by variation in the vertical stress.

The load-displacement responses of the WSRM walls (Groups #1 to #3, #7, #8) predicted by the FE model are presented in Fig.7.21.

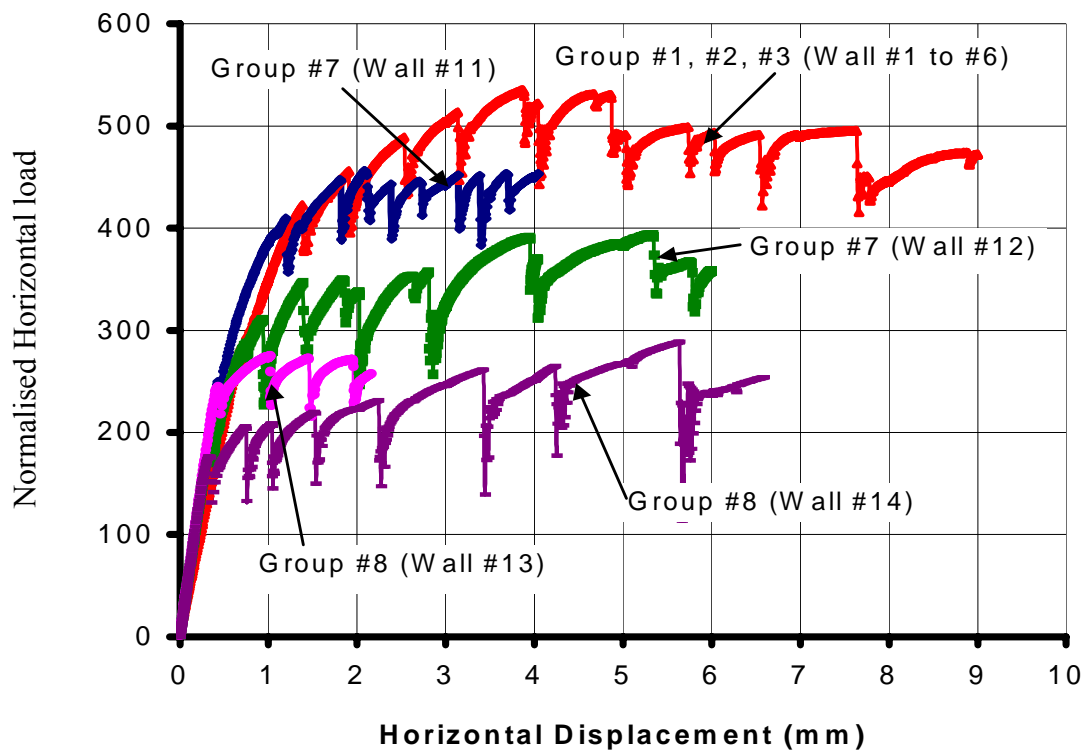


Figure 7.21: Load-displacement curves of WSRM walls

From Fig. 7.21 it can be seen that all the WSRM walls exhibited distinct elastic and hardening regimes. The peak load varied with the aspect ratio as well as with the vertical stress. However, the effect of the vertical stress was smaller when compared with that of the aspect ratio.

7.9 Results of Sensitivity Analysis

To further understand the response of the WSRM walls, sensitivity analyses were performed. WSRM walls of different aspect ratios and subjected to different vertical stresses were analysed

using the FE model. Results for the WSRM walls of aspect ratio 0.50, 0.84 and 1.11 subjected to vertical stress of 0.50MPa, 0.25MPa and 0MPa are discussed in this section.

The load-displacement curves of a WSRM wall of aspect ratio 0.5 subjected to vertical stress of 0.50MPa, 0.25MPa and 0MPa are shown in Fig. 7.22. It appears that with the increase in the vertical stress from 0 to 0.50MPa, the racking load capacity of the wall increased by 40%.

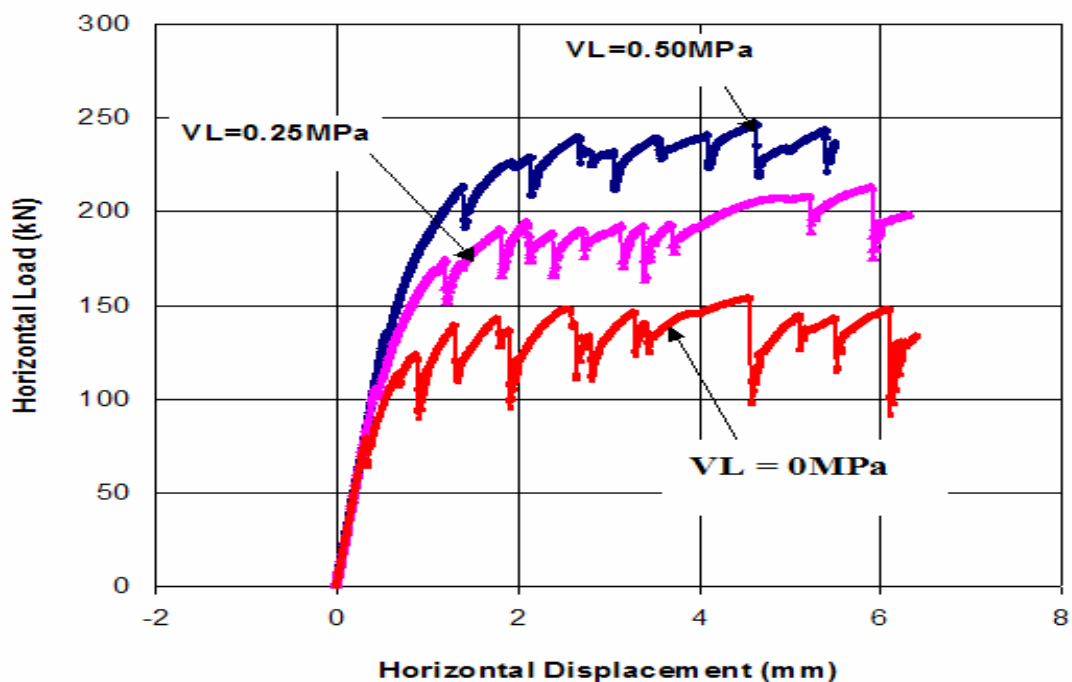


Figure 7.22: Effect of vertical stress on the capacity of a WSRM wall of aspect ratio 0.5

The load-displacement curves of a WSRM wall of aspect ratio 0.84 subjected to vertical stress of 0.50MPa, 0.25MPa and 0MPa are presented in Fig. 7.23. It appears that with the increase in the vertical stress from 0 to 0.50MPa, the racking load capacity of the wall increased by 40%.

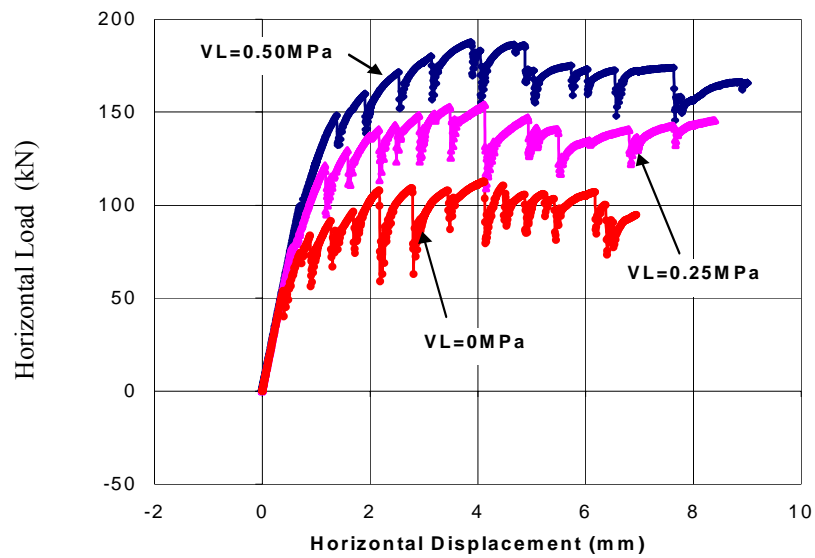


Figure 7.23: Effect of vertical stress on the capacity of a WSRM wall of aspect ratio 0.84

The load-displacement curves of a WSRM wall of aspect ratio 1.11 subjected to vertical stress of 0.50MPa, 0.25MPa and 0MPa are presented in Fig. 7.24

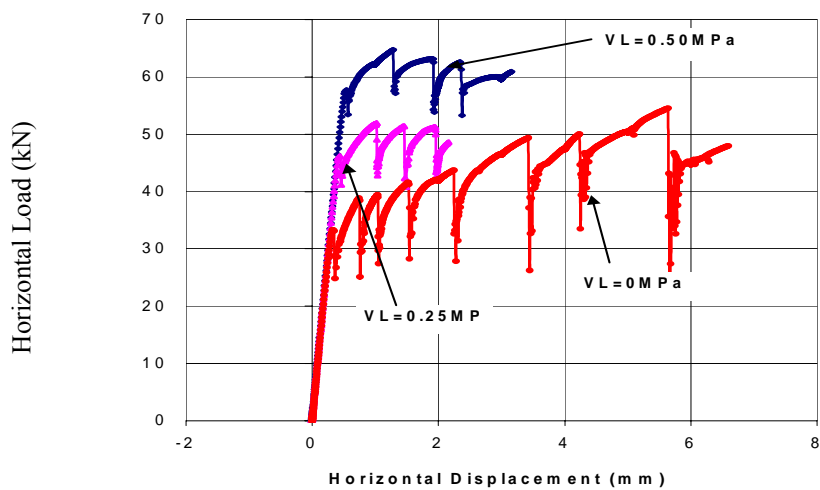


Figure 7.24: Effect of vertical stress on the capacity of a WSRM wall of aspect ratio 1.11

The horizontal load capacity of this wall increased by only 15% with the increase in the vertical stress from 0MPa to 0.50MPa.

The effect of the vertical stress and the aspect ratio on the horizontal load capacity of the WSRM walls can also be seen from Figs. 7.25 and 7.26 respectively.

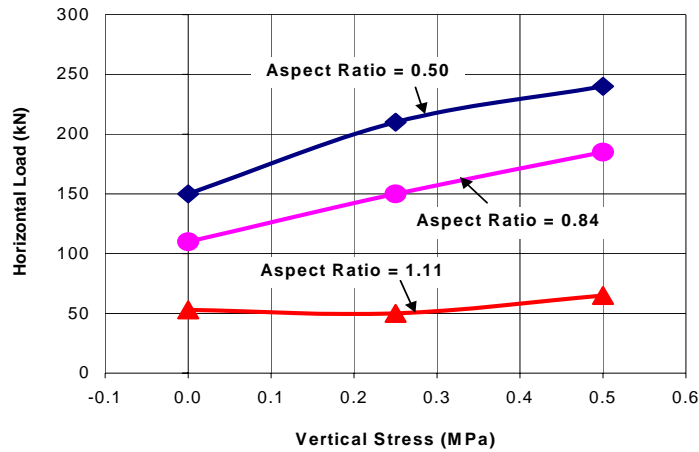


Figure 7.25: Effect of vertical stress (Predicted by the FE Model)

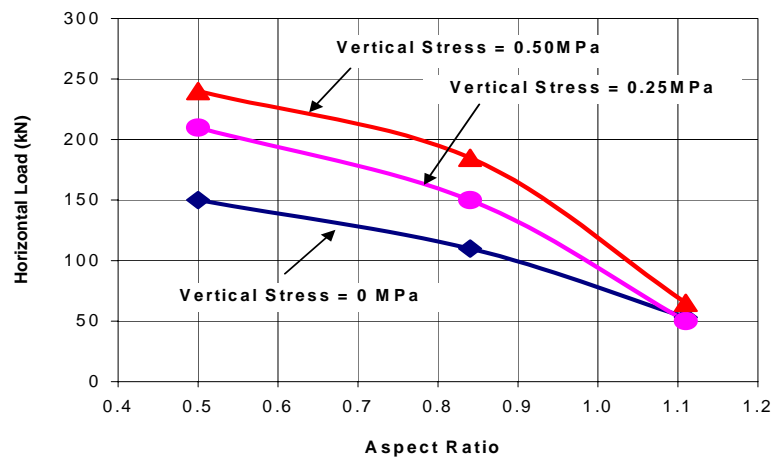


Figure 7.26: Effect of aspect ratio (Predicted by the FE Model)

From these figures, it is evident that with the increase of the vertical stress the racking load capacity of the WSRM walls increased for all aspect ratios, although the walls with larger aspect ratio showed less sensitivity to the vertical load. In general it can be concluded that the racking load capacity of the WSRM walls is more sensitive to the aspect ratio than to the imposed vertical stress.

7.10 Prediction of Shear Capacity

The shear capacities of the validation test walls obtained from the experiments and predicted by AS3700 (2001) and from the FE model are presented in this section. Original values of these shear capacities (without normalisation calculation) obtained from the three methods are provided in Table 7.4.

Table 7.4: Shear capacity of validation test walls

Wall #	Aspect Ratio	Experimental (kN)	AS3700 (2001)			FE Model		
			(kN)	% Difference	Ave Difference	(kN)	% Difference	Ave Difference
11	0.50	179.2	292.1	38.7	44.6%	190.0	5.7	3.1%
12		124.4		57.4		160.0	22.3	
13	1.11	60.6	99.1	38.8		52.0	-14.2	
14		55.9		43.6		55.0	-1.6	

Eq. 5.2 taken from clause 8.6.2 of AS3700 (2001) was earlier discussed in section 5.4.2 and has been used in the calculation of the shear capacity of the WSRM walls. Similar to the walls of the first phase of experiments (aspect ratio= 0.84), this equation excessively over-predicted the shear capacity of the validation test walls that were both relatively squat and tall (aspect ratio of 0.50 and 1.11 respectively). The capacity reduction factor was kept equal to one in the calculations. The AS3700 (2001) formula was found to be non-conservative by up to 57.4% with an average of 44.6%. It becomes evident that AS3700 (2001) is too *non-conservative* for the calculation of the shear capacity of the WSRM walls. On the other hand, the FE model predicted shear capacities of the validation test walls are *non-conservative* but with a reduced level of 22.3% maximum and 3.1% average.

Application of the capacity reduction factor (0.7) to the shear capacities predicted by the FE model will provide results in the safe zone for WSRM walls whereas the equation available in AS3700 (2001) will remain non-conservative even allowing for the capacity reduction factor of 0.7. This equation needs urgent attention and should be critically reviewed.

7.11 Summary

For the verification of the finite element model developed in Chapter 6, four full-scale clay block masonry walls were constructed and tested. Two of these walls (#11 #12) were 2870mm long and 1411mm high, whereas the other two walls (#13 and #14) were 1270mm long and 1411mm high. All walls were 150mm thick. The aspect ratio of walls #11 and #12 was equal to 0.50 and that for walls #13 and #14 was equal to 1.11.

The FE model discussed in Chapter 6 was used for the analyses of the WSRM walls of low to high aspect ratio (0.50 to 1.11) and vertical compressive stress of low to high magnitude (0 to 0.25MPa). The mode of failure and the load-displacement curves of the validation test walls obtained from the FE model and from the experiments have been compared in this chapter.

The crack pattern inferred from the vector plot of logarithmic strains from the FE model has shown a good match with the crack pattern of the WSRM walls obtained from the experiments. A good agreement between the load-displacement curves obtained from the FE model and from the experiments has been obtained. For all the walls, the two load-displacement curves (FE and experimental) have shown an overall good match though some discrepancy in the early stages of loading was evident. This type of problem is inevitable in FE modelling of orthotropic brittle mediums affected by workmanship.

The effect of vertical stress was studied for walls of Group #7 and #8. For Group #7, the normalised load increased only by 11.1% with the increase of vertical load from 0.04MPa to

0.25MPa, whereas for Group #8 the normalised load increased by 6.6% with the increase of vertical load from 0MPa to 0.25MPa. The average increase in the shear capacity of the WSRM walls (examined in this thesis) due to increase of vertical stress was only 8.9%. The maximum normalised shear capacity of walls of aspect ratio of 1.11 and 0.50 was equal to “290” and “450” respectively. This indicates that the normalised shear capacity increased by 35% with 55% decrease in the aspect ratio. From these results it may be concluded that the shear capacity of the WSRM walls was greatly affected by the aspect ratio and marginally by variation in the vertical stress. Sensitivity analyses of the WSRM walls using the validated FE model also exhibited the same effects.

The shear capacity equation available in clause 8.6.2 of AS3700 (2001) is extremely non-conservative for the WSRM walls, with an average over-prediction of 44.6%. The FE model on the other hand over-predicted the shear capacity of the corresponding walls on average by only 3.1%. It becomes evident that AS3700 (2001) is too non-conservative resulting in the unsafe prediction of the shear capacity of the WSRM walls. Application of the capacity reduction factor (0.7) to the shear capacities predicted by the FE model would result in safe shear capacity estimation of WSRM walls, whereas the equation available in AS3700 (2001) will remain non-conservative even after including the capacity reduction factor of 0.7 in the calculation. This equation requires urgent critical review.

CHAPTER 8

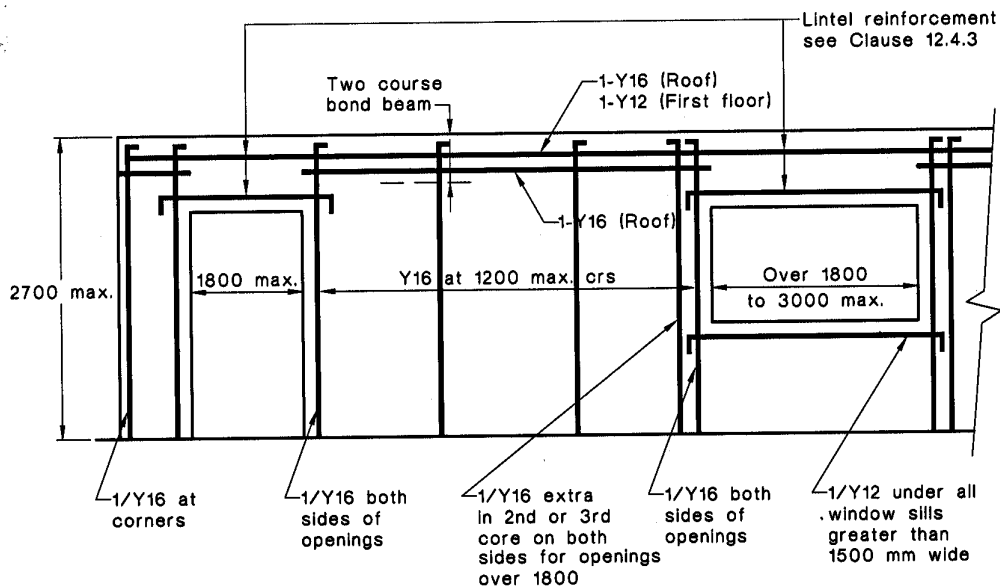
APPLICATIONS OF THE FE MODEL TO IMPORTANT PRACTICAL PROBLEMS

8.1 Introduction

This chapter examines the applications of the FE model developed in Chapter 6 to problems of practical significance. For this purpose, a simplified design of a WSRM shear wall (one of the prescriptive designs in AS3700 (2001)) suitable for small buildings in the Australian regions of wind categories N4, C2 and earthquake categories H1, H2, H3 was selected. This wall was modelled and analysed using the FE model developed in this thesis. Vertical grouted reinforced cores and the bond beams were modelled using the REBAR option and the damaged plasticity concrete material model available in ABAQUS (2005). For unreinforced masonry sections of the wall, a user material subroutine (VUMAT) described in Chapter 6 was used. It has been shown that the FE model could predict sensible load flows, stress distributions and failure modes of such walls. Shear capacity of the selected wall obtained from the FE model is compared with the racking load tabulated in AS3700 (2001). The effect of the width of openings and variation in the masonry material parameters on the load-displacement and ultimate shear capacity of the wall is investigated.

8.2 Masonry Wall for Wind Category N4, C2

A prescribed design in AS3700 (2001) for a masonry shear wall suitable for small buildings in the Australian regions of wind category N4, C2 and earthquake category H1, H2, H3 is presented in Fig. 8.1. Details of the wind categories for housing and the earthquake categories for the Australian regions can be found in AS4055 (2006) and AS1170.4 (1993) respectively. This design prescription is provided in Fig. 12.8(B) of AS3700 (2001) and is re-produced in Fig. 8.1. This wall contains a maximum 1.8m wide opening for the door and a maximum 3m wide opening for a window within its length. Reinforcement details and the location of the bond beams are also prescribed as shown in the diagram. Vertical reinforcement has been prescribed at the ends of openings and at a maximum spacing of 1.2m for the WSRM section of the wall. 16mm diameter bars (Y16 in Fig. 8.1) for the vertical grouted cores and 16mm and 12mm diameter bars for the bond beams are prescribed in this design.



NOTE: Suitable for earthquake design categories H1, H2 and H3.

DIMENSIONS IN MILLIMETRES — NOT MORE THAN 12 M WIDE

Figure 8.1: Simplified design prescribed by AS3700 (2001) for a 190mm thick masonry wall

This selected design (Fig. 8.1) was examined using the FE model developed in this thesis. AS3700 (2001) provides tables for racking load for small buildings containing these walls for different wind categories. The ultimate racking force for the wall shown in Fig. 8.1 was read from chart K1 (j) of AS3700 (2001). Ultimate racking force resisted by the gable end of the 16m wide single or upper storey building with 30° roof slope was 142kN and for the subfloor of a single storey maximum 1000mm above ground (high-set building) was 216kN. For a symmetric building as shown in Fig. 8.2, only half the load carried by the gable end is transferred to the WSRM shear wall.

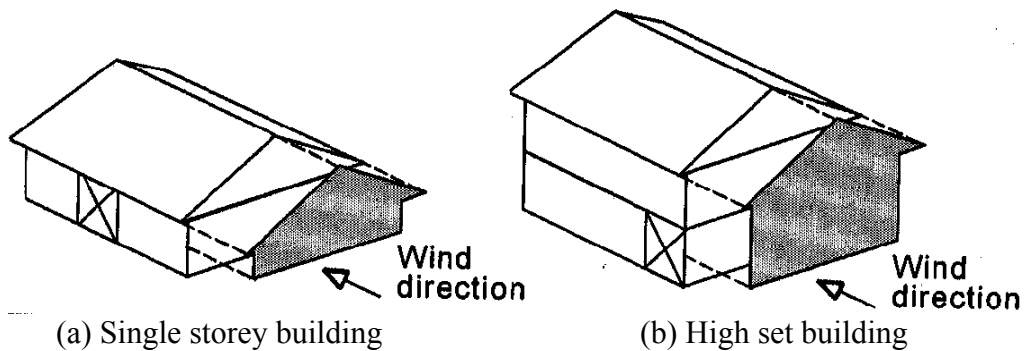


Figure 8.2: Racking load directions for gable ends of small buildings

Based on the code provisions (AS3700 (2001)), the maximum racking load carried by the wall shown in Fig. 8.1 would be equal to 71kN for single or upper storey building and 108kN when it forms part of an elevated single storey building maximum 1m above ground high-set building. These prescribed maximum loads were divided by the capacity reduction factor (0.75 as per clause 4.4 of AS3700 (2001)) to enable comparison with the FE predicted capacity. Therefore, modified values would be 95kN and 144kN respectively for single storey and high-set building shear walls.

8.2.1 Finite Element Modelling

The FE model developed in Chapter 6 and verified in Chapter 7 for the analysis of WSRM walls was applied to determine the shear capacity of this practical problem. A WSRM shear wall of 11m length with two large openings shown in Fig. 8.3 was modelled and analysed using the FE model. A medium density mesh was generated for the analysis of this wall. Steps similar to those used for the analyses of the WSRM walls reported in Chapters 6 and 7 were followed in the analysis of this wall. Material parameters for the URM section, the grout and the reinforcement were kept the same as those for the previously considered WSRM walls.

The input data used for the current wall are as follows: area of each 16mm diameter reinforcement bar was 200mm^2 ; thickness of the hollow masonry was 90mm (45mm face shell thickness) for 190mm hollow masonry blocks; thickness of the grouted cores was 190mm; and the thickness of the bond beam and the base slab was 190mm and 1000mm respectively.

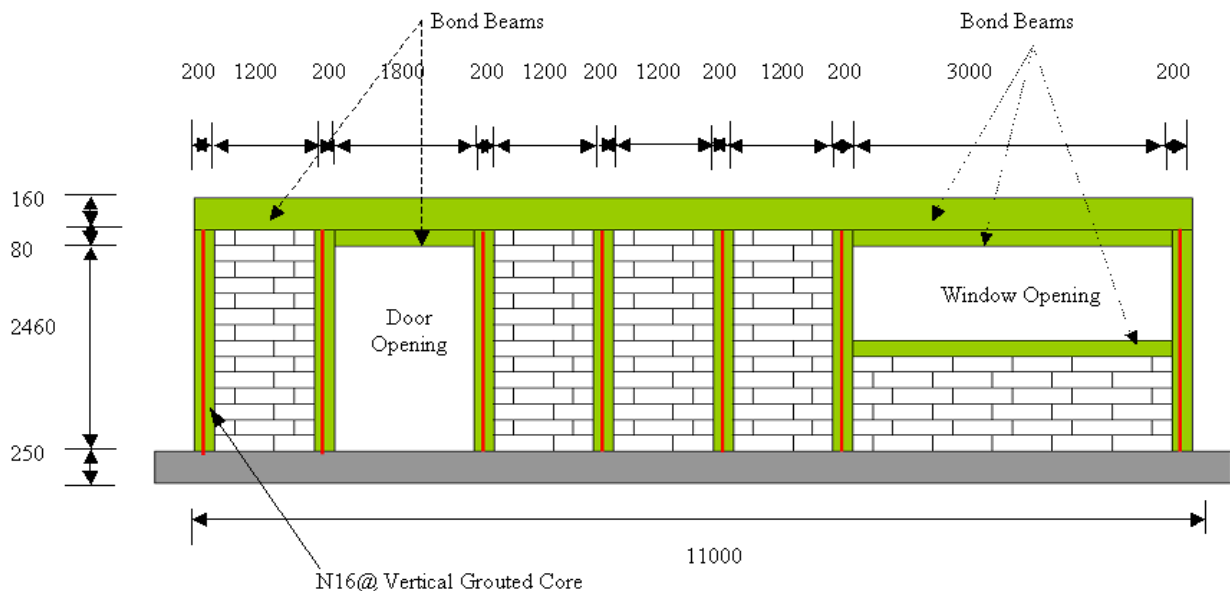


Figure 8.3: Wall modelled for the FE analysis

No vertical load was imposed since the ultimate capacity of the wall without the effect of the vertical load would provide the worst-case scenario. To examine the effect of the width of openings, different meshes were generated and analyses were performed.

8.3 Variability in Masonry Properties

Variability in the material properties of masonry cannot be completely eliminated; therefore, the effect of variation of the masonry material on the structural behaviour of the masonry walls is essential and is considered in this section.

A Standard Normal Distribution curve is commonly used for accounting for variation of data for many engineering applications. Therefore it is adapted to account for the variability of masonry material properties for the WSRM walls considered in this chapter. As per this curve, data with one standard deviation from the mean accounts for about 68% of the data set, data with two standard deviations from the mean accounts for about 95% of the data set and data with three standard deviations from the mean accounts for about 99.7% of the data set.

In order to account for the effect of variability of masonry properties, three standard deviations are used in this chapter. By adapting three deviations from the mean values, all types of masonry (clay block masonry, concrete block masonry, and calcium silicate masonry) could be accounted.

In order to calculate the maximum and minimum possible values for the Australian masonry material parameters, a coefficient of variation equal to 20% and three standard deviations are assumed in this chapter. Mean values of masonry properties used for the FE analysis of the walls are provided in Table 6.2 and the maximum and the minimum values of masonry material parameters are measured from Eq. 8.1.

$$\text{Max/Min Value} = \text{Mean} \pm 3 \times (\text{cov} \times \text{Mean}) \quad (8.1)$$

Highest (stronger masonry) and lowest (weaker masonry) values of masonry material parameters for 20% COV and three deviations from the mean values provided in Table 6.2 are shown in Table 8.1.

Table 8.1: Range of masonry material parameters

Parameter	Units	Average Masonry	Stronger Masonry (+3SD)	Weaker Masonry (-3SD)
f_{tx}	MPa	0.60	0.96	0.24
G_{fx}	(N-mm/mm ²)	1.0	1.6	0.4
f_{ty}	MPa	0.35	0.42	0.28
G_{fy}	(N-mm/mm ²)	0.5	0.8	0.2
f_{cx}	MPa	3.0	4.8	1.2
G_{fcx}	(N-mm/mm ²)	0.302	0.483	0.121
f_{cy}	MPa	18.0	28.8	7.2
G_{fcy}	(N-mm/mm ²)	4.35	6.96	1.74

Other material parameters required for the material model adopted in this chapter were equal to the values provided in Table 6.2. Using the means, and the highest and lowest values of masonry material parameters provided in Table 8.1, two WSRM walls (#15 and #16) were analysed using the FE model developed in this thesis and the results are discussed in sections 8.4 and 8.5 respectively.

8.4 Wall with Prescribed Design (Wall#15)

A mesh shown in Fig. 8.4 was generated to be used for the analysis of an 11m long wall shown in Fig. 8.3. The width of the door opening and the window opening was 1.8m and 3.0m respectively whereas the width of the WSRM section between the two major openings was equal to 4.4m. The width of each grouted core was 200mm and the width of the unreinforced masonry panels enclosed by the vertical grouted cores and the bond beam was 1.2m. The width and height of the reduced integration plane stress elements (CPS4R) used for unreinforced masonry panels was 300mm and 180mm respectively.

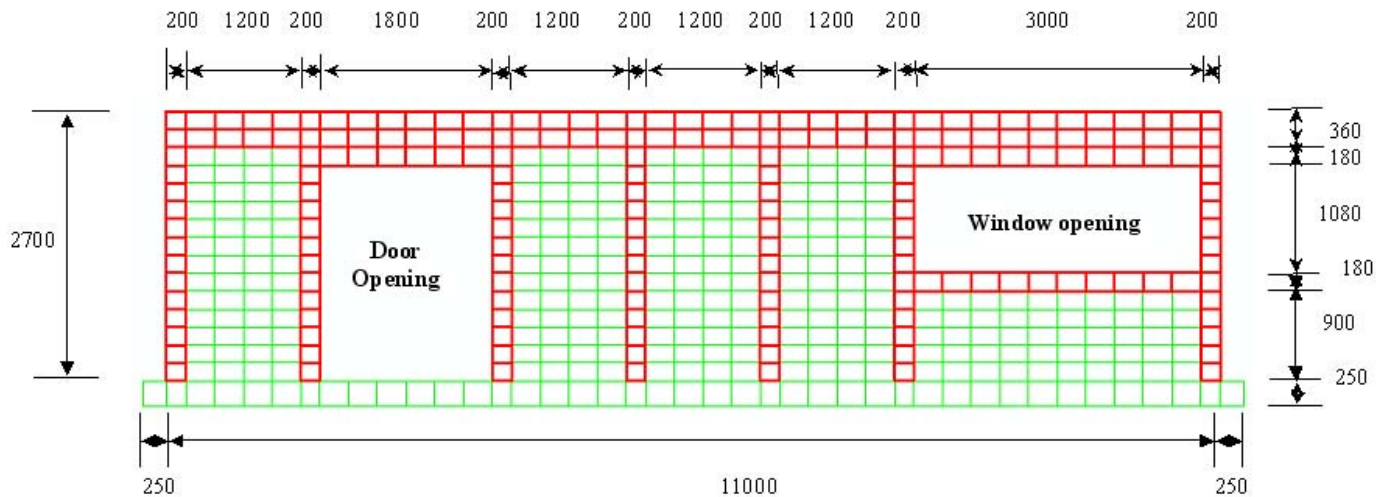
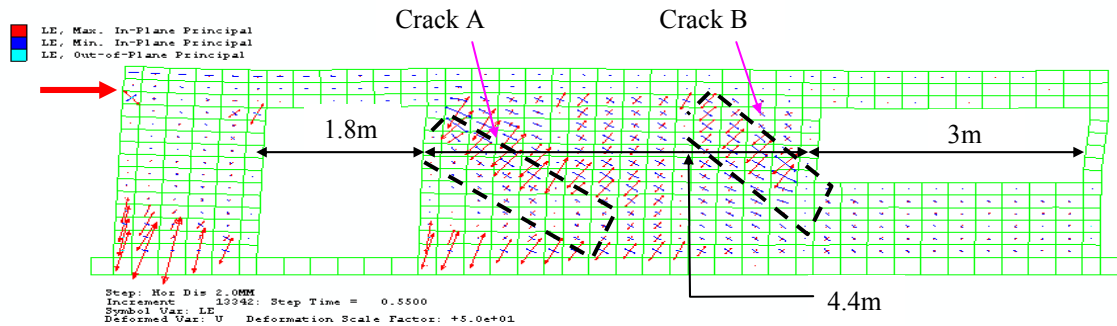


Figure 8.4: Mesh used for the analysis of wall #15

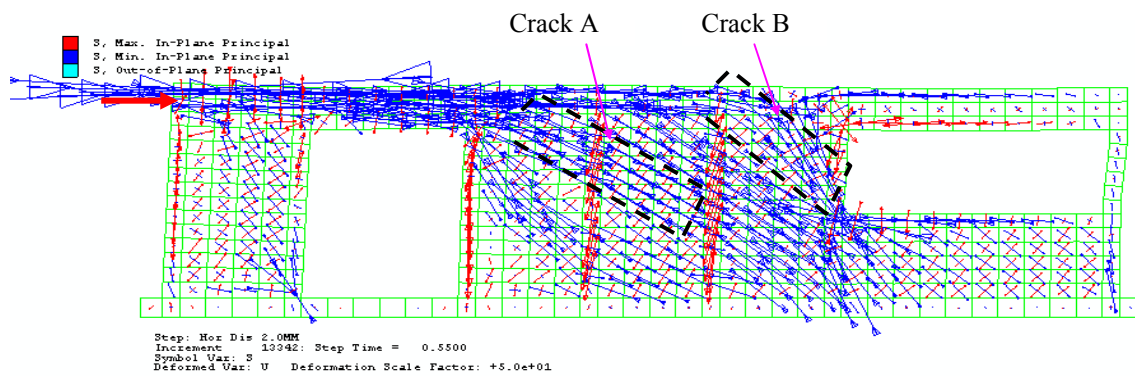
The bond beams and the vertical grouted cores were modelled as per the vertical and the horizontal reinforcement shown in Fig. 8.3. Only the elastic parameters (Young's modulus and Poisson's ratio) were defined for the bond beams, however complete compression hardening and tension stiffening data were provided to the FE model for the grout of the vertical reinforced grouted cores. The average masonry material parameters provided in Table 6.2 and stress-strain data for the reinforcement bars and compression hardening and tension stiffening data for the grout provided in Table 6.1 were provided to the FE model. Other steps discussed in Chapter 6 for the processing of the analyses were followed and results were extracted. Relevant energy criteria were also met for the stable solution.

Plots for the principal logarithmic strains and the principal stresses are presented in Fig. 8.5(a) and (b) respectively. It can be seen from Fig. 8.5 that the applied horizontal load concentrated mainly at the WSRM section between the two openings. Other sections appear to be resisting only a minor proportion of the horizontal load. Some heel tension was observed, however, the failure of the wall appears to be due to the diagonal failure of the middle WSRM section. Since the bond beams were modelled as elastic mediums, no significant failure was noticed in them.

Higher magnitudes of the logarithmic strain vectors along two separate diagonals (see Fig. 8.5(a)) show the occurrence of two major cracks (crack A and crack B).



(a) Vector plot of principal logarithmic strains



(b) Vector plot of principal stresses

Figure 8.5: Principal strains and principal stresses for wall #15 (forward loading)

Significant reduction in the magnitude of the principal stresses in the corresponding regions (see Fig. 8.5(b)) confirmed the occurrence of the diagonal cracks. Stress concentration in the path of the load flow at the corners of the openings was noticed, which is a typical engineering mechanics fundamental. It is important to note that the magnitude of the principal stresses in the WSRM section on the left side of the door opening and in the WSRM section below the window opening were quite low. This indicates that most of the applied horizontal load was resisted by the WSRM section between the two openings.

Displacement controlled horizontal load was applied in the reverse direction at the opposite end of the bond beam (right hand side of the window opening) at the top of the wall. Principal logarithmic strains dominated the diagonal of the middle WSRM section of the wall as shown in Fig. 8.6(a). Reduction in the principal stresses was also noticed along the diagonal of the middle WSRM section as shown in Fig. 8.6(b).

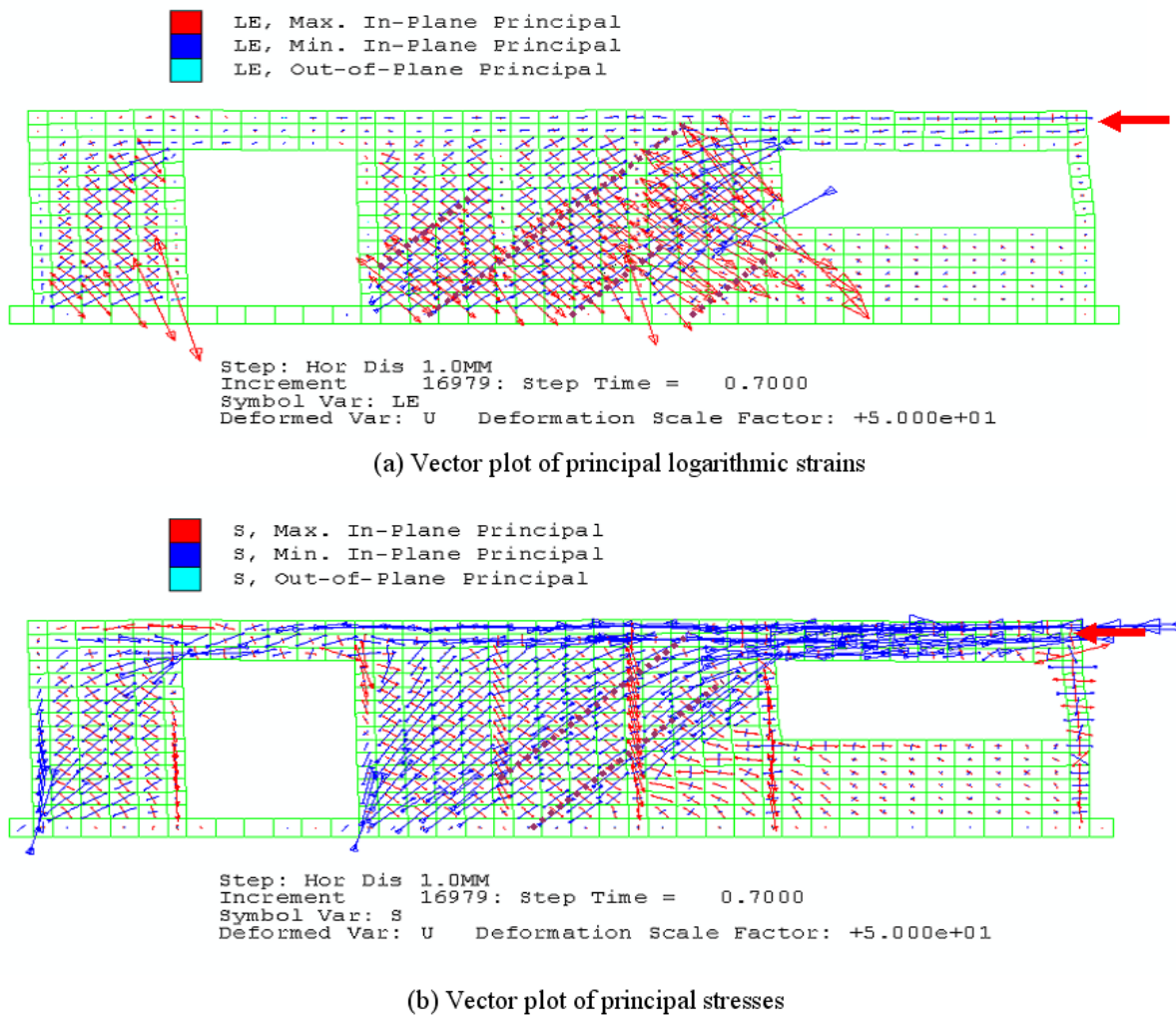


Figure 8.6: Principal strains and principal stresses for wall #15 (reverse loading)

Differences in the distribution of principal logarithmic strains and stresses shown in Figs. 8.5 and 8.6 were due to the different width of the WSRM sections at the two ends of the wall. For forward loading (Fig. 8.5), the 1.6m wide WSRM end panel transferred the load to the middle

WSRM section whereas for the reverse loading (Fig. 8.6), only a 0.2m wide vertical grouted core was available to transfer the load.

The load-displacement response of wall #15 obtained from the FE model for the forward and reverse loadings using average masonry material parameters is presented in Fig. 8.7. No significant softening was predicted. Fig. 8.7 shows that, under forward loading, wall #15 that was modelled as per the design prescription provided by AS3700 (2001) reached its ultimate load capacity of 350kN at approximately 2.5mm of horizontal displacement. Under the reverse loading, the same wall reached its ultimate load capacity of 275kN at approximately 1.8mm of horizontal displacement.

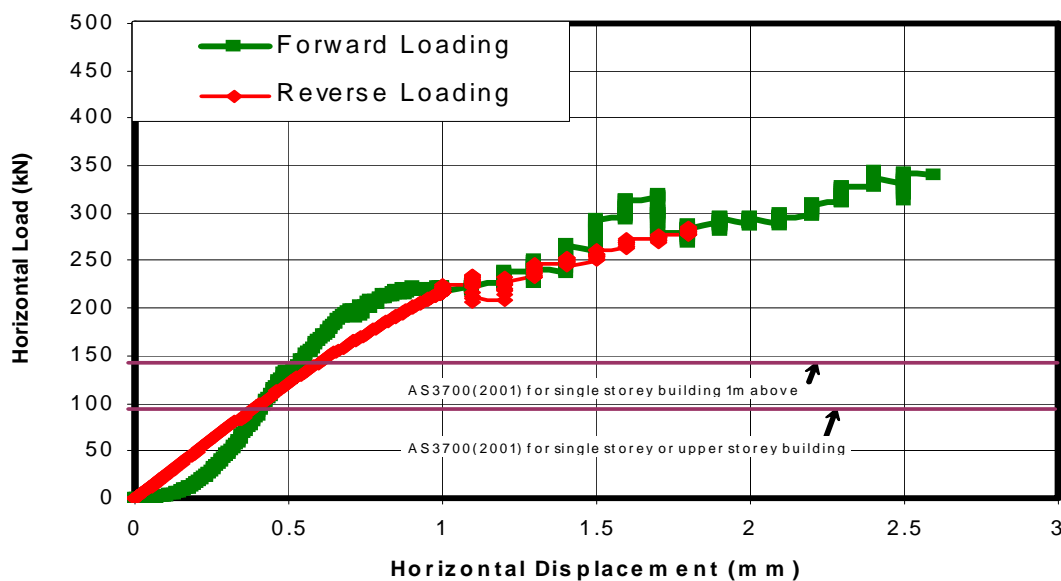


Figure 8.7: Load-displacement curve of wall #15 (Average Masonry)

The ultimate load predicted by the FE model for the forward loading and reverse loading was respectively 2.4 and 1.9 times the shear capacity value of 144kN prescribed by AS3700 (2001) for the high-set building shear walls. For the single storey and upper storey buildings, the ultimate load capacity predicted by the FE model was 3.7 and 2.9 times of the shear capacity value of 95kN prescribed by AS3700 (2001).

8.4.1 Effect of Material Variability on Wall #15

Using average, stronger and weaker masonry material parameters provided in Table 8.1 and the other material parameters given in Table 6.2, wall #15 was analysed by applying the loading in the forward and reverse directions and the load-displacement curves are shown in Figs. 8.8 and 8.9 respectively.

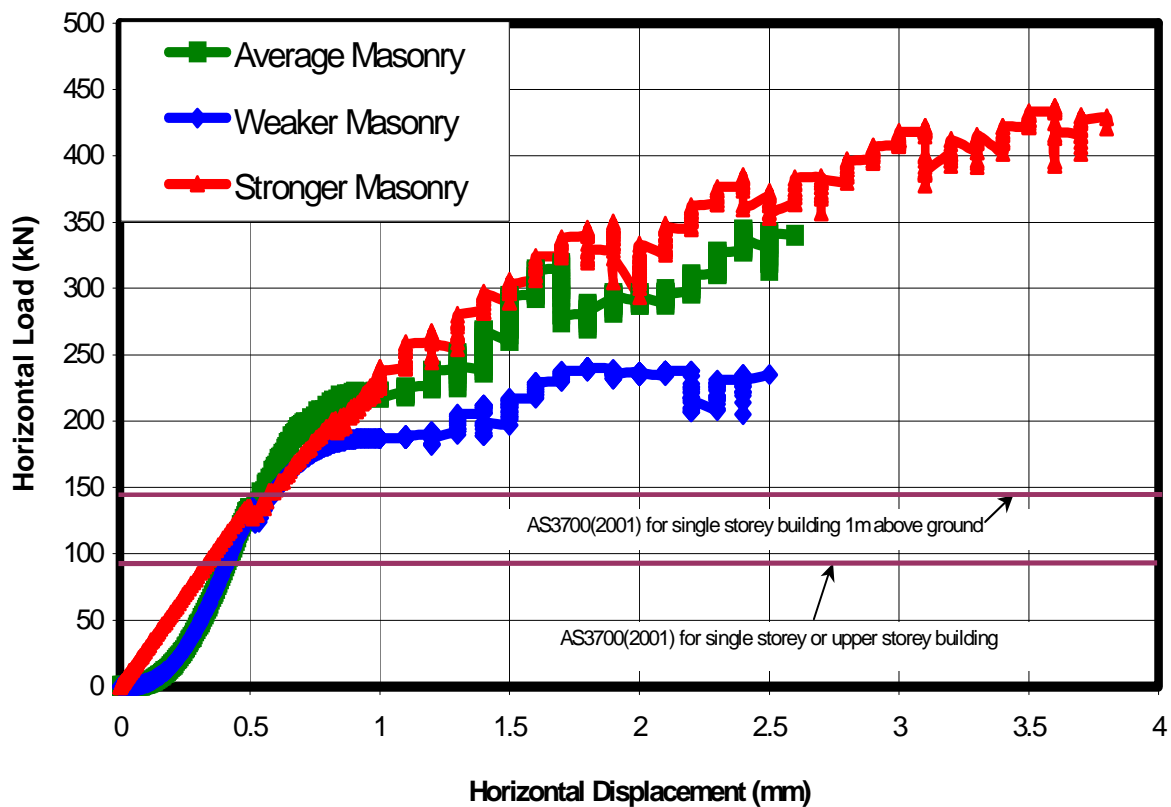


Figure 8.8: Load-displacement curve of wall #15 in the forward direction

From Fig 8.8, it is evident that, for wall #15 made either from clay block masonry or concrete block masonry or calcium silicate masonry, its actual shear capacity is more than its shear capacity value prescribed in AS3700 (2001). The load-displacement response of wall #15 in the reverse direction using average, stronger and weaker masonry is provided in Fig. 8.9.

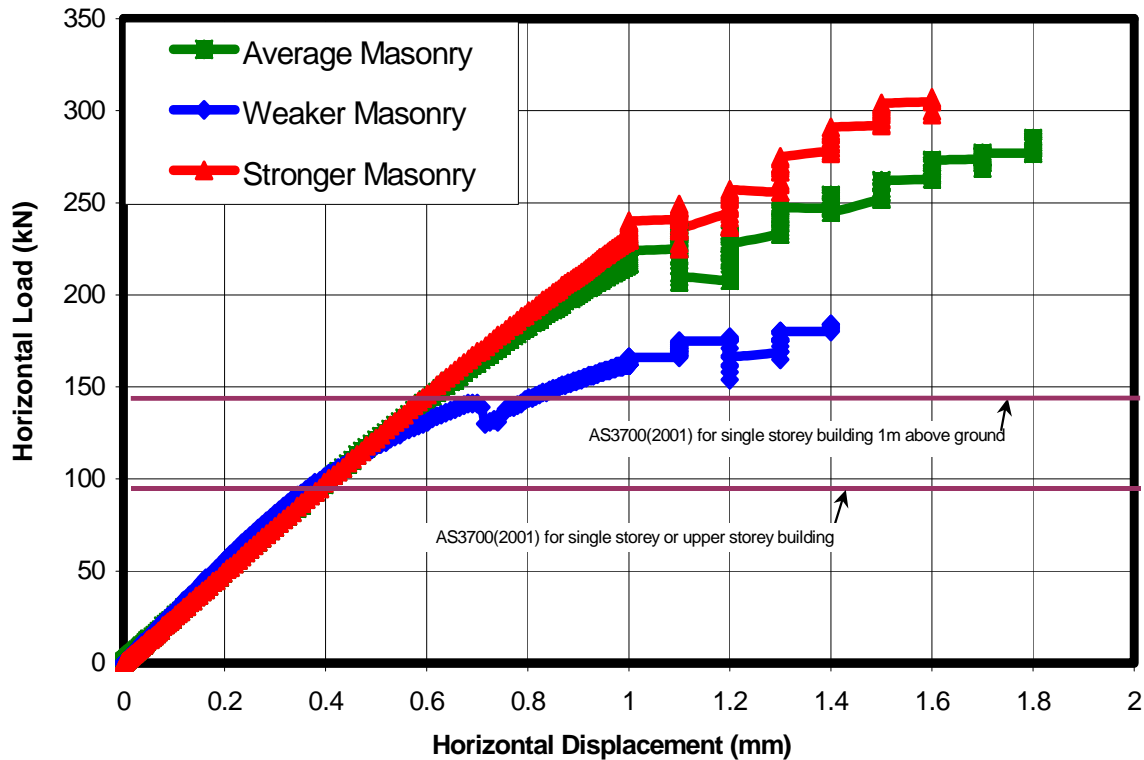


Figure 8.9: Load-displacement curve of wall #15 in the reverse direction

From Fig 8.9, it is evident that, for wall #15 loaded in the reverse direction, the shear capacity predicted by the FE model is higher than the shear capacity values prescribed by AS3700 (2001). Predicted shear capacity values of wall #15 in the reverse direction are smaller than those in the forward direction, however, the reverse direction shear capacity values are slightly bigger than the AS3700 (2001) prescribed values. Based on the FE analysis, it appears that the prescribed shear capacity values for WSRM walls for small buildings are sensible for the weaker masonry and a little conservative for stronger masonry. It would be ideal to include an engineering procedure for the design and analysis of such walls in AS3700 (2001) which will account for the material variability.

8.5 Wall with Relatively Large Openings (Wall #16)

AS3700 (2001) prescriptions (Fig. 8.1) do not allow for increase in the width of opening. The effect of the width of the opening to the shear capacity of the masonry walls (wall #15), as discussed in section 8.4, was further studied by increasing the width of the door opening from 1.8m to 3.2m and keeping all other parameters the same. The mesh generated for the modified wall (#16) design is shown in Fig. 8.10. The FE analysis was performed as described before and the response was interpreted.

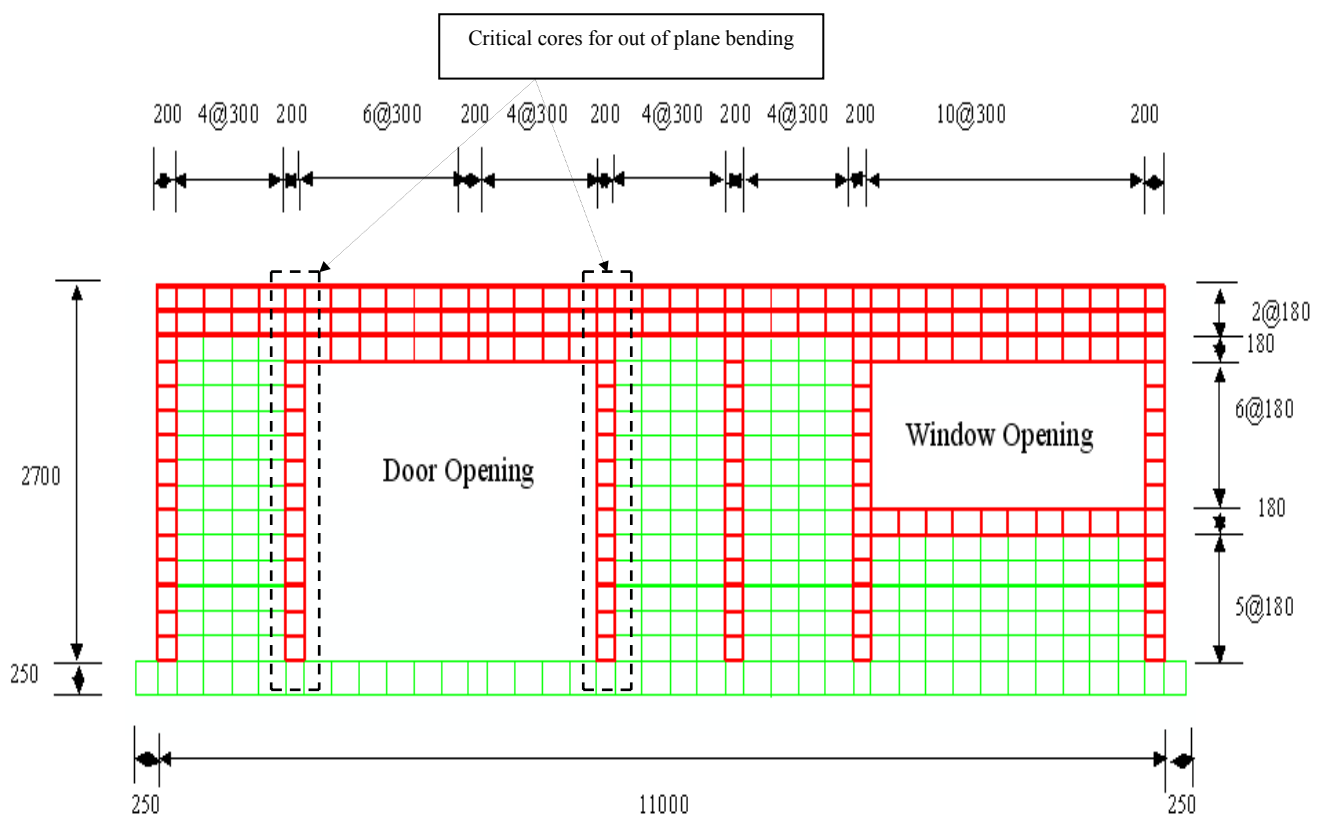


Figure 8.10: Mesh used for the analysis of wall #16

No vertical load was applied and the horizontal displacement was applied in the forward direction in multi steps using average masonry material parameters. Plots for the principal logarithmic strains and the principal stresses are presented in Fig. 8.11(a) and (b) respectively.

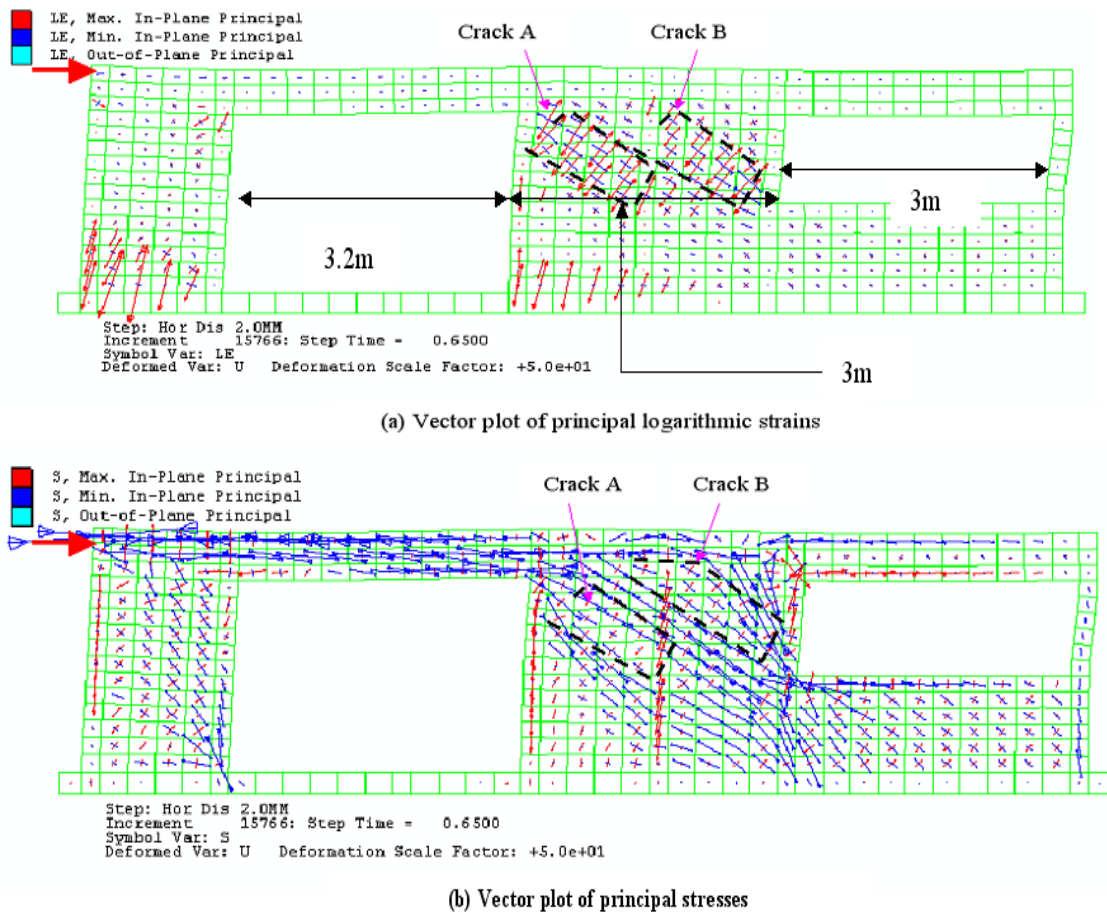


Figure 8.11: Principal strains and principal stresses for wall #16 (forward loading)

The width of the door opening for this wall (wall #16) was equal to 3.2m, which resulted in the reduction in the width of the middle WSRM section from 4.4m to 3m. In spite of such a significant increase in the width of the door opening (from 1.8m to 3.2m or 78% increase) and the corresponding reduction in the width of masonry between the openings, the load flow remained continuous similar to wall #15. The higher magnitude of principal strain vectors and the lower magnitude of principal stress vectors at two locations in the middle WSRM section of the wall indicated occurrence of two cracks (A and B). The distance between the two cracks decreased due to the reduced width of the middle WSRM section. Some heel tension was also noticed in this wall; however, the ultimate failure appears to be due to the diagonal failure of the WSRM section between the two openings.

Displacement controlled horizontal load was applied in the reverse direction at the opposite end of the bond beam (right hand side of the window opening) at the top of this wall. Similar to forward loading, under reverse loading logarithmic strains dominated the diagonal of the middle WSRM section as shown in Fig. 8.12 (a). However, one crack appeared in contrast to two cracks under forward loading. This was due to the shorter width of the WSRM section at the right side of the window opening where the reverse loading was applied. Reduction in the principal stresses was also noticed along the diagonal of the middle WSRM section as shown in Fig. 8.12(b).

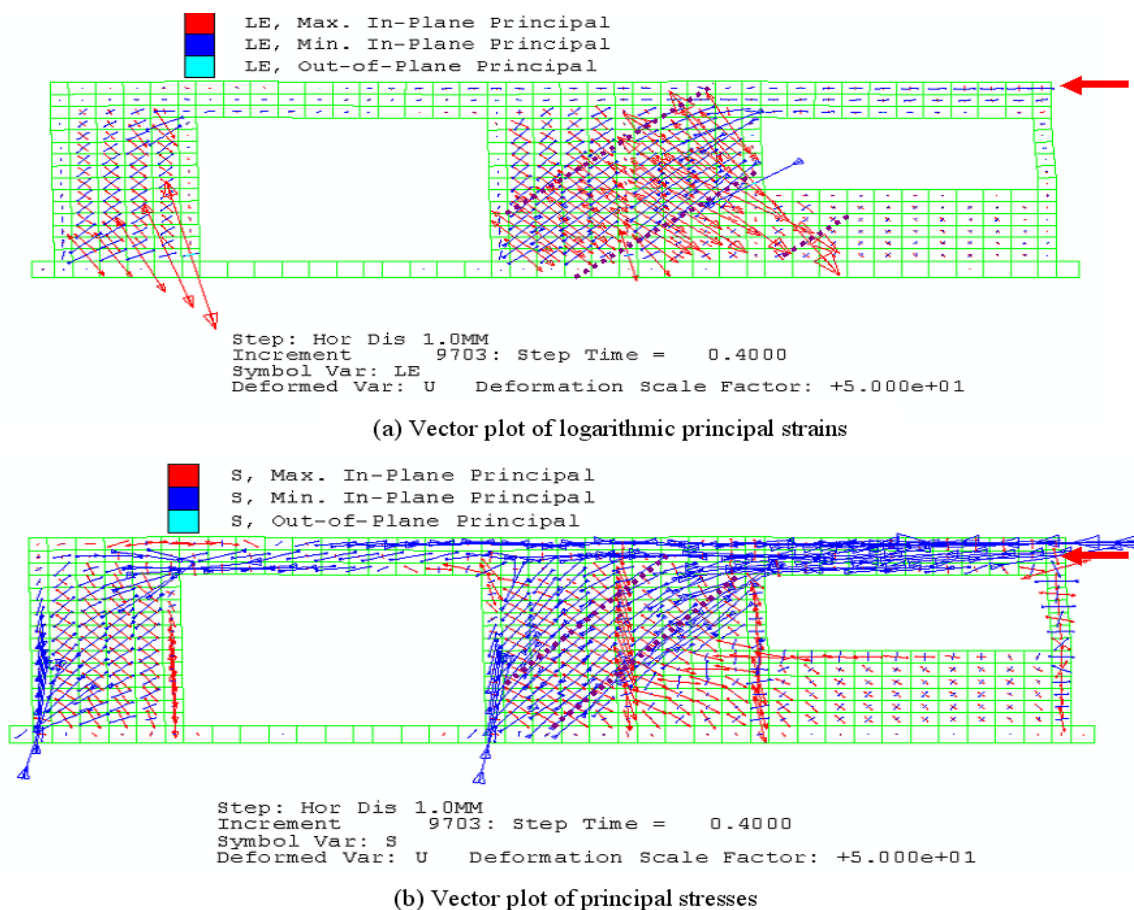


Figure 8.12: Principal strains and principal stresses for wall #16 (reverse loading)

It becomes evident that, similar to wall #15, the cracking pattern of wall #16 was also affected by the width of the end WSRM section. Most of the applied load was resisted by the middle WSRM section.

The load-displacement curves of wall #16 obtained from the FE model under forward and reverse loadings using average masonry material parameters are presented in Fig. 8.13. No significant softening was noticed for this wall similar to wall #15. Fig. 8.13 shows that the ultimate shear capacity of wall #16 under forward and reverse loading was approximately equal to 250kN and 175kN respectively. Both of these values are 100kN less than that of the corresponding values for wall #15. In other words, due to the increase in the width of the door opening and the corresponding reduction in the width of the WSRM panel between the two openings, the ultimate load capacity of this wall under the forward and reverse loading was reduced by 29% and 37% respectively. However, shear capacity of this wall (wall #16) under forward and reverse loading was still 42% and 18% higher than the modified prescribed shear capacity of 144kN in AS3700 (2001) for high-set building shear walls.

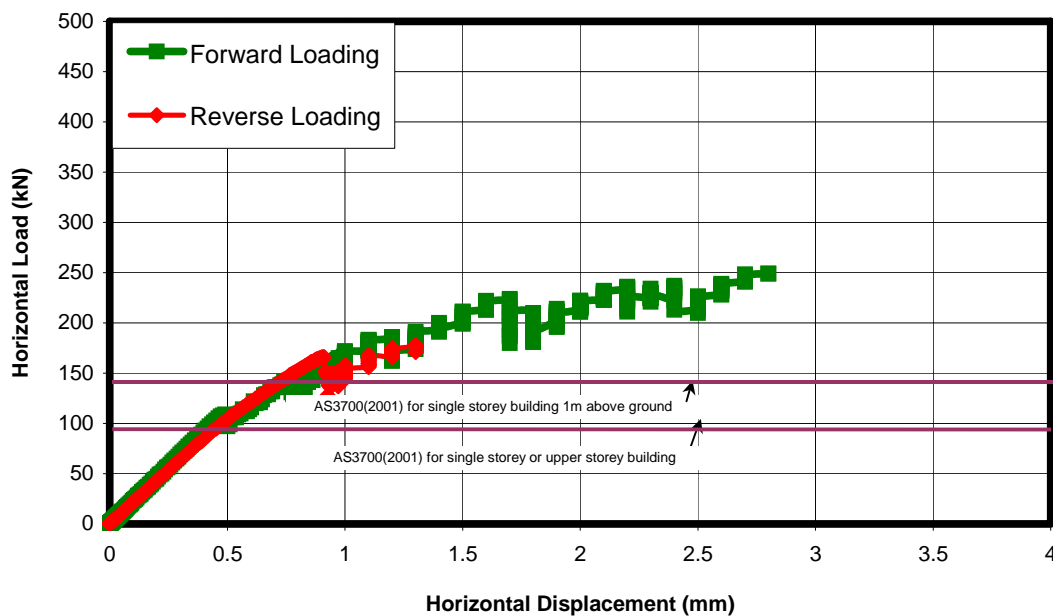


Figure 8.13: Load-displacement response of wall #16 (Average Masonry Properties)

It appears that the prescribed design of the masonry wall that restricts the width of the door opening could also be adequate for 3.2m wide door opening if masonry with average material parameters is adopted in the construction. Relaxing the provisions of the simplified designs for

small buildings in AS3700 (2001) is potentially possible and could allow for more design innovations and make masonry more attractive to designers.

8.5.1 Effect of Material Variability on Wall #16

Similar to wall #15, wall #16 was also analysed using stronger and weaker masonry material parameters provided in Table 8.1, and the load-displacement curves for the forward and reverse directions are presented in Fig. 8.14 and 8.15 respectively.

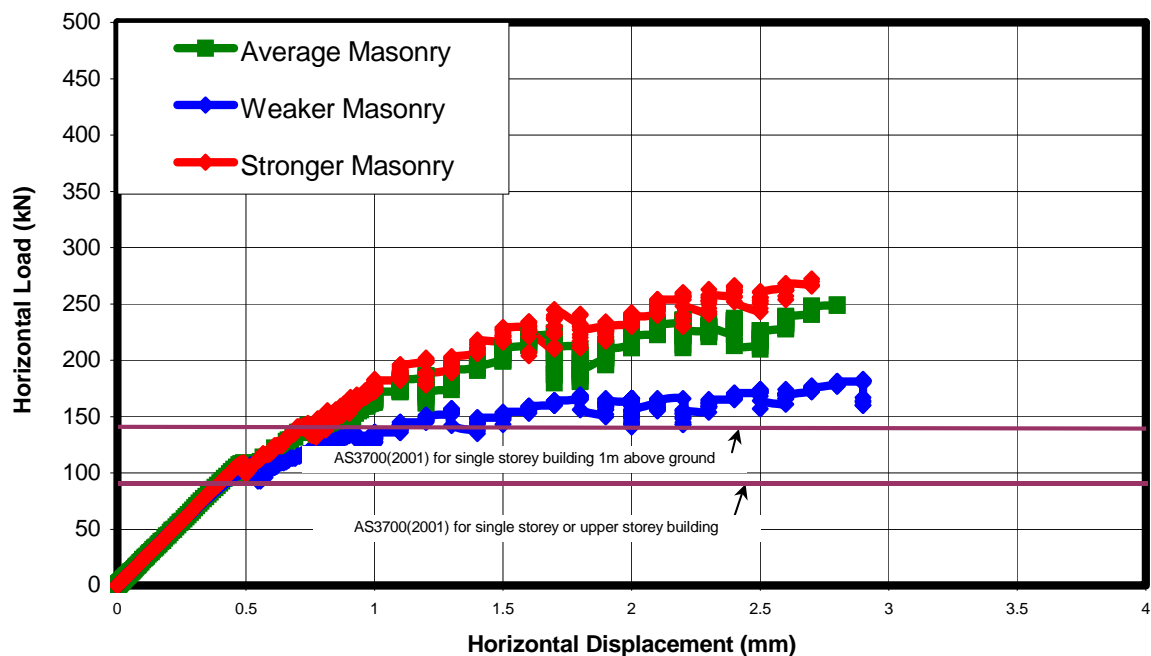


Figure 8.14 Load-displacement response of wall #16 for the forward direction loading

Fig 8.14 shows that the predicted shear capacity of wall #16 in the forward direction is 90%, 74%, and 21% higher than the AS3700 (2001) prescribed value of the shear capacity for wall #15 when it is constructed from stronger, average and weaker masonry respectively for a single storey building 1 m above the ground level. It appears that the limit on the width of door opening for the WSRM walls for small buildings could be increased.

Fig. 8.15 shows that the predicted shear capacity of wall #16 in the reverse direction is 52% and 22% higher than the AS3700 (2001) prescribed value of the shear capacity for wall #15 when it is constructed from stronger and average masonry respectively for a single storey building 1 m above the ground level. However, when this wall is constructed from weaker masonry and is 1m above ground level, its predicted shear capacity is lesser than the prescribed shear capacity.

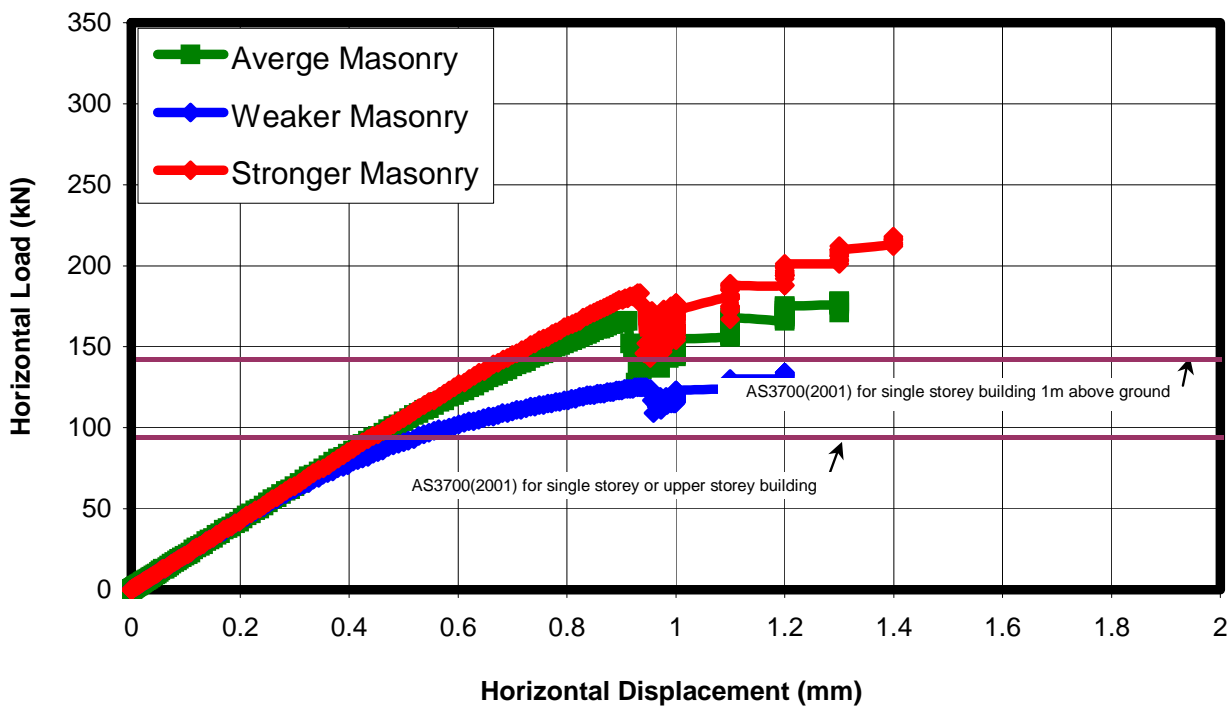


Figure 8.15 Load-displacement response of wall #16 for the reverse direction loading

Predicted shear capacity values for wall #16 in the reverse direction are lesser than those for the forward direction due to the smaller reinforced section of the wall on the load path for reverse direction loading. Therefore, a sufficiently wide masonry section at both ends of the shear walls (similar to the wall section at the forward loading location) appears to be efficient for the transfer of the horizontal force.

8.5.2 Out of Plane Bending Capacity of Wall #16

Out of plane bending capacity of reinforced masonry walls is calculated from Eq. 8.3 provided in AS3700 (2001).

$$M = \phi f_{sy} A_s d^* \left[1 - \frac{0.6 f_{sy} A_s}{1.3 f_m b d^*} \right] \quad (8.2)$$

For the calculation of out of plane bending capacity of wall #16, values of ' ϕ ', ' f_{sy} ', ' A_s ', ' b ', ' d^* ' and ' f_m ' were set equal to 0.75, 500MPa, 200mm², 200mm, 95mm and 18.0MPa respectively. The bending capacity of one of the critical vertical reinforced cores of this wall shown in Fig. 8.12 was calculated from Eq. 8.2 as 6.2kN-m. The corresponding distributed load for the 2.7m simply supported section of the core was equal to 6.8kN/m that corresponds to a design pressure of 3.1kPa for a 2.2m strip (half the width of door opening equal to 1.6m plus half the width of URM panel between two vertical reinforced cores equal to 0.6m) of the wall.

The maximum gust wind speed (V_z) as per AS4055 (2006) for an Australian wind category C2 region is 61m/sec. Maximum wind pressure (q_z) is calculated from Eq. 8.4 provided in AS1170.2 (1989).

$$q_z = 0.6 V_z^2 \times 10^{-3} \text{ (kPa)} \quad (8.3)$$

Maximum wind pressure for wall #16 calculated from Eq. 8.4 is 2.23kPa which is less than the out of plane capacity (3.1kPa) of the wall#16 calculated above.

The out of plane earthquake loading of the wall with wider door opening (reduced mass, higher acceleration) will only be lower than the wall with smaller opening; hence no calculations were made to check the out of plane earthquake load for this wall.

This calculation provides confidence that the out of plane action even for the wall with increased opening size is not critical, thus the inplane behaviour controls the load capacity.

8.6 Discussion

The load-displacement curves of walls #15 and #16 under forward loading and reverse loading using weaker masonry are presented in Fig. 8.16 and Fig. 8.17 respectively. For both walls (#15 and #16) design details were kept the same, and only the width of the door opening was varied. Fig. 8.16 shows that, using weaker masonry, the predicted shear capacity of walls #15 and #16 in the forward loading direction are 72% and 25% respectively higher than the prescribed values for a single storey building 1 m above the ground.

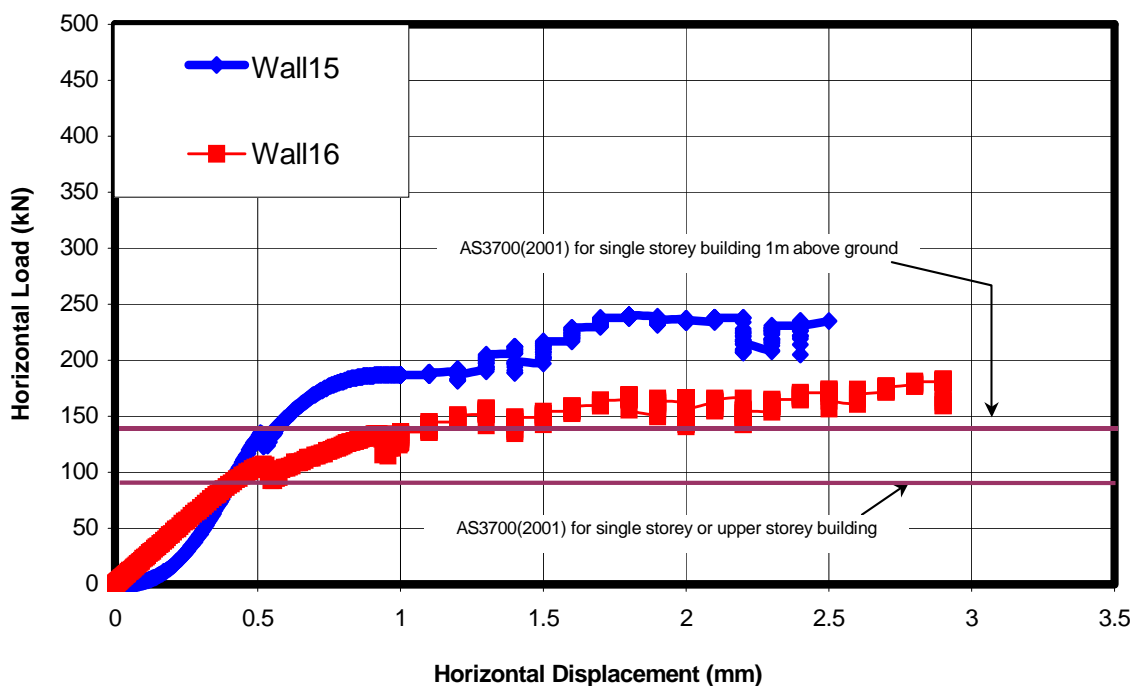


Figure 8.16: Response of walls #15 and #16 under forward loading (non-Critical)

Fig. 8.17 shows that, using weaker masonry, the predicted shear capacity of wall #15 in the forward direction is 25% higher than the prescribed values for a single storey building 1 m above the ground, whereas for wall #16, the predicted shear capacity is about 3% less than the

prescribed value; substantial cracking would also be expected. Therefore the code of practice could not recommend construction of highest masonry homes with increased opening size in the N4/C2 wind zones. However increased opening size still appears sensible for single or double storey buildings (refer to the curve in red relative to the lower most maroon line in Fig. 8.17).

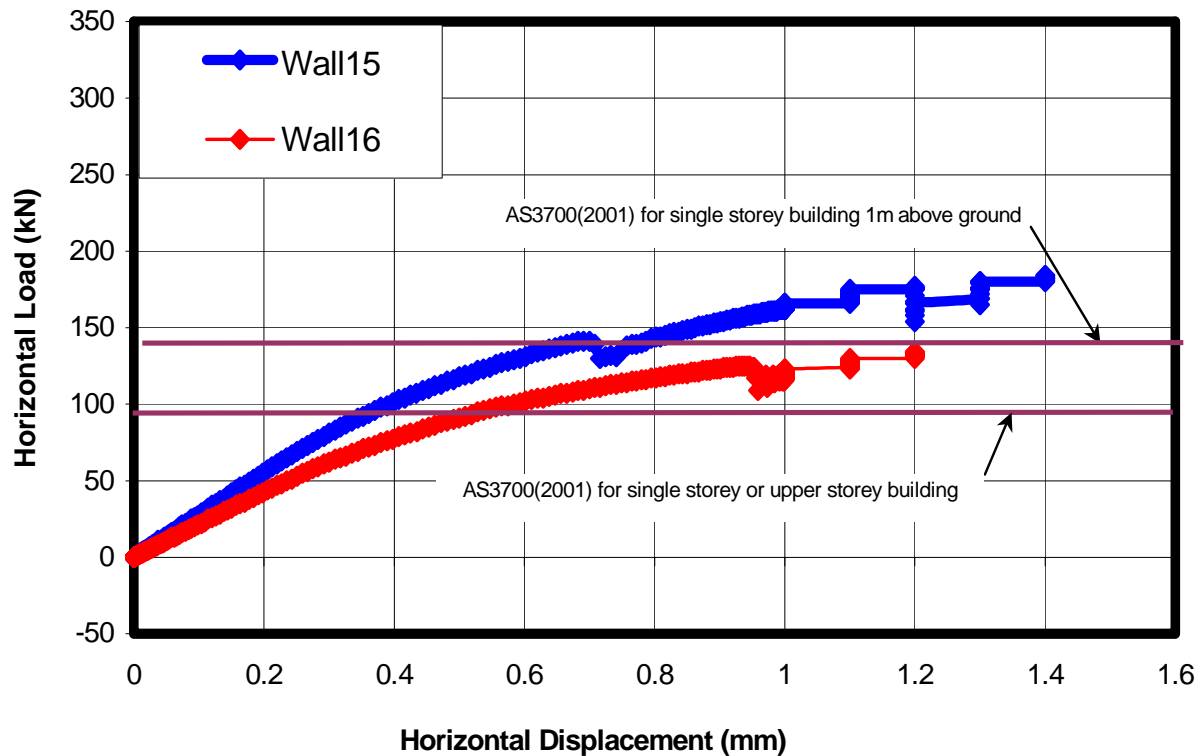


Figure 8.17: Response of walls #15 and #16 under reverse loading (Critical)

From the analyses of wall #15 and #16 using average, stronger and weaker masonry materials and variable door openings between the widely reinforced masonry sections, it appears that the limit on the width of door opening for the WSRM walls for a small building could be increased if:

- A sufficiently large reinforced masonry section is provided on the path of load flow; or
- Masonry with stronger or at least average material parameters is adopted.

8.7 Summary

The explicit algorithm based FE model developed in Chapter 6 for the analysis of the WSRM shear walls and verified in Chapter 7 has been used in this chapter for the analysis of masonry walls for small buildings prescribed in AS3700 (2001) for the Australian regions of different wind and earthquake categories. The FE model that was developed for WSRM walls without major openings has been used in this chapter for the analysis of masonry walls with large openings for doors and windows and with material variability.

The FE model has provided sensible predictions of the load flow, the stress and strain distributions and the modes of failure of WSRM walls of 11m length with 3m wide openings. The load-displacement responses of such walls for the elastic and the strain hardening regimes has been obtained from this model.

The effect of the width of the door opening and the width of the middle WSRM section of the wall has been investigated. It has been found that the WSRM section between the major openings resists the major proportion of the applied horizontal load. However, changing in the width of the WSRM section at the ends of the masonry walls by increasing the width of the door opening (1.8 to 3.2m wide) significantly affected the shear capacity as well as the mode of failure (crack pattern) of the walls. It has also been found that masonry walls containing major openings can resist the racking load quite effectively if a sufficiently wide section of the WSRM is provided between the major openings.

In addition to the change in the size of the door opening in the WSRM wall, the effect of the variability in the masonry material parameters has been examined in this chapter. It has been found that the shear capacity of the WSRM walls does vary with the material variation. It appears that the WSRM walls made from the clay blocks or concrete blocks or calcium silicate

blocks will have sufficient shear capacity if the materials are stronger or at least average and a sufficiently large reinforced masonry section is provided.

More research is recommended to comprehensively investigate the appropriateness of the provisions of the design code for effective design of the WSRM walls.

CHAPTER 9

SUMMARY AND CONCLUSIONS

The behaviour of WSRM walls subjected to inplane horizontal racking forces in the presence of low to high vertical stress has been investigated in this thesis. Firstly, the elastic response of the WSRM shear walls has been examined using a standard ABAQUS finite element code using micro modelling technique, and several hypotheses have been developed based on the results. Secondly, ten full scale shear walls (2870mm long×2408mm high; aspect ratio 0.84 and subjected to vertical stress of 0.5MPa) were constructed and tested to understand the elastic, cracking, nonlinear hardening and post-peak behaviour of the WSRM shear walls. Thirdly, a finite element model based on explicit solution algorithm that incorporates macro material model for masonry has been developed to study the nonlinear response of the WSRM shear walls. The explicit algorithm has enabled the finite element model to provide solutions of nonlinear response of the WSRM walls in 15 minutes on average using an ordinary PC in contrast to the conventional implicit algorithms that typically take several hours to provide solutions to problems of the same size. Fourthly, the FE model has been validated from the results of additional experiments, which consisted of four WSRM walls of two different aspect ratios (0.50 and 1.11) and subjected to two different vertical stresses (0 MPa and 0.25MPa). Finally, the FE model was also applied to examine the appropriateness of the design prescriptions in AS3700 (2001) for the design of WSRM shear walls with door and window openings suitable for small buildings for the Australian regions of different wind and earthquake categories.

In the first part, potential failure modes and stress distribution affected by the presence of vertical grouted cores have been inferred from the elastic analyses using the FE micro modelling strategies.

In the second phase of the study ten walls of 2.9m width, 2.4m height and 150mm thickness were constructed and tested; four were tested under cyclic loading and six under monotonic loading. From the analysis of the experimental data, six of the ten walls have been classified as WSRM walls and the remaining four have been classified as Non-WSRM walls consistent with the provisions on definition of WSRM walls in AS3700 (2001). Shear capacities of the WSRM and Non-WSRM walls determined from the experiments have been compared with those of the corresponding walls determined from the equations available in AS3700 (2001) and in the literature. In addition to the shear capacity, the ductility, the stiffness degradation, the structural response factor and the damage in critical regions of the walls have been investigated from experiments.

The third phase of the study has involved the development of an explicit FE model for which a user subroutine (VUMAT) for macro material modelling of URM available in the literature has primarily been used. The VUMAT subroutine improved the capability of the ABAQUS/Explicit (2005) to model the masonry shear walls that was otherwise not possible. The reinforced grouted cores were modelled using the damaged plasticity concrete material model and REBAR option available in ABAQUS (2005) in conjunction with the VUMAT where the compressive response of the reinforcement bars have been disabled to represent the absence of lateral reinforcement in typical masonry constructions.

The fourth phase of the study has involved experiments on four shear walls of which two walls were 2.9m wide \times 1.4m high and the other two walls were 1.3m wide \times 1.4m high. During this phase of experiments, all the four walls were tested under monotonic loading since the effect of

loading history (monotonic/ cyclic) was found to be insignificant from the first phase of experiments.

The fifth and final phase of the study has involved the application of the FE model to examine the appropriateness of design prescriptions of WSRM walls in AS3700 (2001). One of the design prescriptions that could be applied to either a single storey or high-set building in Australian wind category N4, C2 and earthquake category H1, H2, H3 was examined for its shear wall response.

Results obtained from the experimental and nonlinear FE studies lead to the following major conclusions:

- 1: Two groups of masonry shear walls, namely WSRM and Non-WSRM have emerged based on the results for horizontal load capacity, displacement ductility factors, stiffness values and damage characteristics. This grouping was consistent with the definition for the classification of the WSRM walls provided in AS3700 (2001).
- 2: The developed explicit FE model has successfully predicted the nonlinear behaviour of the WSRM as well as the Non-WSRM walls. Load flow, mode of failure and the states of stresses and strains at different stages of the analysis have been very well exhibited by the FE model.
- 3: The crack pattern inferred from the vector plot of logarithmic strains and principal stresses obtained from the FE model has shown a good match with the crack pattern of the WSRM walls obtained from the experiments.
- 4: For all the walls, the two load-displacement curves (FE and experimental) have shown an overall good match although some discrepancy in the early stages of loading was evident due to the orthotropic brittle nature of masonry and the workmanship effects.

- 5: Prediction of the softening part of the load-displacement curve from the FE model has made it possible to calculate the ductility factor as well as the structural response factor used by the designers of masonry structures.
- 6: The FE model has also provided sensible predictions of the load flow, the stress and strain distributions and the modes of failure of WSRM walls of 11m length containing two 3m wide openings.
- 7: From the experiments it has been found that the shear capacity of the WSRM walls was greatly affected by the aspect ratio and marginally by the variation in the vertical stress. Sensitivity analyses of the WSRM walls using the FE model also exhibited the same effects.
- 8: The average experimental values of the normalised horizontal load for the WSRM walls at the peak and the ultimate load stages was 34% higher than that for the Non-WSRM walls.
- 9: Ductility factor of the WSRM walls was 29% higher than that for the Non-WSRM walls.
- 10: Masonry walls containing major openings can resist the racking load quite effectively if a sufficiently wide section of WSRM is provided between the major openings.
- 11: WSRM section between the major openings resists the major proportion of the applied horizontal load. However, change in the width of the WSRM section at the ends of the masonry walls also affects the shear capacity as well as the mode of failure of the walls.
- 12: Structural change (size of door openings) affect the structural behaviour of the WSRM walls more than by the variability in the masonry material parameters.

- 13: The equation available in the Australian Standard for masonry structures AS3700 (clause 8.6.2) has over predicted the shear capacity of the WSRM walls on average by 30%. The FE model over-predicts the shear capacity of the corresponding walls on average by only 3.1%.
- 14: Application of the capacity reduction factor (0.75) to the shear capacities predicted by the FE model would result in safe shear capacity estimation of WSRM walls whereas the equation available in AS3700 (2001) will remain non-conservative even after including the capacity reduction factor of 0.75 in the calculation.
- 15: For WSRM and Non-WSRM walls of aspect ratio 0.84 the major crack passed through the loaded diagonal of the walls; for walls of aspect ratio 0.50 the major crack was not truly diagonal rather it was horizontal between the two intermediate vertical grouted cores and inclined at the two ends of the walls; for walls of aspect ratio 1.11 the major crack was below the loaded diagonal of the walls.
- 16: Elastic analyses showed that the shear stress dominated the diagonal region of the walls irrespective of the presence of vertical grouted cores in the walls of aspect ratio 0.84.
- 17: Elastic analyses showed that the grouted sections introduced discontinuity to the shear flow, however, it was inferred that the discontinuity did not modify the potential diagonal failure planes.

Results obtained from the present study lead to the following specific conclusions:

- 1: One major crack appeared along the loaded diagonal of the WSRM shear walls during forward loading of both the monotonic as well as cyclic loading histories irrespective of the presence of the reinforced grouted cores. A second crack along the opposite diagonal appeared when the direction of loading was reversed.

- 2: The diagonal cracks closed and opened with the increment of horizontal displacement applied at the bond beam level in the forward and reverse direction during cyclic loading, whereas one diagonal crack appeared during forward monotonic loading and a second crack appeared along the opposite diagonal when the direction of monotonic loading was reversed.
- 4: In the URM wall, higher toe and heel deformations were found than those in WSRM walls. This was due to lack of grouted cores at the ends of the URM wall.
- 5: Average stiffness values of the WSRM walls at the yield, the peak and the ultimate load stage were 55%, 53% and 40% higher respectively than that for the Non-WSRM walls.
- 7: The URM wall exhibited rocking type of failure that did not happen for the WSRM and the other Non-WSRM walls due to presence of vertical reinforced cores at the ends.

Recommendations:

- (i) Maximum horizontal spacing (2000mm) between the vertical reinforced cores of the WSRM walls should be retained as it has been verified by the experimental and FE studies of these walls in this thesis.
- (ii) The equation provided in clause 8.6.2 of AS3700 (2001) for WSRM walls is highly non-conservative and over predicts their shear capacities; hence this equation requires urgent critical review.
- (iii) For effective designs of WSRM walls suitable for small buildings and provided in AS3700 (2001), more research is required. Restrictions on the maximum width of the door and window openings in these prescriptions may be relaxed.

-
- (iv) Although the FE model has successfully predicted all characteristics of the WSRM and Non-WSRM shear walls yet it is strongly recommended that a comprehensive research program on the fracture energy, strain localisation and characteristic length of the URM be conducted.

 - (v) The explicit FE algorithm incorporating the macro masonry material model, the damaged plasticity concrete model and the compression-disabled reinforcement bar model could be used as an effective numerical technique for the future analysis of WSRM shear walls of practical relevance.

REFERENCES

- ABAQUS (2005). "Theory Manual", Hibbit, Karlson & Sorenson, Inc
- Alcocer, S. M. and Meli, R. (1995). "Test program on the seismic behaviour of confined masonry structures." TMS Journal Vol.13(2): pp.68-76.
- Ali, S. and Page, A. W. (1986). "A failure criterion for mortar joints in brick masonry subjected to shear and tension." Masonry International Vol.6: pp.9-21.
- Ali, S. and Page, A. W. (1988). "Finite element model for masonry subjected to concentrated loads." Journal of Structural Engineering, ASCE Vol.114(8): pp.1761-1783.
- AS1170.2 (1989). "Minimum design loads on structures - Wind Loads." Standards Australia International.
- AS1170.4 (1993). "Australian Standards - Earthquake loads." Standards Australia International.
- AS2699 (2002). "Australian Standards for durability of structures -Built in components for masonry construction (Durability Requirements)." Standards Australia International.
- AS2701.4 (1984). "Australian Standards for determining the compressive strength of mortar." Standards Australia International.
- AS3600 (2000). "Australian Standards - Concrete Structures." Standards Australia International.
- AS3700 (2001). "Australian Standards for Masonry Structures." Standards Australia International.
- AS4055 (2006). "Australian Standards - Wind Loads for Housing." Standards Australia International.
- AS4100 (1998). "Australian Standards for Steel Structures" Standards Australia International.
- AS4456.3 (2003). "Australian Standards for determining the compressive strength of masonry units." Standards Australia International.
- Assa, B. and Dhanasekar, M. (2000). "A layered line element for the flexural analysis of cyclically loaded reinforced concrete beam-columns." Computers and Structures Vol.78: pp.517-527.
- ASTM (1989). "American Society for Testing and Materials standards for mortar mix."
- Backes, H. P. (1985). "The behaviour of masonry under tension in the direction of the bed joints (in German)." PhD Dissertation, Aachen University of Technology, Aachen, Germany.
- Benli, G. and Houqin, Z. (1991). "The seismic resistance of behaviour of partially reinforced brick walls". Proceedings of the 9th International Brick/Block Masonry Conference, Berlin, Germany, October. pp.481-489

- Bernardini, A., Lazzaro, G. and Valluzzi, M. R. (1997). "Cyclic behaviour and modelling of reinforced masonry panels". 11th International Brick/Block Masonry Conference, Shanghai, China, October 14-16. pp.40-49
- Bosiljkov, V., Page, A. W., Bosiljkov, V. B. and Zarnic, R. (2003). "Performance based studies of inplane loaded unreinforced masonry walls." *Masonry International* Vol.16(2): pp.39-50.
- Boult, B. F. (1979). "Concrete masonry prism testing." *ACI Journal* Vol.76-24: pp.513-535.
- Brunner, J. D. and Shing, P. B. (1996). "Shear strength of reinforced masonry walls." *TMS Journal* Vol.14(1): pp.65-77.
- BS5628 (1992), "British Standard for Unreinforced Masonry, Part 1 of Masonry Code"
- Cheema, T. S. and Klingner, R. E. (1986). "Compressive strength of concrete masonry prisms." *ACI Journal* Vol.83-11: pp.88-97.
- Correa, M. R. and Page, A. W. (2001). The interaction of load bearing masonry walls subjected to vertical loads section3. Research Report No. 218.12.2001. Department of Civil, Surveying and Environmental Engineering, University of Newcastle Australia. pp.19-58
- Cruz-Diaz, J. I., Selier, A., Capra, B., Delmotte, P., Phillippe, R. and Ahamed, M. (2002). "Resistance of masonry infill walls to racking loads- Simplified model and experimental validation." *Masonry International* Vol.15(3).
- CSAS304.1 (1994). "Limit State Design for Masonry Buildings." Canadian Standards Association, Canada.
- Davidson, B. J. and Brammer, D. R. (1996). "Cyclic performance of nominally reinforced masonry walls". NZNSEE Conference, New Plymouth, New Zealand, March 22-24. pp.144-151
- Dhanasekar, M. (1985). "The performance of brick masonry subjected to inplane loading." PhD thesis, University of Newcastle, Australia.
- Dhanasekar, M., Kleeman, P. W. and Page, A. W. (1985a). "Biaxial stress -strain relations for brick masonry." *Journal of Structural Engineering, ASCE* Vol.111(5): pp.1085-1100.
- Dhanasekar, M., Loov, R. E. and Shrive, N. G. (1997). "Stress-strain relations for grouted concrete masonry under cyclic compression". Proceedings of the 15th Australasian conference on the Mechanics of Structures and Materials, Melbourne Australia, December 8-10. pp.663-668
- Dhanasekar, M. and Page, A. W. (1987). "The influence of brick masonry infill properties on the behaviour of infilled frames." Proceedings of the Institution of Civil Engineers, Part 2(Paper 9061): pp.593-605.
- Dhanasekar, M., Page, A. W. and Kleeman, P. W. (1985b). "The failure of brick masonry under biaxial stress." Proceedings of the Institution of Civil Engineers Part 2(79): pp.295-313.

- Dhanasekar, M. and Xiao, Q. Z. (2001). "Plane hybrid stress element method for 3D hollow bodies of uniform thickness." *Computers and Structures* Vol.79: pp.483-497.
- Drysdale, R. G. and Gazzola, E. A. (1991). "Strength and deformation properties of grouted, dry stacked, interlocking concrete block system". 9th International Brick/Block Masonry Conference, Berlin, Germany. pp.164-171
- Drysdale, R. G. and Hamid, A. A. (1979a). "Behaviour of concrete block masonry under axial compression." *ACI Journal - Technical Paper*(76-32): pp.707-721.
- Drysdale, R. G. and Hamid, A. A. (1983). "Capacity of concrete block masonry prisms under eccentric compressive loading." *ACI Journal*: pp.102-109.
- Drysdale, R. G., Hamid, A. A. and Baker, L. R. (1993). *Masonry Structures: Behaviour and design*. Inglewood, Cliffs, NJ, Prentice Hall Inc.
- Drysdale, R. G., Hamid, A. A. and Heidebrecht, A. C. (1979b). "Tensile strength of concrete masonry." *Journal of Structural Division, ASCE* Vol.105(ST7): pp.1261-1276.
- ENV-1996-1-1 (1995). "Euro code for Masonry structures."
- Faella, G., Manfredi, G. and Realfonzo, R. (1994). Cyclic shear behaviour of tuff masonry walls strengthened by grout injections and reinforcement. 10th International Brick/Block Masonry conference, Calgary, Canada. pp.239-248
- Fattal, S. G. (1993a). "The effect of critical parameters on the behaviour of partially grouted masonry shear walls under lateral loads." National Institute of Standards and Technology, Gaithersburg MD (NISTIR 5116).
- Fattal, S. G. (1993b). "Strength of partially grouted shear walls under lateral loads." U. S. Department of commerce, NISTIR 5147, National Institute of Standards and Technology, Gaithersburg, MD.
- Fattal, S. G. and Todd, D. R. (1993). "Ultimate strength of masonry shear walls: Predictions versus test results." U. S. Department of commerce, NISTIR 5147, National institute of standards and technology, Gaithersburg, MD.
- Feenstra, P. H. and Borst, R. D. (1995). "A plasticity model and algorithm for mode 1 cracking in concrete." *International Journal for Numerical Methods in Engineering* Vol.38: pp.2509-2529.
- Frunzio, G., Mallardo, V. and Monaco, M. (1995). Reliability of diagonal test. 7th Canadian Masonry Symposium, June 4-7
- Ganz, H. R. and Thurlimann, B. (1982). "Tests on the biaxial strength of masonry (in German)." Report No. 7502-3, Institute of Structural Engineering, ETH Zurich, Switzerland.
- Ghanem, G. M., E., S. A., Elmagd, S. A. and Hamid, A. A. (1993). Effect of axial compression on the behaviour of partially reinforced masonry shear walls. 6th North American Masonry Conference, June 6-9

- Ghosh, A. K., Amde, A. M. and Colville, J. (1994). Finite element modelling of unreinforced masonry. 10th International Brick/Block Masonry conference, Calgary, Canada, July 5-7. pp.61-69
- Haider, W. and Dhanasekar, M. (2004). "Experimental study of monotonically loaded wide spaced reinforced masonry shear walls." Australian Journal of Structural Engineering Vol.5(2): pp.101-118.
- Hamid, A. A. (1991). "Partially reinforced concrete masonry". 9th International Brick/Block Masonry conference, Berlin, Germany. pp.368-378
- Hamid, A. A. (1997). "Material model for concrete and clay masonry: A comparative study." TMS Journal Vol.15(1): pp.21-26.
- Hamid, A. A. and Drysdale, R. G. (1981). "Proposed failure criteria for concrete block masonry under biaxial stresses." Journal of Structural Division, ASCE Vol.107(ST8): pp.1675-1687.
- Hamid, A. A., Drysdale, R. G. and Heidebrecht, A. C. (1978). "Shear strength of concrete masonry joints." Journal of Structural Division, ASCE Vol.105(ST7): pp.1227-1240.
- Hansen, K. F., Nykanen, E. and Gottfredsen, F. R. (1998). "Shear behaviour of bed joints at different levels of precompression." Masonry International Vol.12(2): pp.70-78.
- Hendry, A. W. (1978). "A note on the strength of brickwork in combined racking shear and compression". Proceedings of the British Ceramic Society. pp.47-52
- Hossain, M. M., Ali, S. and Rahman, M. A. (1997). "Elastic finite element study of composite action between brick wall and supporting beam." Masonry International Vol.11(1).
- Ibrahim, K. S. and Suter, G. T. (1994). Smear crack model for reinforced concrete masonry shear wall analysis. Proceedings of the 10th International Brick/Block Masonry Conference, Calgary, Canada, July 5-7. pp.731-740
- Ingham, J. M., Davidson, B. J., Brammer, D. R. and Voon, K. C. (2001). "Testing and codification of partially grout filled nominally reinforced concrete masonry subjected to inplane cyclic loads." TMS Journal: pp.83-96.
- Jager, W. and Schops, P. (2004). Numerical modeling of masonry under shear loading. 13th International Brick and Block masonry conference, Amsterdam, July 4-7. pp.1-10
- Jiang, D. H. and Xiao, X. S. (1994). "A new masonry shear test method determining shear strength". Proceedings of the 10th International Brick/Block Masonry Conference, Calgary, Canada. pp.1013-1019
- Jihang, F., Bolong, Z., Dezheng, Z. and Yan, W. (1997). "A study on ductility and energy dissipation of reinforced concrete - concrete masonry composite shear walls". 11th International Brick/Block Masonry Conference, Tongji university, Shanghai, China, October 14-16
- Jukes, P. and Riddington, J. R. (1997). "A review of masonry joint shear strength test methods." TMS Journal Vol.11(2): pp.37-43.

- Khalaf, F. M. and Naysmith, M. W. (1997). "Shear strength of masonry bed joints." TMS Journal Vol.15(2): pp.13-22.
- Khatab, M. M. and Drysdale, R. G. (1993). "The effect of reinforcement on the shear response of grouted concrete masonry." TMS Journal Vol.12(1): pp.38-44.
- Khatab, M. M. and Drysdale, R. G. (1994). "Nonlinear modelling of the shear response of grouted and reinforced concrete masonry". 10th International Brick/Block Masonry Conference, Calgary, Canada. pp.1047-1056
- Knuttsen, H. H. and Nielsen, J. (1995). "On the modulus of elasticity for masonry." Masonry International Vol.9(2).
- Kornbak, D. L. (2000). "Mohr-Coulomb approach to the ductility of masonry and optimum unit/block configuration." Masonry International Vol.14(1): pp.18-27.
- Kozar, I. and Bicanic, N. (1999). Softening materials: An engineering approach. IC on Fracture and Damage, London, July 27-29
- Kumar, M. (1995). "Development of reinforced clay block masonry subjected to concentric and eccentric compression." Master Thesis, Central Queensland University, Australia.
- LabVIEW (2004). "National Instruments: 11500 N, Mopac Expressway, Austin Texas."
- Lafuente, M., Castilla, E. and Ganatios, C. (1998). "Experimental and analytical evaluation of the seismic resistant behaviour of masonry walls." Masonry International Vol.11(3).
- Lotfi, H. R. and Shing, P. B. (1991). "An appraisal of smeared crack models for masonry shear wall analysis." Computers and Structures Vol.41(3): pp.413-425.
- Lotfi, H. R. and Shing, P. B. (1994). "Interface model applied to fracture of masonry structures." Journal of Structural Engineering, ASCE Vol.120(1): pp.63-80.
- Lourenco, P. B. (1996). Computational strategies for masonry structures. PhD thesis, Delft University, Netherlands
- Lourenco, P. B., Borst, R. D. and Rots, J. G. (1997). "A plane stress softening plasticity model for orthotropic materials." International Journal for Numerical Methods in Engineering Vol.40: pp.4033-4057.
- Lourenco, P. B. and Rots, J. G. (1997). "Multisurface interface model for analysis of masonry structures." Journal of Engineering Mechanics Vol.123(7): pp.660-668.
- Lublinter, J. J., Oliver, S., and Onate, E. (1989). "A plastic damage model for concrete", International Journal of Solids and Structures, Vol. 25: pp. 299-329.
- Mahmoud, A. D. S., Hamid, A. A. and Magd, A. E. (1995). "Lateral response of unreinforced masonry shear walls". 7th Canadian Masonry Symposium, McMaster University, Hamilton, Ontario, Canada. pp.110-125

- Maleki, M., El-Damatty, A. A., Hamid, A. A. and Drysdale, R. G. (2005). "Finite element analysis of reinforced masonry shear walls using smeared crack model". Proceedings of the 10th Canadian Masonry Symposium, Banff, Alberta, June 8-12
- Matsumura, A. (1987). "Shear strength of reinforced hollow unit masonry walls". 4th North American Masonry Conference, Los Angeles, CA. pp.50.1-50.16
- Matsumura, A. (1988). Shear strength of reinforced masonry walls. 9th World Conference on Earthquake Engineering, Tokyo-Kyoto, Japan, August 2-9. pp.VI 121-VI 126
- Matsumura, A. (1990). Planar shear loading test on reinforced fully grouted hollow clay masonry walls. Proceeding of the 5th North American Masonry Conference, University of Illinois, Urbana-Champaign. pp.347-358
- Mehrabi, A. B. and Shing, P. B. (1997). "Finite element modelling of masonry infilled RC frames." *Journal of Structural Engineering* Vol.125(5): pp.604-613.
- Mehrabi, A. B., Shing, P. B., Schuller, M. and Noland, J. L. (1994). "Performance of masonry infilled R.C. frames under inplane lateral loads." *Structural Engineering and Structural Mechanics Research Series*, Department of Civil Engineering and Architecture Engineering, University of Colorado, Boulder.
- Middleton, J., Pande, G., N., Liang, J. X. and Kralj, B. (1991). "Some recent advances in computer methods in structural masonry". Proceedings of International Symposium on Computer Methods in Structural Masonry, Holiday Inn, Swansea, UK, 3-5 April. pp.1-21
- Muguruma, H., Nishiyama, M., Watanabe, F. and Tnaka, H. (1991). "Ductile behaviour of high strength concrete columns confined by high strength transverse reinforcement." *ACI Special Publication: Evaluation and Rehabilitation of concrete structures and innovation in design* Vol.128-54(88-AB).
- Mullins, P. J. and O'Connor, C. (1994). "The capacity of unreinforced unbonded brick shear walls". 10th International Brick/Block Masonry Conference, Calgary, Canada, 5-7 July. pp.1037-1046
- Naom, N. F. (1992). "Prediction of masonry ultimate compressive strength." M-Phill Thesis, University of Sussex.
- Naraine, K. and Sinha, S. (1989). "Behaviour of brick masonry under cyclic compressive loading." *Journal of Construction Engineering and Management* Vol.115(2): pp.1432-1445.
- Naraine, K. and Sinha, S. (1992). "Stress-strain curves for brick masonry in biaxial compression." *Journal of Structural Engineering* Vol.118(6): pp.1451-1461.
- NEHRP (1994). "Recommended provisions for the development of seismic regulations for new buildings,." Part 1, Provisions, Federal Emergency Management Agency, Proposed Revisions to 1994 Edition.
- Okamoto, S., Yamazaki, Y., JKaminosono, T., Teshigawara, M. and H., H. (1987). "Seismic capacity of reinforced masonry walls and beams in wind and seismic effects".

- Proceedings of the 18th Joint Meeting, US-Japan Panel on Wind and Seismic Effects, Raufaste, NJ.
- Page, A. W. (1978). "Finite element model for masonry." *Journal of Structural Division, ASCE* Vol.104(ST8): pp.1267-1285.
- Page, A. W. (1981). "The biaxial compressive strength of brick masonry." *Proc. Intsn. Civ. Engrs. Vol.Part 2(71)*: pp.893-906.
- Page, A. W. (1982). An experimental investigation of the biaxial strength of brick masonry. 6th International Brick Masonry conference, Rome, Italy. pp.3-15
- Page, A. W. (1983). "The strength of brick masonry under biaxial compression-tension." *International Journal of Masonry Construction* Vol.3(1): pp.26-31.
- Pande, G., N., Liang, J. X. and Middleton, J. (1990). "Equivalent elastic moduli for brick masonry." *Computers and Geotechnics* Vol.8: pp.243-265.
- Papa, E. (2001). Damage and failure models. Computational modelling of masonry brickwork and blockwork structures, Saxe-Coburg publications, Stirling, Scotland. pp.1-26
- Park, R. and Paulay, T. (1975). Reinforced concrete structures, John Wiley & Sons, New York
- Paulay, T. and Priestley, M. J. N. (1992). "Seismic design of reinforced concrete and masonry buildings", John Wiley & Sons, NY
- Pilakoutas, K. and Elnashai, A. (1995). "Cyclic behaviour of reinforced concrete cantilever walls, Part1: Experimental results." *ACI Structural Journal* Vol.92(3): pp.271-281.
- Priestley, M. J. N. (1977). "Seismic resistance of reinforced concrete masonry shear walls with high steel percentages." *Bulletin of the New Zealand National Society of Earthquake Engineering* Vol.10(1): pp.1-6.
- Priestley, M. J. N. and Elder, D. M. (1982). "Cyclic loading tests of slender concrete masonry shear walls." *Bulletin, New Zealand National Society of Earthquake Engineering* Vol.15(1): pp.3-21.
- Priestley, M. J. N. and Elder, D. M. (1983). "Stress-strain curves for unconfined and confined masonry." *ACI Journal* Vol.80(3): pp.192-201.
- Riddington, J. R. and Naom, N. F. (1994). "Finite element prediction of masonry compressive strength." *Computers and Structures* Vol.113-119.
- Rots, J. G. (1988). Computational Modelling of Concrete Fracture, PhD Thesis, Delft University of Technology, Delft, The Netherlands
- Saadeghvaziri, M. A. and Mehta, S. (1993). "An analytical model for URM structures." The 6th North American Masonry conference, Philadelphia, Pennsylvania: pp.409-418.
- Saatcioglu, M. (1991). "Modelling of hysteretic force-deformation relationship of reinforced concrete elements." *ACI Special Publication* Vol.127(5): pp.153-198.

- Samarasinghe, W., Page, A. W. and Hendry, A. W. (1981). "Behaviour of masonry shear walls." *The Structural Engineer* Vol.59B(3): pp.42-48.
- Sayed-Ahmed, E. Y. and Shrive, N. G. (1995). "Numerical analysis of face shell bedded hollow masonry walls subject to concentrated loads." *Canadian Journal of Civil Engineering* Vol.22(4): pp.802-819.
- Schultz, A. E. (1994). "NIST Research program on the seismic resistance of partially grouted masonry shear walls." Building and Fire Research Laboratory, National Institute of Standards and Technology, Gaithersburg, MD20899, NISTIR 5481.
- Scrivener, J. C. and Baker, L. R. (1988). "Factors influencing the grout masonry prism compressive strength". 8th International Brick/Block Masonry Conference, Dublin. pp.874-883
- Seah, C. K. and Dawe, J. L. (1997). "Elastic-plastic analysis of masonry infilled frames". 11th International Brick/Block Masonry Conference, Tongji University, Shanghai, China, 14-16 October. pp.1260-1268
- Seim, W. (1994). Isotropic or anisotropic Simulation of inplane loaded masonry structures close to reality. 10th International Brick/Block Masonry Conference, Calgary, Canada, July 5-7. pp.77-86
- Shing, P. B., Brunner, J. D. and Lotfi, H. R. (1993a). "Evaluation of shear strength of reinforced masonry walls." *TMS Journal* Vol.2(1): pp.61-75.
- Shing, P. B., Brunner, J. D. and Lotfi, H. R. (1993b). "Analysis of shear strength of reinforced masonry walls". Proceedings of the 6th North American Masonry conference. pp.1133-1144
- Shing, P. B. and Cao, L. (1997). "Analysis of partially grouted masonry shear walls." U. S. Department of Commerce, National Institute of Standards and Technology, Gaithersburg, MD, NISTIR GCR 97-710.
- Shing, P. B., Noland, J. L., Spaeh, H. P., Klamerus, E. W. and Schuller, M. (1991). "Response of single story reinforced masonry shear walls to inplane lateral loads, US-Japan Coordinated Program for Masonry Buildings Research, Report No. 3.1(a)-2."
- Shing, P. B., Schuller, M. and Hoskere, V. S. (1990a). "Inplane resistance of reinforced masonry shear walls." *Journal of Structural Engineering*, ASCE Vol.87116(3): pp.619-640.
- Shing, P. B., Schuller, M. and Hoskere, V. S. (1990b). "Strength and ductility of reinforced masonry shear walls". 5th North American Masonry conference, University of Illinois Urbana-Champaign, June 3-6. pp.309-321
- Sio, W. B. (1994). "Shear strength of short reinforced concrete walls, corbels and deep beams." *ACI Structural Journal* Vol.91(2): pp.123-132.
- Smith, S. and Carter, C. (1971). "Hypothesis for shear failure of brickwork." *Journal of Structural Division*, ASCE Vol.97(ST4): pp.1055-1062.

- Soroushian, P., Obaseki, K. and Choi, K. B. (1988). "Nonlinear analysis and seismic analysis of masonry shear walls." *Journal of Structural Engineering*, ASCE Vol.114(3): pp.1106-1119.
- Tanuwidjaja, H. R. and Dhanasekar, M. (1998). "Review of the reinforced concrete masonry shear walls subjected to cyclic loading". 5th Australasian Masonry Conference, Gladstone, Queensland, Australia. pp.375-386
- Tomazevic, M., Lutman, M. and Petkovic, L. (1996). "Seismic behaviour of masonry walls: Experimental simulation." *Journal of Structural Engineering*, ASCE Vol.122(9): pp.1040-1047.
- Toscan, M. M. (2001). "Inplane behaviour of partially reinforced masonry shear walls." Thesis, University of Newcastle, Australia.
- UBC (1988). "Uniform Building Code." International Conference of Building Officials, Whittier, Calif, South Workman Mill Road, Whittier 90601.
- Usami, T., Aoki, T., Mizutani, S. and Itoh, Y. (1991). "Steel and concrete filled steel compression members under cyclic loading". US-Japan Joint Seminar on Stability and Ductility of Steel Structures under Cyclic Loading, Osaka, Japan, July 1-3. pp.123-138
- Van der Pluijm, R. (1992). "Material properties of masonry and its components under tension and shear." *Proceedings of the Sixth Canadian Masonry Symposium*, Saskatoon, Canada.
- Van der Pluijm, R. (1993). "Shear behaviour of bed joints". 6th North American Masonry Conference, Philadelphia, Pennsylvania, June 6-9. pp.125-136
- Vermeltfoort, A. T., Raijmakers, T. M. J. and Janssen, H. J., M (1993). Shear tests on masonry walls. The 6th North American Masonry conference, Philadelphia, Pennsylvania. pp.1183-1193
- Warner, R. F., Rangan, B. V. and Hall, A. S. (1999). *Concrete Structures*, Addison Wesley, Australia, Pty, Ltd. 752-780
- Yancey, C. W. C., Fattal, S. G. and Dikkers, R. D. (1990). "Review of technical literature on masonry shear walls." U. S. Department of Commerce, National Institute of Standards and Technology, Gaitherburg, MD, Report No. 90-4512.
- Yokel, F. Y. and Fattal, S. G. (1976). "Failure hypothesis for masonry shear walls." *Journal of Structural Division*, ASCE Vol.102(ST3): pp.515-532.
- Zhuge, Y. (1995). "Nonlinear dynamic response of unreinforced masonry under inplane lateral loads." PhD Thesis, Queensland University of Technology, Australia.
- Zhuge, Y., Corderoy, J. and Thambiratnum, D. (1996). "Behaviour of unreinforced brick masonry under lateral cyclic loading." *TMS Journal* Vol.14(2): pp.55-62.
- Zhuge, Y. and Thambiratnum, D. (1998). "Nonlinear dynamic analysis of unreinforced masonry." *Journal of Structural Engineering*, ASCE Vol.124(3): pp.270-277.